UNIVERSIDADE ESTADUAL DE CAMPINAS
Faculdade de Engenharia Mecânica

CAMILO AUGUSTO FERNANDES SALVADOR

Phase transformations, microstructure and mechanical properties of new beta metastable Ti-Nb-Zr-Fe (TNZF) alloys for biomedical applications

Transformações de fase, microestrutura e propriedades mecânicas de novas ligas de titânio beta metaestáveis do sistema Ti-Nb-Zr-Fe (TNZF) para aplicação biomédica

CAMPINAS
2019

CAMILO AUGUSTO FERNANDES SALVADOR

Phase transformations, microstructure and mechanical properties of new beta metastable Ti-Nb-Zr-Fe (TNZF) alloys for biomedical applications

Transformações de fase, microestrutura e propriedades mecânicas de novas ligas de titânio beta metaestáveis do sistema Ti-Nb-Zr-Fe (TNZF) para aplicação biomédica

Thesis presented to the School of Mechanical Engineering of the University of Campinas in partial fulfillment of the requirements for the degree of Doctor in Mechanical Engineering, in the area of Materials and Fabrication Processes.

Tese apresentada à Faculdade de Engenharia Mecânica da Universidade Estadual de Campinas como parte dos requisitos exigidos para a obtenção do título de Doutor em Engenharia Mecânica, na Área de Materiais e Processos de Fabricação.

Orientador: Prof. Dr. Rubens Caram Junior

ESTE EXEMPLAR CORRESPONDE À VERSÃO FINAL DA TESE DEFENDIDA PELO ALUNO CAMILO AUGUSTO FERNANDES SALVADOR, E ORIENTADA PELO PROF. DR. RUBENS CARAM JUNIOR.

CAMPINAS
2019

Ficha catalográfica
Universidade Estadual de Campinas
Biblioteca da Área de Engenharia e Arquitetura
Rose Meire da Silva - CRB 8/5974

Sa38p

Salvador, Camilo Augusto Fernandes, 1988-
Phase transformations, microstructure and mechanical properties of new beta metastable Ti-Nb-Zr-Fe (TNZF) alloys for biomedical applications / Camilo Augusto Fernandes Salvador. – Campinas, SP : [s.n.], 2019.

Orientador: Rubens Caram Junior.
Tese (doutorado) – Universidade Estadual de Campinas, Faculdade de Engenharia Mecânica.

1. Ligas de titânio. 2. Biomateriais. 3. Tratamentos térmicos. 4. Transformações de fase. 5. Propriedades mecânicas. I. Caram Junior, Rubens, 1958-. II. Universidade Estadual de Campinas. Faculdade de Engenharia Mecânica. III. Título.

Informações para Biblioteca Digital

Título em outro idioma: Transformações de fase, microestrutura e propriedades mecânicas de novas ligas de titânio beta metaestáveis do sistema Ti-Nb-Zr-Fe (TNZF) para aplicação biomédica
Palavras-chave em inglês:
Ti alloys
Biomaterials
Aging heat-treatments
Phase transformations
Mechanical properties
Área de concentração: Materiais e Processos de Fabricação
Titulação: Doutor em Engenharia Mecânica
Banca examinadora:
Rubens Caram Junior [Orientador]
Claudemiro Bolfarini
André Paulo Tschiptschin
João Batista Fogagnolo
Rodrigo José Contieri
Data de defesa: 02-04-2019
Programa de Pós-Graduação: Engenharia Mecânica

Identificação e informações acadêmicas do(a) aluno(a)
- ORCID do autor: https://orcid.org/0000-0002-9128-2044
- Currículo Lattes do autor: http://lattes.cnpq.br/5066314956831269

UNIVERSIDADE ESTADUAL DE CAMPINAS
FACULDADE DE ENGENHARIA MECÂNICA

TESE DE DOUTORADO ACADEMICO

Phase transformations, microstructure and mechanical properties of new beta metastable Ti-Nb-Zr-Fe (TNZF) alloys for biomedical applications

Transformações de fase, microestrutura e propriedades mecânicas de novas ligas de titânio beta metaestáveis do sistema Ti-Nb-Zr-Fe (TNZF) para aplicação biomédica

Autor: Camilo Augusto Fernandes Salvador
Orientador: Prof. Dr. Rubens Caram Junior

A Banca Examinadora composta pelos membros abaixo aprovou esta Tese:

Prof. Dr. Rubens Caram Junior
DEMM-FEM-UNICAMP

Prof. Dr. Claudemiro Bolfarini
DEMA-UFSCAR

Prof. Dr. André Paulo Tschiptschin
PMT-EPUSP

Prof. Dr. João Batista Fogagnolo
DEMM-FEM-UNICAMP

Prof. Dr. Rodrigo José Contieri
FCA-UNICAMP

A Ata da defesa com as respectivas assinaturas dos membros encontra-se no processo de vida acadêmica do aluno.

Campinas, 02 de Abril de 2019.

“That is the problem with ignorance. You can never truly know the extent of what you are ignorant about.”

— Adrian Tchaikovsky, Children of Time (2015)

This document is dedicated to Leandro, my brother, to my parents, Ester and Sergio, and my dear friends. Thank you for your adamant support and love.

Acknowledgments

First and foremost, I would like to express gratitude to my supervisor, Prof. Rubens Caram, for his support and encouragement throughout the last seven years. I thank Rubens to give me the freedom to try some insane ideas. I am sure it was not easy, but I am happy that (surprisingly) some of them worked.

Many thanks to Prof. Hamish L. Fraser for his guidance, patience, and support during my internship at The Ohio State University. Thank you for giving me the opportunity of being part of your research group. My stay at OSU was essential; in a way, I cannot even describe (or understand) it yet. It certainly changed the way I perceive materials science, research, and life.

I would like to thank the following people for their support, without whose help this work would never have been possible: Alberto Fatichi, Babu Viswanathan, Brian Welk, Carlos Ospina, Daniel Huber, Dalton Lima, Dean Sage, Eder Lopes, Eloá Lopes Maia, Fernando Costa, Guilherme Faria, Hendrik Colijn, Jefferson Bettini, João Oliveira, Kaio Campo, Julian Escobar, Marcia Taipina, Mariana Dal Bó, Mariana Mello, Victor Opini, and Sam Kuhr. Thanks to all of the members of the Caram research group, the Fraser research group, CEMAS personnel, UNICAMP personnel, and the CNPEM staff. Finally, many thanks to the members of the committee for the fruitful discussions Thanks all the readers of this document.

This study was financed in part by the São Paulo Research Foundation (FAPESP), grants 2014/24449-0 and 2016/22714-3.

This study was financed in part by The Brazilian National Council for Scientific and Technological Development (CNPq), grant #405054/2016- 5.

Resumo

A obtenção de ligas de titânio de baixo custo com elevada razão entre tensão de escoamento e módulo de elasticidade (EAS) é um dos grandes desafios na área de biomateriais estruturais. Neste estudo, nós respondemos a esse desafio em duas frentes. Inicialmente, exploramos o sistema Ti-Nb-Fe com o objetivo de encontrar composições otimizadas, que apresentassem um baixo módulo de elasticidade com um teor de Nb reduzido. Lingotes das ligas Ti-(31-4x)Nb-(1+0.5x)Fe foram preparados, enquanto o Nb foi sendo substituído por Fe, a partir da liga Ti-31Nb-1.0Fe até a liga Ti-11Nb-3.5Fe. As amostras foram solubilizadas e testadas sob três diferentes condições: resfriada em água, resfriada em forno e envelhecida (diversas temperaturas). As microestruturas resultantes foram analisadas por meio de difração de raios-X, calorimetria exploratória diferencial, microscopia eletrônica de varredura e de transmissão. Entre as ligas ternárias, a liga Ti-19Nb-2.5Fe foi a que apresentou a melhor combinação de resistência mecânica e módulo de elasticidade. As amostras envelhecidas revelaram dados interessantes sobre a formação e crescimento da fase alfa neste sistema durante o envelhecimento. Em geral, a formação de alfa se dá preferencialmente nos contornos de grão, mesmo em tratamentos isotérmicos de curta duração (1 min). Uma microestrutura composta de grãos de beta e fase alfa fina e dispersa foi obtida para a maioria das ligas através de envelhecimentos à 450 ºC.

A segunda parte do projeto consistiu na exploração de ligas quaternárias Ti-Nb-Fe-Zr, com adições de 4 a 13% (peso) de Zr. Uma liga adicional, baseada na liga Ti-19Nb-2.5Fe, foi preparada com adição de 6% de Sn. Além de todo o trabalho de caracterização executado, ensaios de tração a temperatura ambiente comprovaram que ligas do sistema Ti-Nb-Fe-Zr podem atingir EAS próxima de 1,5, com boa ductilidade. As adições de Zr e Sn foram uteis na supressão da fase omega após resfriamento em água. Além disso, Zr e Sn são igualmente particionados entre matriz e precipitados durante o envelhecimento. Enquanto a difusão de Nb e Fe foi favorecida pelos contornos de grão, ela parece ser inibida na presença de Zr e Sn. Como consequência, adições de Sn resultam em uma maior resistência mecânica e precipitação de alfa mais refinada. Finalmente, um mapa de seleção de materiais é apresentado com o objetivo de ajudar futuros autores a comparar ligas de aplicação biomédica tendo como parâmetros a razão tensão-módulo (EAS) e o custo.

Palavras-chave: Ligas de titânio; biomateriais; tratamentos térmicos; transformações de fases; propriedades mecânicas.

Abstract

An open challenge on structural biomaterials is to obtain low-cost Ti-alloys with a high elastic admissible strain (the ratio of yield strength to elastic modulus). In this study, we addressed the presented challenge via two working directions. Firstly, we explored the Ti-Nb-Fe system to find an optimal, cost-effective composition with a compromise between a low elastic modulus and low added Nb contents. Ti-(31-4x)Nb-(1+0.5x)Fe ingots were prepared, and Nb was substituted with Fe, starting at Ti-31Nb-1.0Fe and going down to Ti-11Nb-3.5Fe (wt%). The samples were solution-treated and tested under three conditions: water-quenched, furnace-cooled and step-quenched to different temperatures. Resultant microstructures were analyzed with the aid of X-ray diffraction, differential scanning calorimetry, scanning, and transmission electron microscopy. Among the ternary alloys, Ti-19Nb-2.5Fe (wt. %) presented the best combination of mechanical strength and elastic modulus. The heat-treated samples provided useful insights into how the alpha-phase formation starts and develops in this system during aging. In general, alpha-phase precipitation starts at the grain boundaries, even after very short-time isothermal heat-treatments (1 min). Overall, an optimized microstructure composed of beta-grains and fine and dispersed alpha-phase was obtained for most of the experimental alloys after aging at 450 ºC.

The second part of this project comprises the exploration of Ti-Nb-Fe-Zr quaternary alloys, with additions of 4-13 wt.% of Zr. One additional alloy, based on Ti-19Nb-2.5Fe, was prepared with additions of 6 wt.% of Sn. Beyond all the characterization work, tensile tests performed at room-temperature confirmed that Ti-Nb-Fe-Zr alloys could reach an elastic admissible strain close to 1.5, with relatively good ductility. Regarding the Zr and Sn additions, they helped suppress omega formation after water-quenching. Also, Zr and Sn were equally distributed between matrix and precipitates during aging. While the diffusion of Nb and Fe were enhanced via grain-boundaries, they seemed to be inhibited by the presence of Zr and Sn. As a result, these elements allow higher yield-strengths and more refined secondary α-phase. In the end, a materials selection chart is presented to help future researchers to compare materials for orthopedic implants considering the elastic admissible strain and cost as significant guidelines.

Keywords: Ti alloys; Biomaterials; Aging heat-treatments; Phase transformations; Mechanical properties.

List of Figures

List of Tables

List of Abbreviations

APT – Atom probe tomography

ath – athermal

BOR – Burgers orientation relationship

BSE – Backscattered electrons (detector)

Cs – spherical aberration (correction)

DB-FIB - dual-beam, focused ion-beam

EAS – elastic admissible strain

EELS – electron energy loss spectroscopy

EDS – energy dispersive spectroscopy

EPMA – electron-probe microanalysis

FC – furnace cooled

FFT – Fast-Fourier Transformation

GB – grain boundary(ies)

HAADF – high-angle annular dark-field

HR – high-resolution

HT – heat treatment

IG – Intragranular

IPS – invariant plane strain

iso – isothermal

Ms – martensite start temperature

Mf – martensite finish temperature

OSU – Ohio State University

PTMC - phenomenological theory of martensite formation

ROI – region of interest

SAD – selected-area diffraction

SEM – scanning electron microscopy

SIM – stress-induced martensite

SQ – step-quenched

ST – solution-treated

STEM – scanning transmission electron microscopy

STFS – stress-free transformation strain

TEM – transmission electron microscopy

TNZT – Ti-Nb-Zr-Ta (refer to the alloy or the system)

TNFZ – Ti-Nb-Fe-Zr (refer to the alloy or the system)

TNZF – analogous to TNFZ

TNFS - Ti-Nb-Fe-Sn (refer to the alloy or the system)

WQ – water quenched

XEDS – X-ray energy dispersive spectroscopy

XRD – X-ray diffraction

XRF – X-ray fluorescence

σ – standard deviation for a normal distribution

Table of Contents

1. OBJECTIVES AND INTRODUCTION

In Brazil, the manufacturing of orthopedic implants and, hence, the development of low-cost Ti alloys present themselves as a latent necessity. In 2016, the Brazilian medical devices market reached an estimated US$ 5.4 billion per year, with a commercial deficit of US$ 3.4 billion [1]. More than that, expenses with orthopedic and prosthetic implants increased by 78% in 8 years [2].

In orthopedic implants, a low elastic modulus is essential to prevent the bone stress-shielding effect, reducing the probability of failure or a revision surgery [3]. Also, a high yield strength is desirable to withstand the stress cycles to which the component is subjected, and sometimes to minimize component size. In this context, the development of a special class of Ti-alloys known as “gum metals” by Saito et al. (2003) [4] was groundbreaking. With a distinguished cold-workability, high-strength, low elastic modulus, and good biocompatibility, gum metal and related alloys satisfied all at once the requirements for hip and knee replacements, despite their high-cost. Thereon, the combination of Ti-35Nb-5Ta-7Zr-0.4O wt.% (TNZT-O) high-strength (976 MPa) and low modulus (66 GPa) has been considered a benchmark in the orthopedic field for the last 20 years [5]. On the other hand, despite the maturity of Ti-Nb-Zr-Ta gum metals, a remarkable number of studies investigating new formulations of gum-type alloys have appeared during the last decade. Researchers have been trying to reduce the cost of the alloys by substituting Nb and Ta, which are relatively expensive, with low-cost elements such as Fe, Sn and Mn [6].

The primary goal of the study to be presented in this thesis was to design novel Ti-Nb-Fe and Ti-Nb-Fe-Zr alloys, to characterize their microstructure and mechanical properties and, ultimately, to determine the viability of the alloys as structural biomaterials. After an initial exploration of the ternary Ti-Nb-Fe system, new ideas emerged involving the secondary-phase precipitation in Ti-11Nb-3.5Fe (wt. %), which could be associated with a pseudospinodal decomposition. This exploration led to microstructural evolution studies with carefully designed step-quench heat-treatments, among 17 compositions. Thus, a secondary objective of this work was to evaluate the influence of the chosen alloying elements on the microstructural changes observed during aging.

This dissertation has seven chapters. In Chapter 2 of this document, a brief literature review on Ti-alloys is presented. Since the literature on Ti-alloys is vast and diverse, the text is focused on gum metals and precursors of the Ti-Nb-Fe-Zr system. Chapter 3 describes the

experimental procedures including sample preparation using the focused-ion-beam (FIB) and a useful common-background of the characterization of Ti-alloys via transmission-electron microscopy (TEM).

Chapter 4 details the exploration of the Ti-Nb-Fe ternary system, based on six Ti-(31-4x)Nb-(1+0.5x)Fe alloys in which Nb was substituted with Fe, starting at Ti-31Nb-1.0Fe and going up to Ti-11Nb-3.5Fe (wt%). Phase transformations and mechanical properties were included in this chapter. Chapter 5 details the formation of omega-phase in three Ti-Nb-Fe alloys subjected to low-temperature heat-treatments. Chapter 6 examines the alpha-phase precipitation mechanisms among Ti-alloys. This chapter combines thermodynamic simulations and advanced characterization techniques such as nanometer-scaled microanalysis (STEM-EDS). Models concerning the enthalpy and kinetics of the α-phase precipitation were included in Chapter 6. Chapter 7 was dedicated to the addition of Zr (4-13 wt.% contents) to previous characterized Ti-Nb-Fe alloys. Chapter 8 displays the final Ti-Nb-Fe-Zr compositions obtained through this study, their mechanical behavior, and a materials-selection map that allows the reader to have a dimension on how these alloys perform compared to other biomedical alloys concerning yield-strength, elastic modulus, and cost.

1.1 List of Appended Papers

Chapter 4 – Exploring the ternary system

- **Camilo A. F. Salvador**, Mariana R. Dal Bó, Fernando H. Costa, Marcia O. Taipina, Eder S.N. Lopes, Rubens Caram, Solute lean Ti-Nb-Fe alloys: An exploratory study, Journal of the mechanical behavior of biomedical materials 65 (2017) 761–769

Chapter 5 – Isothermal omega-phase in ternary alloys

- **Camilo A. F. Salvador**, Mariana R. Dal Bo, Yufeng Zheng, Eder S. N. Lopes, Rubens Caram, Hamish Fraser, Investigation of the morphology of isothermal omega-phase in Ti-Nb-Fe Alloys, to be submitted (2019).

Chapter 6 – Mechanisms of alpha-phase precipitation

- **Camilo A. F. Salvador**, Victor C. Opini, Mariana G. Mello, Rubens Caram, Effects of double-aging heat-treatments on the microstructure and mechanical behavior of an Nb-modified Ti-5553 alloy, Materials Science & Engineering A 743 (2019) 716–725.

- **Camilo A. F. Salvador**, Eder S. N. Lopes, Jefferson Bettini, Rubens Caram, Formation of alpha phase via pseudospinodal decomposition in Ti-Nb-Fe based alloys, Materials Letters 189 (2017) 201–205.
- **Camilo A. F. Salvador**, Mariana R. Dal Bó, Mariana G. Mello, Alisson K. da Silva, Rubens Caram, and Hamish L. Fraser, Bainitic alpha-phase formation in Ti-alloys – microstructural, thermodynamic and kinetic aspects, to be submitted (2019).

Chapter 7 – Microstructure and mechanical behavior of quaternary alloys

- Mariana R. Dal Bó, **Camilo A. F. Salvador**, Mariana G. Mello, Dalton D. Lima, Guilherme A. Faria, Antonio J. Ramirez, Rubens Caram, The effect of Zr and Sn additions on the microstructure of Ti-Nb-Fe gum metals with high elastic admissible strain, Materials and Design 160 (2018) 1186–1195.
- **Camilo A. F. Salvador**, Mariana R. Dal Bó, Dalton D. Lima, Rubens Caram, Substituting Nb with Fe in Ti-Nb-Zr-Fe alloys: microstructure and mechanical behavior, to be submitted (2019).

2. LITERATURE REVIEW

2.1. Titanium: history and a brief introduction

Ti is the fourth most abundant engineering metal in the earth's crust (0.6%), after Al, Fe, and Mg. Titanium oxides ilmenite and rutile were first discovered by British mineralogist William Gregor and German chemist Martin Klaproth, respectively, during independent efforts in the years of 1791 and 1795. Nevertheless, the production of metallic, high-purity Ti proved to be challenging, given its reactivity with oxygen and nitrogen. In this way, the titanium industry development was delayed more than a hundred years. It started only in the year of 1932, with the advent of the so-called "Kroll process" by chemist Milhelm Kroll. The Kroll process is a convenient method of isolating metallic Ti from oxides on an industrial scale. It consists of reducing $TiCl_4$ using metallic-magnesium under an inert atmosphere. The Kroll method, however, is a batch process that demands high quantities of energy, which contributes to the elevated cost of pure Ti and, therefore, of Ti alloys even nowadays [7].

Throughout history, Ti alloys have become distinguished materials for a wide range of applications in the chemical, aerospace and biomedical industries owing to a combination of high-strength, low-density, and exceptional corrosion resistance.

Ti presents allotropy in the solid-state. The crystallographic allotropes are named α-phase, which has a hexagonal close-packed (hcp) structure, and β-phase, the high-temperature body-centered cubic (bcc) phase – see Figure 2.1. The allotropic transformation temperature in Ti established as β-*transus* is placed at 882 ºC. In equilibrium conditions, cooling from temperatures above β-*transus* leads the β phase to transform into α phase. Alloying elements considered α-stabilizers (Al, O, N, etc.) tend to increment the β-*transus* temperature, stabilizing α phase at higher temperatures. On the other hand, the addition of β-stabilizers might reduce it, allowing β-phase to be stable[1] at temperatures lower than 882 ºC. Among β-stabilizers, there are isomorphous stabilizers (Nb, Ta, Mo, V, etc.), which form extensive β phase solid solutions, and eutectoid stabilizers (Cu, Co, Cr, Ni, etc.), which have limited solubility in the β phase; during cooling, eutectoid stabilizers can associate with Ti to form intermetallic compounds via a eutectoid reaction (β → α + TiX intermetallic).

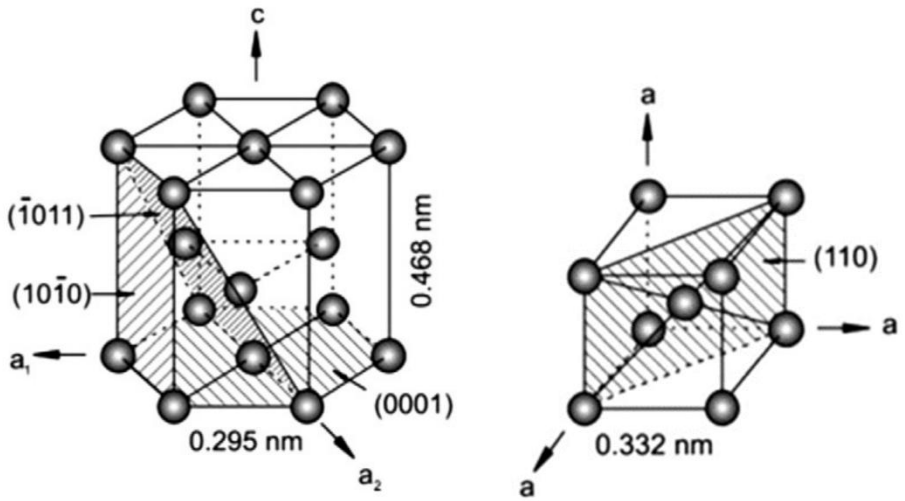

Figure 2.1 – A representation of β and α unit cells, adapted from Banerjee et al. (2003) [8]

[1] Or at least metastable, i.e. at a meta-equilibrium state

2.2. Titanium classes

As a convention, titanium alloys can be divided into three different broad classes, designated as α, α+β, and β alloys. A schematic phase diagram containing such classes is presented in Figure 2.2. Physical and mechanical properties of each class are highly affected by their microstructural features.

Pure Ti, α, and near-α were the first classes of Ti alloys to be designed. Their microstructures contain primarily α-phase. In addition to Ti, α-alloys have a small quantity of alloying elements such as Al, Sn, and impurities such as O and Fe. Thermally-activated diffusion is smaller in the α-phase comparatively to the β-phase; therefore these alloys are employed to high-temperature applications, usually up to 600 °C. Regarding clinical applications, pure Ti was the pioneer to be used for the fixation of bone fractures in the ’50s [9]. The criteria to its application in the biomedical field are currently described in ASTM F67. According to this ASTM standard, primary-α grain size must lie on the range of 10-150 μm to ensure proper mechanical strength and ductility. However, over history, the use of pure Ti has been restricted due to its low mechanical strength [18]. Oxygen content usually varies from 0.18 to 0.40 wt. %, depending on the desired alloy-grade since O can improve yield strength to near 485MPa via interstitial solid solution [10].

To further explore the mechanical properties of Ti alloys, Ti-6Al-4V was introduced to the biomedical field in the ’70s, with the combined addition of α (Al) and β (V) stabilizers. Ti-6Al-4V - often referred to Ti-6-4 for short - is the workhorse of Ti alloys, employed to varied applications. The duplex microstructure with both α and β phases exhibited at the room temperature (RT) allows Ti-6Al-4V to achieve yield strengths of approximately 1000 MPa. In the biomedical field, Ti-6Al-4V is referred to ASTM F136 [11], in the wrought condition, or ASTM F1108, in the as-cast condition. A few attempts to produce other α+β alloys similar to Ti-6Al-4V by making solute replacements were succeeded, as in the case of Ti-6Al-7Nb, or ASTM F1295 [12], which have similar properties of the parent alloy.

The latest classes to be developed were the β and β-metastable classes. Nowadays, β and β-metastable Ti-alloys are the preferred candidates in the field of orthopedic biomaterials, thanks to their relatively low elastic modulus, biocompatibility, and an improved forgeability and cold-workability compared to α-β alloys, due to a greater number of slip systems available in the bcc-β in comparison to the hcp-α crystal structure [13].

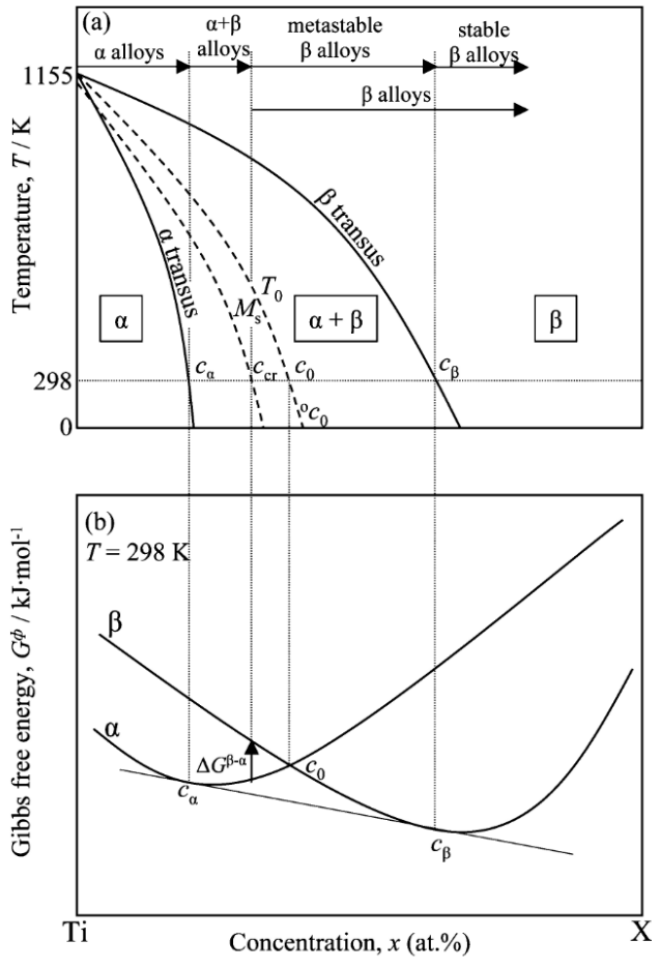

Figure 2.2 – Schematics of a phase-diagram showing the respective Gibbs free energy curves for both α and β phases, as a function of the solute concentration. The Ms line represents the martensite start temperature. ccr is the critical concentration required to retain β-phase upon quenching from the β-phase region completely. T0 line represents the metastable equilibrium temperature between the α- and β-phases, at which Gα = Gβ. c0 and oc0 are metastable equilibrium concentrations between the α- and β-phases at room temperature (298 K) and 0K, respectively. Adapted from Uesugi et al. (2013) [14].

The number of studies concerning β-metastable Ti alloys has been growing consistently since the ’90s. According to Kolli & Devaraj (2018), the total of publications indexed from Web of Science now reached approx. 650 (Figure 2.3) and might grow in the following decades with further alloy development, advanced characterization techniques, and computational tools [15]. In addition to that, a search through Web of Science indicates 20 papers published in the last ten years pointedly relating to “gum metals.”

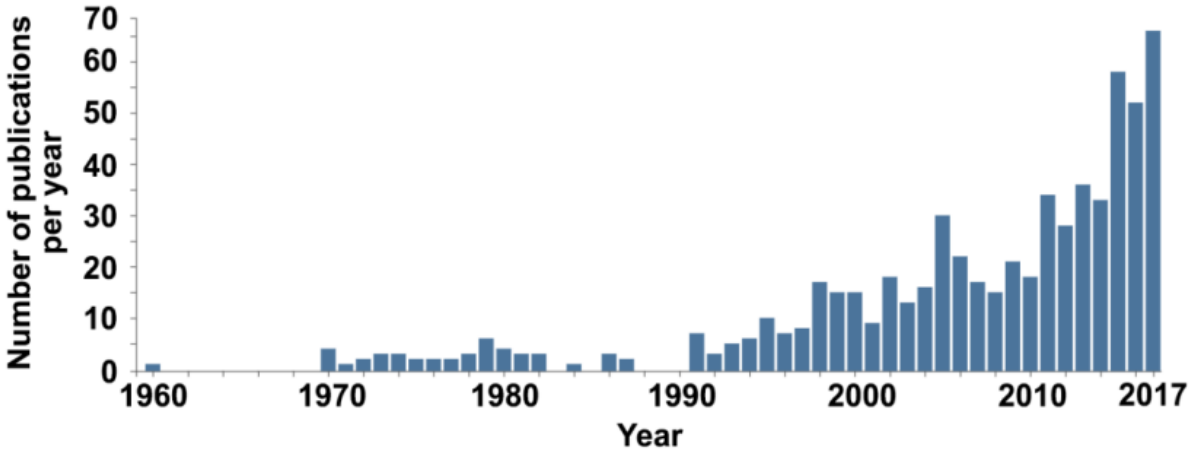

Figure 2.3 – Number of publications per year concerning "beta metastable titanium alloys" indexed from Web of Science. Adapted from Kolli et al. [15].

2.3. Metastable phases

Hexagonal (α') and orthorhombic (α") martensite phases can be formed by rapid quenching β-metastable Ti alloys from the β phase field, depending on the β-stabilizer solute content of the alloy. A small percentage of β-alloying elements leads to the formation of α' martensite, which has the same structure of α (hex), but it is frequently supersaturated concerning solute elements. For alloys with higher solute content, orthorhombic martensite (α") is formed instead. With the increase of the β stabilizing solute content, a decrease of the Ms temperature (martensite start) is observed, to the point that α' and α" are not formed anymore. To illustrate this behavior, let's look at the Ti-Nb binary system. Among Ti-Nb alloys, α' is reported to be formed upon quenching in alloys with an Nb content smaller than 17.5 wt. % [16], followed by the formation of α" in alloys with an Nb content up to approx.. 36.2 wt. % [17]. Alloys with Nb contents higher than 36 wt.% Nb present a microstructure dominated by β and athermal-ω phases (Figure 2.4).

There are other aspects of the α"-phase formation that will not be treated here. In broad terms, α" can also be formed as a precursor to α-phase during heating [18,19], or under stress-strain cycles, as a product of a stress-induced martensitic (SIM) formation, which is associated with super-elasticity and to shape-memory-effect. These aspects are further discussed in papers concerning shape-memory alloys, such as [20–24].

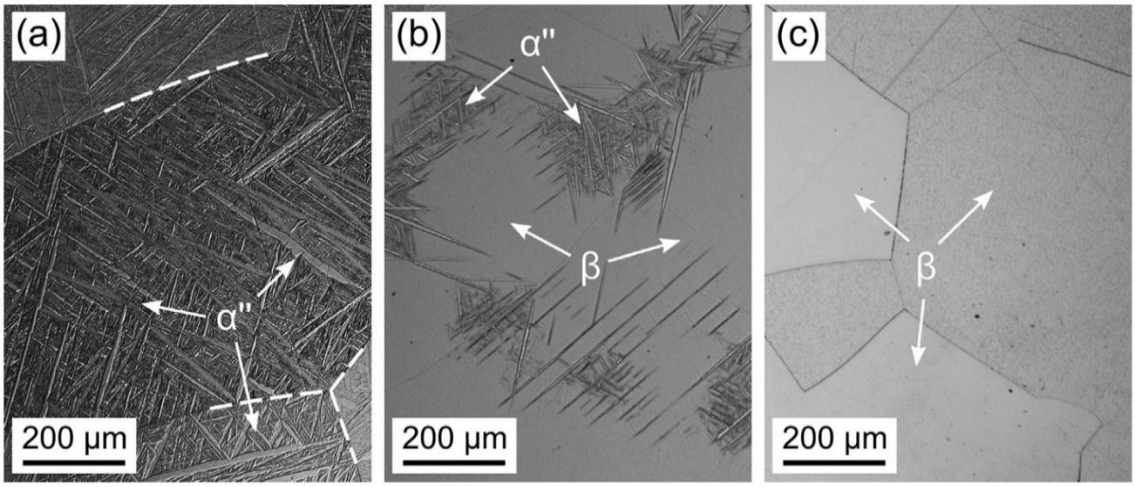

Figure 2.4 – Optical micrographs of Ti-Nb alloys after WQ. (a) Ti-33Nb, (b) Ti-38Nb and (c) Ti-44.5Nb wt. %. Taken from Bönisch et al. (2017) [25].

Athermal ω phase (hexagonal) can be formed from β phase on quenching due to a first order transition. Ath-ω has a size limited to a few nanometers, and its formation occurs by the collapse of alternate pairs of (222)β planes (see Figure 2.5), through a diffusionless mechanism [26–29]. During heating, or at low-temperature aging heat-treatments, the volumetric fraction of ω-phase increases quickly as the ω precipitates grow by rejecting all major solutes to the surrounding β-matrix [30,31], giving rise to isothermal ω-phase (iso-ω) precipitates. These are larger precipitates which can develop to the size of 100 nm [32]. During aging heat treatments, the composition of iso-ω particles might be altered over time, before the point that both phases reach a structural/compositional metastable equilibrium [33–36]. Later on, depending on the temperature, the ω-particles might act as nucleation sites for the α-phase (α), what comprises an important strategy for obtaining high-strength Ti-alloys known as "ω-assisted α-phase formation," with microstructures composed of fine and dispersed α-phase through the β matrix [37–43]. However, the formation of ω phase has deleterious effects on mechanical properties, turning the material fragile, often elevating the elastic modulus and depreciating fatigue resistance [44]. Characteristics of the ω-phase formation in the Ti-Nb-Fe system will be treated in Chapter 5.

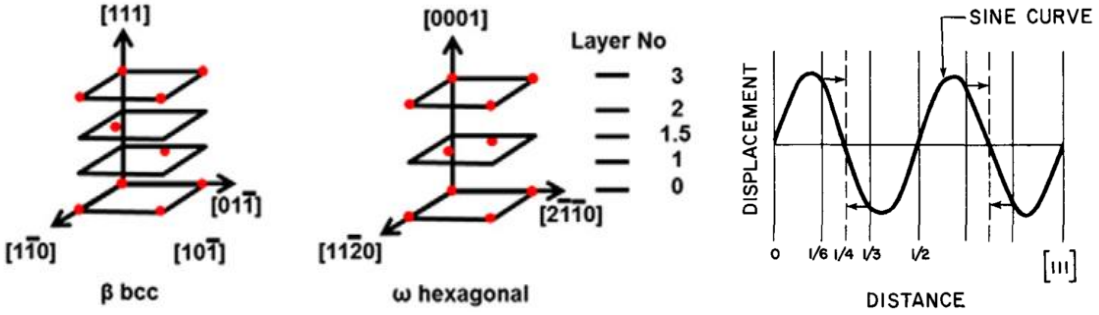

Figure 2.5 – Schematic representations of the β-ω transformation. Left - the collapse of atomic layers to form ω-phase. Left - the displacement of the atoms, with (111) planes displayed horizontally. Adapted from Banerjee et al. (2003) [45] and De Fontaine et al. (1970) [26], respectively.

In the last years, there has been an increasing interest in the role of metastable phases in the microstructural evolution of Ti-alloys. Recent studies by Zheng et al. suggests that there are other two additional orthorhombic phases (other than α") formed before α formation. The first one would be the O' phase, first detected among Ti-18Mo (wt.%) quenched samples. O'-phase was found in conjunction with ω-phase, in the presence of an excess of solute elements which reduce ω-stability. The β-lattice gives origin to O' as atoms on every other {110}β planes shuffle in the <110>β direction [46]. According to Liang et al., elements such Zr, Sn, Al, and O partially suppress the 2/3<111>β longitudinal phonon, which is necessary to form ω-phase, favoring the transverse {011}<011>β phonon instead, thus favoring the formation of O'. [47].

According to Zheng et al., the phase named O" can be formed while heating Ti-5553 to 375 ºC at a rate of 5 ºC/min. O" has face-centered orthorhombic structure, belonging to space group F_{mmm}, with lattice parameters a = 0.328 nm, b = 0.464 nm and c = 1.393 nm. The orientation relationship between O" and the β-matrix is given by: $(001)_{O"}$ // $(011)_{\beta}$ and $[100]_{O"}$ // $[100]_{\beta}$. The same way as α"-phase, the relatively small misfit between O" and β allows them to share a coherent interface. O" has a spherical morphology, its size is restricted to near 10 nm. The discovery of the O′ and O" phases will become more and more relevant in the future since its presence might be associated with the origins of ultralow modulus in Ti-alloys. So far, O' and O" phases can only be undoubtedly characterized via high-resolution techniques. Curiously, the preferred crystal orientation for such analyses is the (100)β.

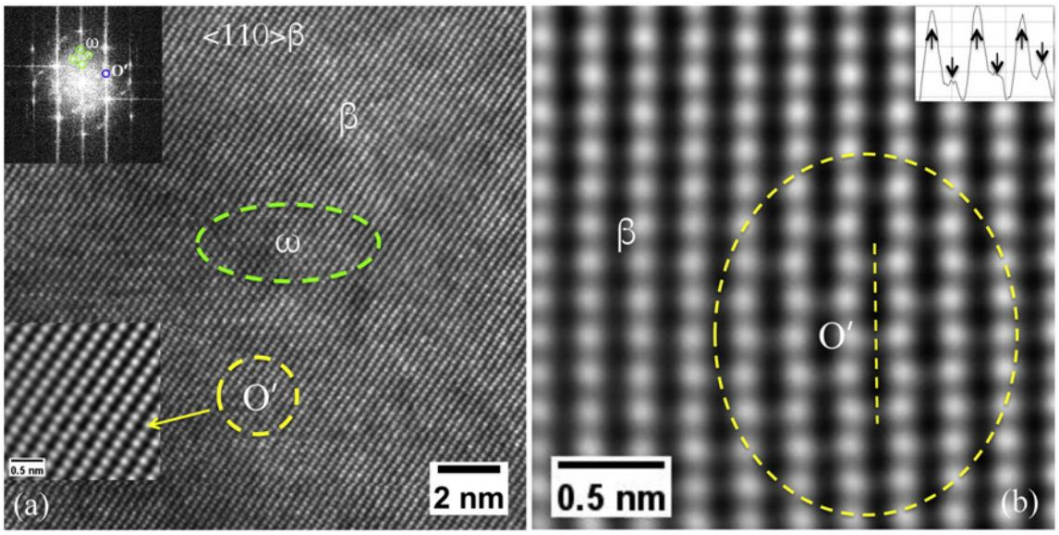

Figure 2.6 – HAADF-STEM images showing the co-existence of athermal ω phase and O′ phase in Ti–18Mo (a) and (b) higher magnification image showing {110}<110> shuffle in the center of O′ phase; adapted from Zheng et al. (2016) [46].

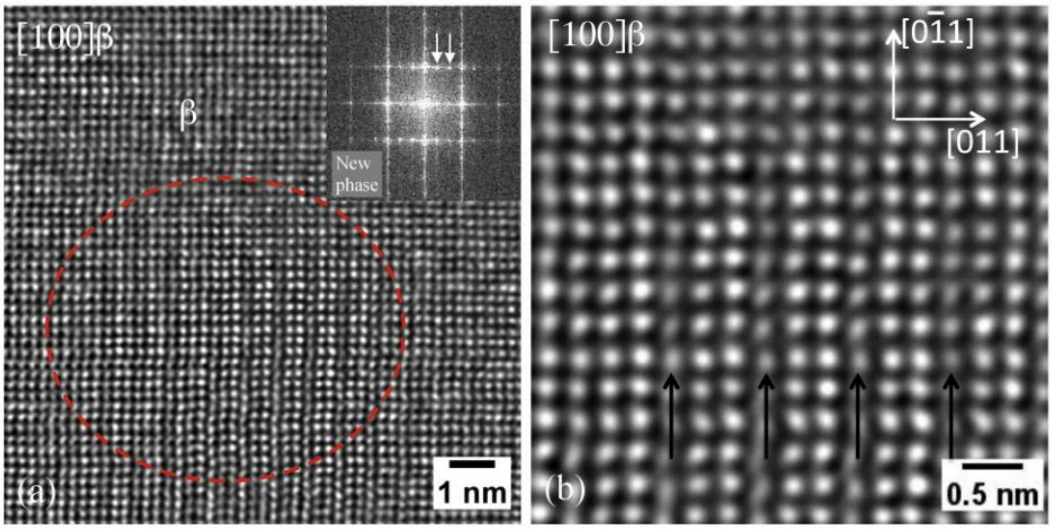

Figure 2.7 – HAADF–STEM images showing the ordered structure of O” phase and its Fast Fourier Transformation (inset) (a) and a high magnification image showing the periodic intensity change (ordering) along [011]β direction (b); adapted from Zheng et al. (2016) [48].

It is now clear that the microstructures in Ti can be rather complex. However, depending on the solute content, it is possible to have a previous idea of which metastable should be formed, and why. To assist with these predictions, a pseudo-binary phase diagram

of Ti-alloys including the metastable phases briefly presented in this section is shown in Figure 2.8. The diagram also includes the solute range in which a β/β' phase separation is expected as a result of a spinodal decomposition [49].

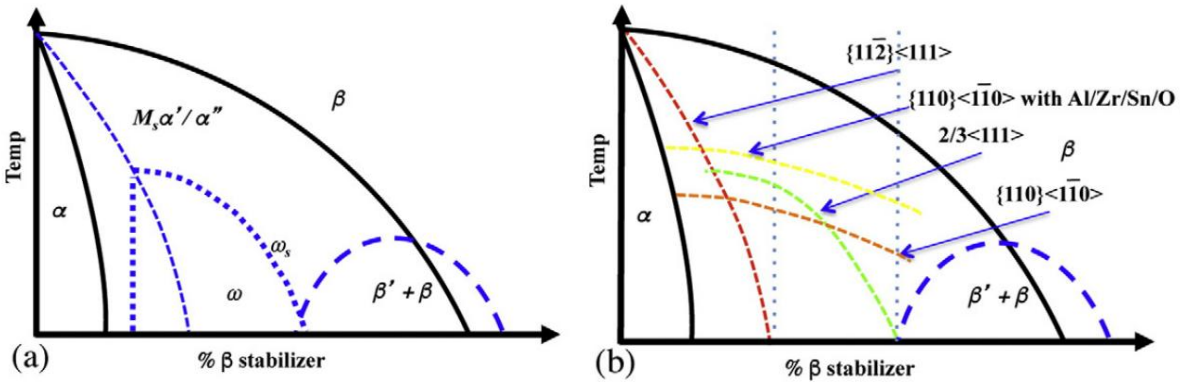

Figure 2.8 – Schematic figure showing various phases in the Ti-X pseudo-binary phase diagram (a) and the phonon instabilities associated with the formation of O′ phase (b). Adapted from Zheng et al. (2016) [46].

2.4. Alpha-phase

In Ti alloys, the β/α interfaces block the dislocation motion; hence, the mechanical strength of any β+α microstructure derive mainly from the size, morphology, and distribution of the α phase. In β-metastable Ti-alloys, the formation of α usually starts at the β-phase grain boundaries, giving rise to colonies of Widmanstätten α-phase laths.

There is a vast amount of literature on the characteristics of the β-α phase transformation in Ti alloys. In general, α-phase is formed following a traditional Burgers Orientation Relationship (BOR), shown in Figure 2.9, with a 6-fold symmetry, which implies {110}β // (0001)α and <1-11>β // (11-20)α. For this reason, 12 crystallographic variants of α can be found in a single β-grain. By looking at the β-α interface with the aid of high-resolution TEM, one might see a semi coherent interface composed of broad faces and structural ledges. The habit plane of the α-plates is {112}β || {10-10}α, and it usually deviates from the normal plane to the broad faces by a small angle. According to the literature, this angle is approximately 14.4-14.9º. Regarding the broad faces, recent works have shown that

these interfaces could also be quite complex, with the presence of slip bands, interfacial dislocations and misfit compensating regions [50,51].

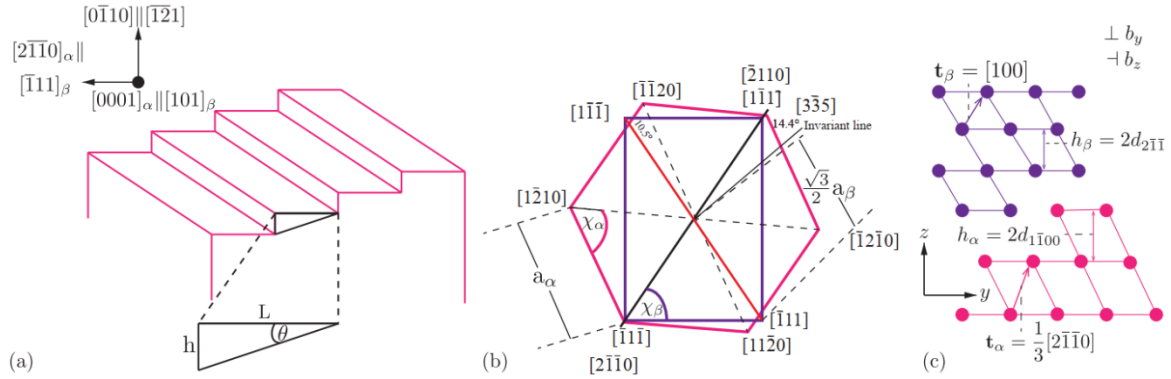

Figure 2.9 – (a) A schematic example of the β-α interface (θ is approx. 14.4º), (b) the burgers orientation relationship showing both phases, being β in purple and α in pink and (c) the trigonometric relations of the interface lattices. Taken from Ackerman et al. (2018) [50].

Since the β-to-α transformation is commonly accompanied by linear lattice strains up to 10%, a massive accumulation of dislocations at the interface would be needed to maintain a coherent interface [52]. For this reason, coherent α is hardly ever seen in Ti-alloys [8]. Another interesting fact is that when two α-variants contact each other, there is no β-phase left between them. According to Zheng et al. (2018), there is a small rotation of one lath in respect to the other, which is linked to the 11º deviation between their individual [-1-120]α directions. Despite this rotation, the variants still share the same <0001>direction and therefore have parallel (0001)α planes – see Figure 2.10 [51].

Based on the nature of the α-β interface, it has been established that the α-plate thickening occurs through the terrace-ledge-kink model, which consider that ledges are incoherent and thus have more mobility to grow. Therefore, ledge-wise growth models can be valuable to analyze the α-phase formation in Ti alloys [50,53]. The mechanisms of α-phase formation will be extensively discussed in Chapter 6.

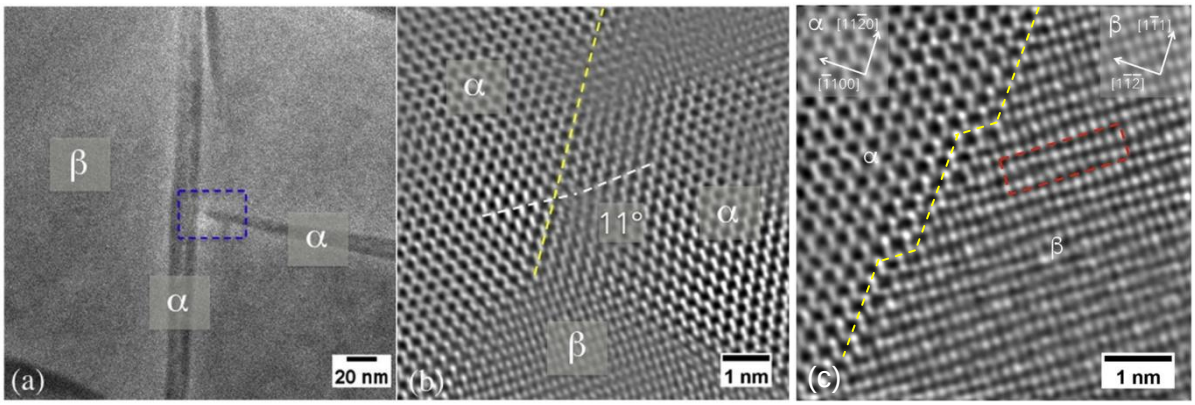

Figure 2.10 – (a) HAADF-STEM image of the intersection of two laths, (b) a detailed, high-resolution image of the intersection and (c) a detail of the semicoherent β-α interface showing the broad faces and the structural ledges. Sample: Ti-5553 fast heated to 600 ºC and isothermally aged for 0 min. Images through the [110]β zone axis. Images adapted from Zheng et al. (2018) [51].

2.5. Electronic parameters

Ti is a transition metal belonging to group 4 of the periodic table of elements. Its electronic ground state configuration is $[Ar]3d^2 4s^2$. This electronic configuration - with 2s and 2d valence electrons - is an important factor influencing the physical properties, metallurgical and alloying behavior of Ti. Elements which have a similar electronic configuration, such as Zr and Hf, present analogous behavior to Ti in respect to their physical metallurgy.

The valence electrons per atom ratio (*e/a*) in Ti-alloys can exert a great influence on the elastic modulus. Experiments with the Ti-Nb and Ti-V binary alloys have shown that a minimum modulus can be obtained in these systems with an e/a ratio between 4.24 and 4.26 [54]. According to Saito et al., in this range, the difference between the elastic constant components C11 and C22 tends to zero, what implies the single-crystal Young's modulus in the <001> direction and the shear modulus along <111>{011}, {112} and {123} slip systems must be zero. In this way, the elastic modulus is minimized [55].

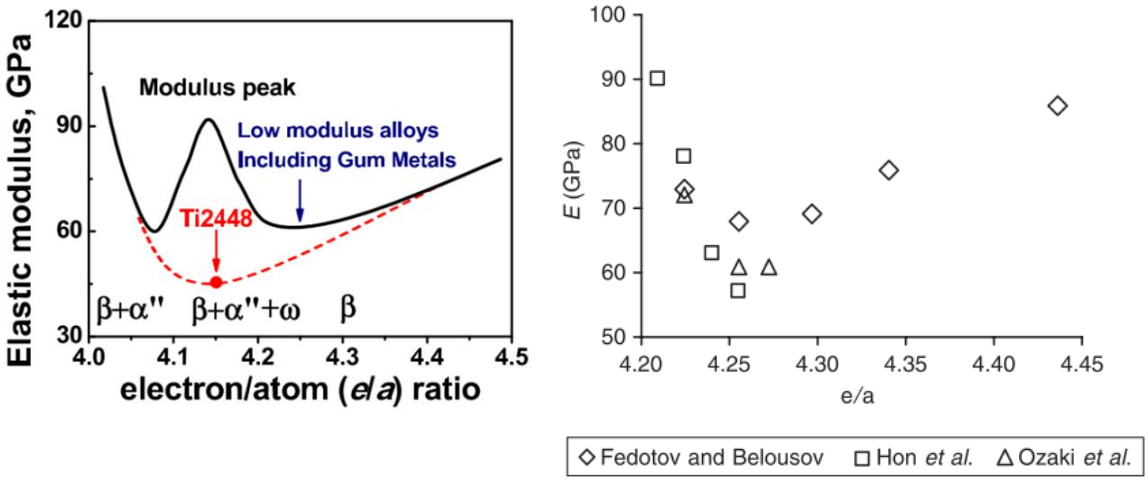

Figure 2.11 – Left – A typical curve is representing the elastic modulus as a function of the e/a ratio in Ti-alloys; the modulus peak can be attributed to the presence of ω-phase. Adapted from Wang et al. [56]. Right – A detailed view of the same diagram showing quenched Ti-Nb binary alloys only. All the alloys were in the composition range where quenching does not lead to the formation of ω or other second phases. Adapted from Todd & Armstrong (2006) [54].

Also, since the ’90s, novel β-type Ti alloys have been designed with the aid of the so-called $\overline{Bo}$ – $\overline{Md}$ diagram proposed by Morinaga et al. [57] and further matured by Abdel-Hady et al. [58]. This diagram correlates two electronic parameters – the bond-order (Bo) and d-electrons energy level (Md) - with the elastic modulus and helps to predict the phases that will be obtained in many alloys after water-quenching them from the β phase field. The bond-order is a parameter which represents the covalent bond strength between Ti and other alloying metals, while Md represents the “d” orbital energy level of any metallic element relative to Ti. For a given alloy, values of $\overline{Bo}$ and $\overline{Md}$ are defined by the compositional average (at.%) of each parameter (Figure 2.12).

Furthermore, according to the diagram, to obtain a low elastic modulus, the co-addition of high-cost elements with high bond order values (i.e., Mo, Nb, Ta, Zr, Hf) seems indispensable. In general, the higher the content of these elements the lower the elastic modulus [58,59]. However, according to the creators of the diagram, the position of the phase-boundaries in the diagram is not precise, given that some elements such as Zr, Sn, O, and Al can shift the β / β+ω boundary line to higher $\overline{Bo}$ values, suppressing the formation of athermal omega (ω_{ath}) even in compositions located on the right side of the line – i.e., in the β+ω field [58,60].

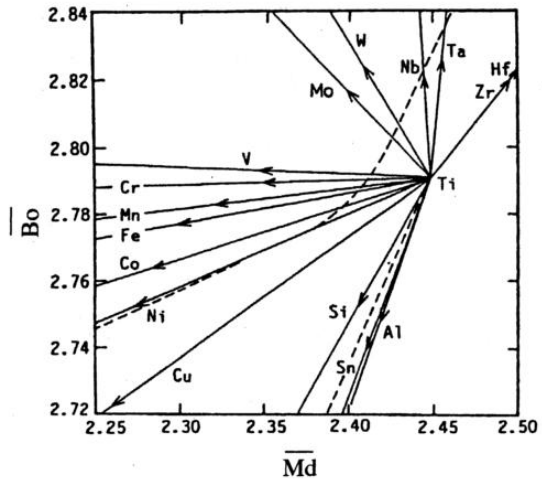

Figure 2.12 – The modification of the $\overline{Bo} - \overline{Md}$ parameters with the addition of certain alloying elements, adapted from Kuroda et al. (1998) [61].

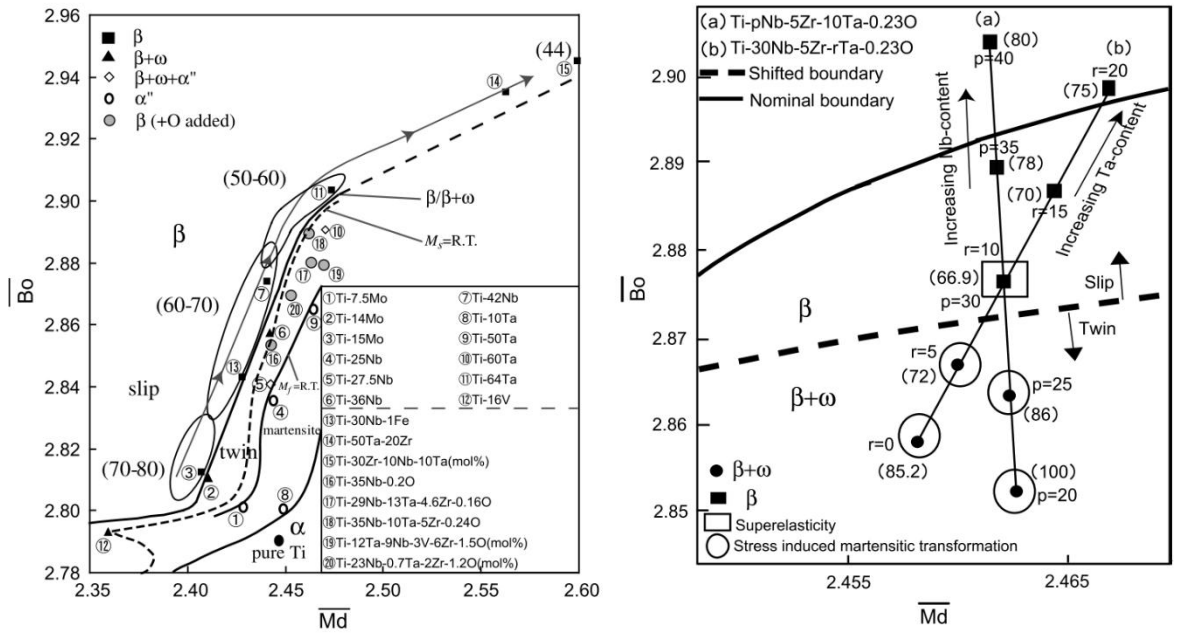

Figure 2.13 – Left - Overview of the Bo x Md diagram containing 20 alloys and their respective positions in the diagram. The β/β+ω domain is shown in dashed lines. Typical elastic modulus is given in parentheses. Right – Phase stability changes with the Nb and Ta content in TNZT alloys. O and Zr additions shift the boundary (dashed-line) up. Adapted from Abdel-Hady et al. (2006) [58].

2.6. Precursors of the Ti-Nb-Fe-X systems

While some research has been carried out on Ti-Fe based alloys, there is very little scientific understanding of the role of Fe on the phase transformations in multicomponent Ti-alloys. Since the early ’60s, studies with alloys containing more than 2.5 wt.% Fe were discouraged. During the ingot fabrication, the addition of Fe in high quantities led to its segregation to regions called β-flecks, which were detrimental to mechanical performance [62]. Furthermore, the metallurgy community raised some concerns about the formation of the Ti-Fe intermetallic compound over a large range of compositions, based on the equilibrium thermodynamics data available for the Ti-Fe binary system (see Figure 2.14). However, later works by Franti et al. and Lee et al. showed that in hypoeutectoid alloys such as Ti-5Fe (wt. %), the formation of Ti-Fe intermetallics occurred very slowly. According to the authors, the delay between the onset of proeutectoid α formation and the beginning of the bainite reaction – which in turn would produce Ti-Fe – is of the order of weeks, even slightly below the eutectoid temperature. Ti-Fe intermetallics could only be seen in Ti-5Fe after 28 days spent at 550 ºC. When detected, the formation of Ti-Fe seemed to occur at impinged proeutectoid α-plates [63,64].

In the ’90s, studies on ternary alloys containing Fe showed that Ti-Fe intermetallics were not formed in these systems at all. Accordingly, these results opened the possibility to explore ternary systems with Fe further. As an example, the design of Ti-Mo-Fe and Ti-Mo-Fe-Zr in the early 2000s paved the way to design new alloys with low cost and high mechanical strength [65,66]. As one can see in Figure 2.15, there is a reasonable field that allows a full β-solubilization (austenitization) in Ti-Nb-Fe alloys at 1000 ºC, for example.

At the moment we started this work (2015), only a few papers had been published exploring the Ti-Nb-Fe system in 15 years. Furthermore, most of them analyzed as-cast samples[2] of binary Ti-Nb alloys, varying the Fe content only [67,68]. With a similar strategy, Lopes et al. (2016) showed that additions of 1-5 wt.% Fe to Ti-30Nb alloys could induce significant strength improvements relative to the Ti-Nb binary system [69].

[2] Which are not optimal for such studies, since they are heterogeneous due to dendrite formation

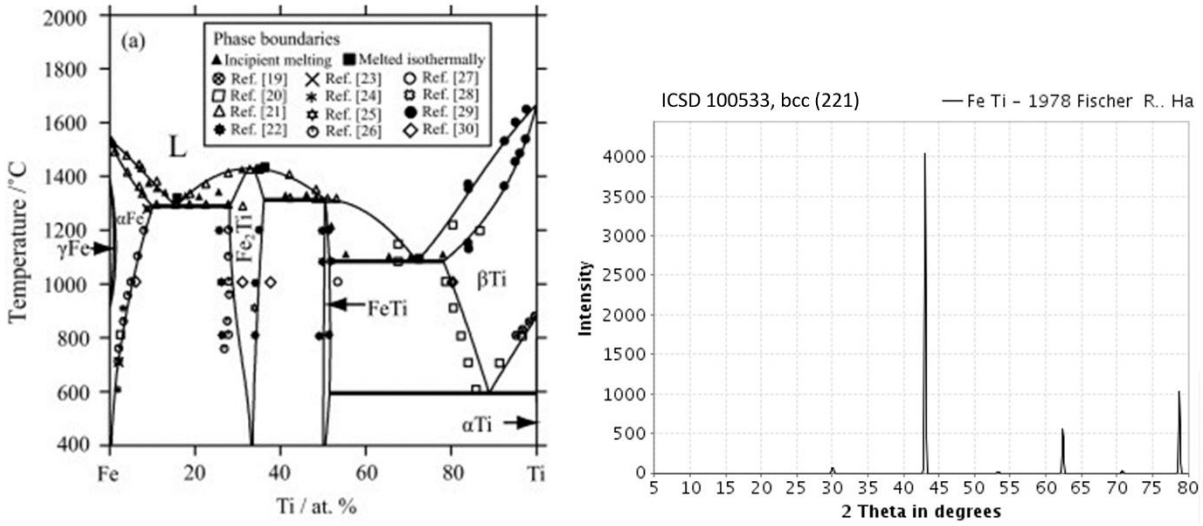

Figure 2.14 – The Fe-Ti binary phase diagram (left) and the ICSD chart for Fe-Ti intermetallic compound (right). Adapted from Wang et al. (2011) [70].

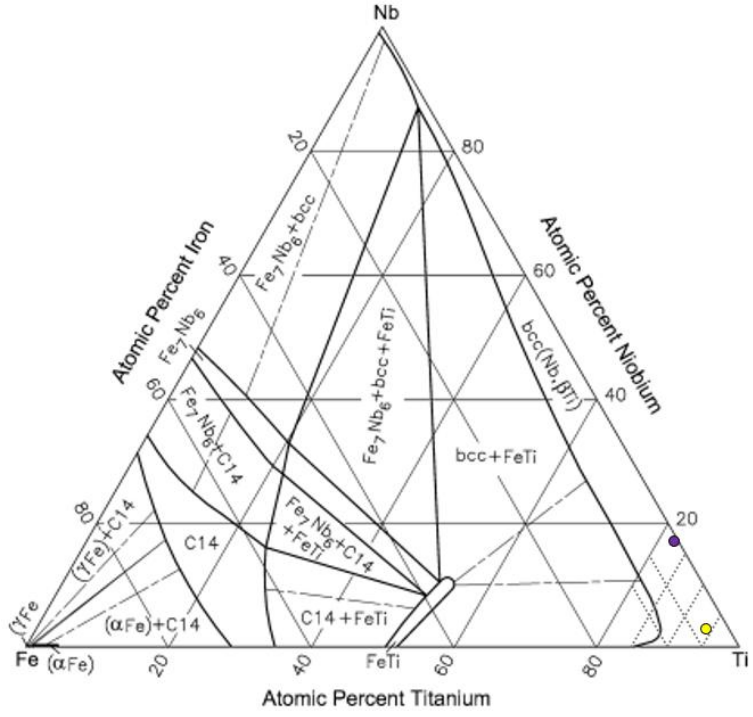

Figure 2.15 – A section of the Fe-Ti-Nb ternary phase diagram at 1273K (1000 ºC). The alloys Ti-11Nb3.5Fe and Ti-31Nb-1.0Fe (yellow and purple circles, respectively) which are explored in section 3 are indicated on the right side. Adapted from Raghavan (2012) [71]

In 2009, Cui & Guo designed a novel alloy named TNZF (Ti-28Nb-13Zr-0.5Fe wt.%). Forged samples subjected to ST-WQ presented yield strength of 800 MPa, elongation of 13% and an elastic modulus of 60 GPa. The microstructure was composed of primary β-grains and a small volumetric fraction of α". After aging at 450 °C for four hours, the precipitation of ω and α-phases led to an increase in yield strength and modulus to 950 MPa and 80 GPa, respectively [72]. This work, in particular, was the only one pointing to promising properties that could be achieved in the TNZF system.

The possibility of using Fe as an alloying element has also regained interest in the past years due to the consolidation of new processing routes based on additive manufacturing using low-cost TiH2 powder feedstock. In this case, Fe enhances the sinterability of AM pieces thanks to its high diffusivity in Ti, especially helping the initial sintering stage [73].

This thesis takes a new look at the possibility of using Fe as a minor alloying element, now in a quaternary system with additions of Zr and Sn. The selection of Zr and Sn as omega suppressor elements was not arbitrary. The addition of Zr and Sn can increase the energy barrier to ω-formation relative to other systems without these elements [74]. More information about the Ti-Nb-Fe system precursors is provided in Chapter 4 and Chapter 7.

2.7. Biocompatibility

According to Williams et al. (2008), materials for bioimplants are expected to be non-toxic, and should not trigger significant allergic, inflammatory or immune responses in the human body, to thus induce a stable equilibrium between material and host [75]. Despite concerning biomedical Ti-alloys, the focus of the present thesis was pointed to physical metallurgy and phase-transformations aspects of the Ti-Nb-Fe based alloys. In other words, we cannot attest that the experimental alloys presented here are suitable for bioimplants since no host response induced by the material was evaluated. Usually, in this respect, alloys are tested via electrochemical, in-vitro and in-vivo experiments, to evaluate corrosion degradation, wear resistance, cell proliferation, etc. These analyses are, therefore, suggested as future works.

Previous data by Biesiekierski et al. (2016) and Orzan et al. (2017) indicate there is no statistical difference in the proliferation of SaOS-2 osteoblasts between pure Ti (control) and

Ti-Nb-Fe, Ti-Ta-Fe and Ti-Nb-Ta-Zr alloys, after a 7-day incubation period [76,77]. Based on previous data (Figure 2.16), we expect the Ti-Nb-Fe based alloys designed here to behave similarly in respect to cell adhesion and healthy cell growth on the alloys' surfaces, which are good indicators preceding clinical trials.

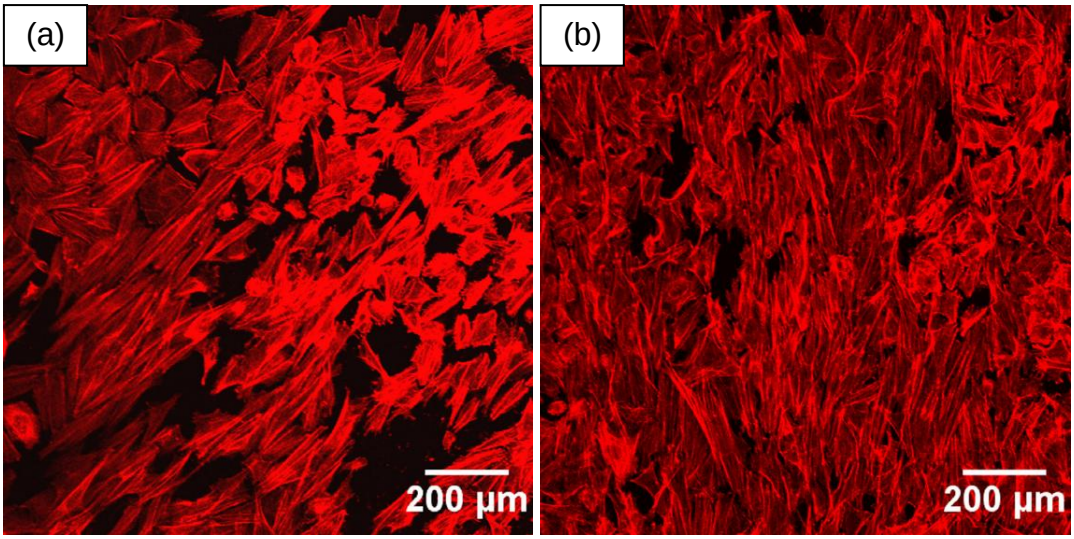

Figure 2.16 – Confocal micrograph of 7-day incubated osteoblasts cells on (a) Ti-12Nb-5Fe and (b) C.P. Ti (control). Adapted from Biesiekierski et al. (2016) [76].

2.8 Grain boundary reactions

As we know from classical metallurgy, sites of lower dimensionality – i.e., corners, edges, and grain boundaries - will contribute most to the nucleation rate at the early stages of nucleation. It happens due to the minimum free energy required to form a nucleus at these sites, which is lower than the homogenous nucleation barrier. On the other hand, the higher the dimensionality, the higher the availability of sites; therefore, when grain boundary reactions stop, they might continue at a slower rate inside the grains, up to saturation [78].

Intergranular embrittlement - also known as grain boundary (GB) embrittlement - is a common cause of failure in structural materials such as steels and Ni-base superalloys. Despite it has been known as a metallurgical impediment since the development of tempered alloy steels, it was only in the 70's that the GB embrittlement could be associated with the

segregation of residuals (Sb, P, As and Sn) and minor solute elements (Ni, Cr, Mn) to the grain boundaries, thanks to the development of Auger-electron spectroscopy. Previous works compiled by Guttman et al. (1980) showed that the segregation factors for certain residuals were increased by a factor of 5-10 in alloy-steels, compared to pure iron. In other words, alloying additions of Ni, Cr, and Mn[3] were proved to have a synergistic effect on the segregation of residuals such as P, Sn and Sb [79], increasing their equilibrium concentrations in the GBs. According to Stephenson et al. (1980), the segregation of Sn to GBs, for example, leads to a drastic reduction in fracture toughness and, of course, allows grain boundary cracks to form in rail steels [80].

Reactions involving grain boundaries are still a relevant subject nowadays. The advent of analytical techniques such as 3-dimensional atom probe tomography (3D-APT) and high-resolution transmission electron microscopy (HR-TEM) paired with a chemical analysis offers the possibility to observe solute segregation in non-brittle systems, such as Al and Ti-alloys [81]. As an example, in high-strength 7XXX aluminum alloys, all alloying elements (Zn, Mg, and Cu) segregate to the GBs upon water-quench. This segregation will later cause the formation of precipitate-free zones (PFZ) and, subsequently, allow coarse intermetallic phases to form along the GBs [82] if the microstructure is reheated. These microstructural features (Figure 2.17) are harmful to the mechanical and corrosion properties of many commercial-grade Al alloys [83].

Modern alloys also face an equivalent difficulty. In high-entropy alloys, the formation of intermetallic phases with hexagonal crystal structure at the grain boundaries upon cooling compromise room temperature ductility [84]. The same happens with β-metastable Ti-alloys since allotriomorphic (GB) α-phase often forms during aging. The presence of a continuous β-phase film in the vicinity of GBs is known as a soft region relative to the aged-hardened bulk, and under tensile/compression cycles, the film allows a faster crack propagation through these regions. GB segregations enable a major mechanism of transgranular crack propagation observed among aeronautical and biomedical Ti-alloys such as Ti-5553 [85], Ti-17 [85] and TNZT [86].

[3]That is for Ni, Cr and Mn. The addition of other stabilizing alloying elements (Ti, Zr) and carbide forming elements (Mo, V, W) causes the opposite effect, reducing the solubility of such residuals (mainly P e Sb) in the GBs, thus reducing embrittlement.

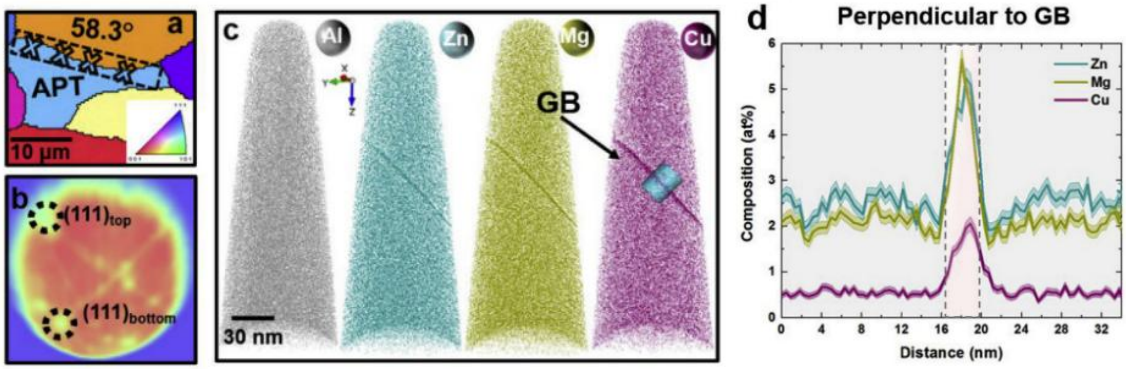

Figure 2.17 – APT analysis for a Al-Zn-Mg-Cu alloy in the as-quenched state: (a) EBSD-IPF map showing the grain boundary (GB) chosen for site-specific APT tip preparation; (b) Desorption map showing indexed crystallographic poles of two adjacent grains; (c) Atom maps of all elements in the as-quenched state; (d) Composition profile across the grain boundary in a 20 nm-diameter cylinder, taken along the z-direction. (Al, Zn, Mg, and Cu are depicted in grey, dark cyan, olive, and dark red, respectively). Extracted from Zhao et al. (2018) [87].

Given the limitations imposed by GB segregations on several metallic alloy systems, a model that allows us to describe the segregation/adsorption phenomenon to GBs seems extremely useful, especially to predict the likelihood of these events to take place based on composition.

In the case of steels, early attempts to model GB segregations were grounded on the assumption that segregations always occur in the way of reducing the interfacial free energy, due to a phenomenon referred to as equilibrium segregation. Accordingly, the saturation of solute elements at the GBs is inversely proportional to temperature. At temperatures close to RT, the segregation is pronounced. At intermediate temperatures (e.g., 600 °C), desegregation is often observed because of an entropic stabilization of the solid solution [79]. Another indication that GB segregations follow local-equilibrium conditions is observed in systems with intermetallic A_XB_Y compounds. In these systems, the maximum segregation of alloying element B at the GBs is given by $(X_B)_{MAX} = Y/(X+Y)$.

From a thermodynamic standpoint, segregation can be associated with a positive mixing enthalpy between main and solute elements (ΔH^{mix}). In a recent study, Xing et al. (2018) developed a simplified framework to estimate the grain boundary segregation in ternary alloys. The model allows us to observe the tendency of segregation of a given ternary alloying element (referred as C) based on the "effective enthalpy of GB segregation for C atoms in the ternary A-B-C system", or $\Delta H_{AC}^{seg-eff}$, an arbitrary variable which is a function of the binary enthalpies of mixing of the A, B and C elements - see Equation 1. The model uses as a reference one atom from a GB lattice model whose coordination number is 3. Since the coordination number can change depending on the crystal structure and grain orientations, coefficients a, b, and c were introduced to Eq. 1 for generalization purposes. By making use of the Equation 1, the authors could foretell that Pd should be segregated to GBs in the Pt-Au-Pd system, at a specific temperature range [88].

$$\Delta H_{AC}^{seg-eff} = \Delta H_{AC}^{seg(bin)} + a\Delta H_{AB}^{mix} - b\Delta H_{AC}^{mix} - c\Delta H_{BC}^{mix} \quad (1)$$

where the constants a, b, and c are positive numbers which are not greater than one.

To validate the model and explain it in the details, the authors obtained Pt-Pd and Pt-Au-Pd alloys via magnetron sputtering, which were then subjected to thermal heat-treatments at an optimal temperature. In the Pt-Pd system, Pd was not segregated - after all, the enthalpy of mixing of Pt-Pd is close to zero. On the other hand, in the presence of Au, which was strongly segregated to GBs, Pd tended to be co-segregated. As the enthalpy of mixing of Pd-Au is negative, Pd-Au bonds tend to be preserved, causing segregation of Pd induced by Au. In summary, the model proposed by Xing et al. (2018) is relatively simple, yet it has been proved to be very useful. The availability of enthalpy of mixing data, CALPHAD techniques, the consolidation of the Miedema model and the ability of nowadays obtaining the enthalpy of mixing between virtually any pair of elements with atomistic techniques (such as molecular dynamics), could aid further refining the model [89].

2.9 Diffusion through grain boundaries

Grain boundary diffusion is a key process in polycrystalline materials since it can occur at 4 to 8 orders of magnitude faster than bulk diffusion. Nevertheless, GB diffusion is known as an intricate process combining (1) volume diffusion to a surface, (2) diffusion along the GBs, (3) leakage of diffusers from the GB to the volume and finally (4) volume diffusion around GBs. For that reason, it is hard to generalize the exact mechanism of diffusion through GBs among metallic materials. Most mathematical treatments of GB diffusion are based on Fisher's model, whose equations can be solved analytically [90]. Arrhenius plots typically represent diffusion kinetics (including GB diffusion). Commonly, diffusion kinetics falls into at least one of the three of the well-known Harrison's regimes. Volume diffusion becomes less and less important as we move from regime A to regime C. In other words, under kinetic regimes B and C, grain boundary diffusion and other fast pathways play a dominant role on the overall solute diffusivity. [91]. In kinetic regime type C - which is activated with larger grain size, low temperatures and extremely short annealing times - diffusion happens only through the GBs. Therefore, this kinetic regime is the only one that allows isolating the grain boundary diffusion coefficient [92]. All this information is relevant to this work since we adopted an experimental setup that we could activate kinetic regimes B-C, making GB diffusion important to interpret the results.

It is worth reminding that our experiments are very simple compared to experiments that focus on diffusion behavior alone. GB diffusion experiments often encompass the use of radiotracer solute elements that can be easily identified to compute the solute penetration profiles at the desired temperature [92,93]. To better evaluate diffusion, multiple experiments at different kinetic regimes are needed. More details about such experiments are extensively discussed in the works of Herzig et al.[4], especially on Chapter 8 in the book Diffusion in Condensed Matter [91].

In the event of a simultaneous phase formation at the GBs while GB diffusion occurs, additional aspects must be considered, such as the creation of an interface (on both sides), and differences on the diffusivity of each phase, depending on its crystal structure and the perpendicular direction to the GB. These aspects add even more complexity to the diffusion phenomenon, which is already intrinsically hard to characterize.

[4]The diffusivity data available in the literature is most times a result of approximations assuming a typical grain boundary width of 0.5 nm and segregation factors of 10^1-10^5, depending on the experimental procedure.

According to some fundamental aspects of diffusion in Ti-alloys described by Lutjerig and Williams (2003), Fe exhibits an abnormally fast diffusion in beta-Ti, which can be attributed to an interstitial diffusion mechanism. Another interesting aspect of Fe as an alloying element is that Fe presence as impurity changes the diffusion of other substitutional alloying elements, such as Al. [7]. The diffusion behavior in our system will be treated in Chapter 6.

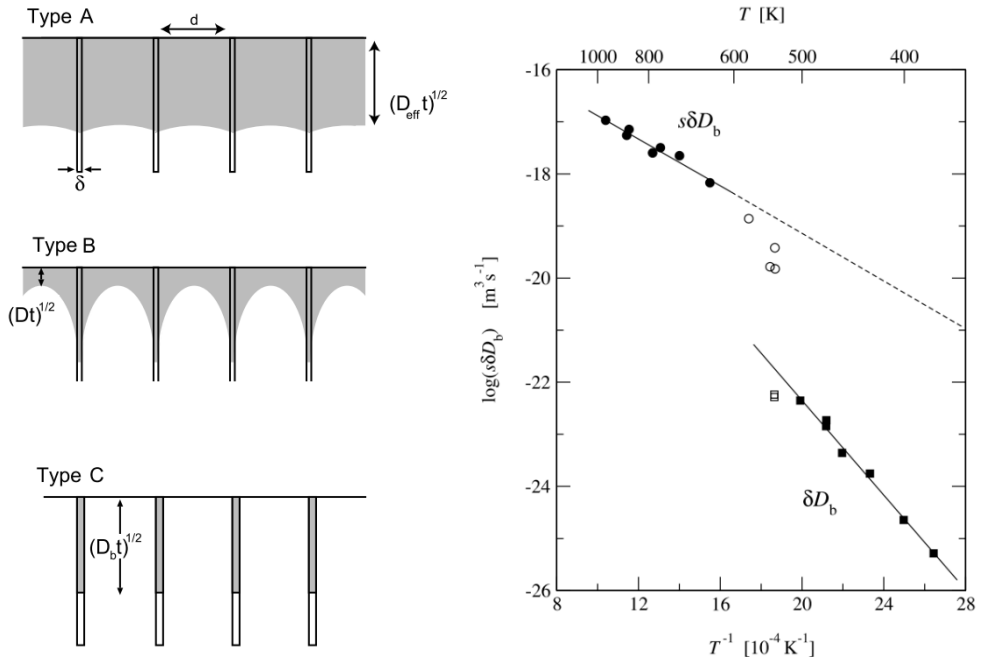

Figure 2.18 – Left - schematic illustration of type A, B and C diffusion regimes in Harrison's classification. The gray shade represents the penetration of the tracer atom for each Kinect regime. Right - Arrhenius plot of for Te impurity diffusion along GBs in Ag evidencing the transition between type B (> 500K) and type C regimes. Both Figures were adapted from Heitjans et al. (2005) [91].

3 EXPERIMENTAL PROCEDURE

3.1. General sample preparation

High-purity precursor metals were employed to the ingots manufacturing. Grade 2 Ti (99.7%) and high-purity Nb (99.9%) pieces were subjected to chemical pickling to remove surface oxide layer before melting. Other metals were employed in the form of powder or

granules. Before melting, the fusion chamber was flushed three times with argon and vacuum cycles. Arc-melting was carried through in a water-cooled copper crucible using a non-consumable electrode, under a protective argon atmosphere. After solidification, all ingots were encapsulated in quartz tubes filled with Ar to be homogenized at 1000 °C for 12 h, followed by water-quenching (WQ). Homogenization is important to break the dendrites and assure chemical homogenization. From there, two divergent experimental routes were adopted: (1) cold-rolling or (2) hot-swaging.

For the cold-rolled samples, they were deformed up to 20% of their original thickness with a 0.2 mm reduction per pass. Most compositions presented an excellent cold-formability, excluding Ti-15Nb-3.0Fe and Ti-11Nb-3.5Fe based alloys. The reduction in thickness in these alloys was limited to 50% to prevent the growth of edge cracks generated during processing. Samples with 10 x 10 x 2 mm thickness were cut from the plates using a diamond-abrasive saw. All cold-rolled samples were subjected to a recrystallization/solution heat treatment step at 750-800 °C (above β-*transus*) for 10 min before aging. After all, these flat samples were the ones used to a preliminary investigation of the phase transformations during aging employing hardness tests, elastic modulus measurements, and X-ray diffraction analyses. They were also used to produce the compressive test specimens with Ø 2×4 mm, that were obtained via a wire erosion in an electrical discharge machine (EDM). Cylindrical, hot-swaged samples were selected to the tensile tests. Ingots were heated up 1000 °C and then hot-swaged with a reduction of approx. 3 mm in diameter each step (four to five forging steps total), down to 9 mm. Cylindrical tensile specimens with 4 mm of diameter and 26 mm of gauge length were then milled from the bars and subjected to the desired heat-treatment. Fixation at the universal testing machine was done at both edges by M8 threads.

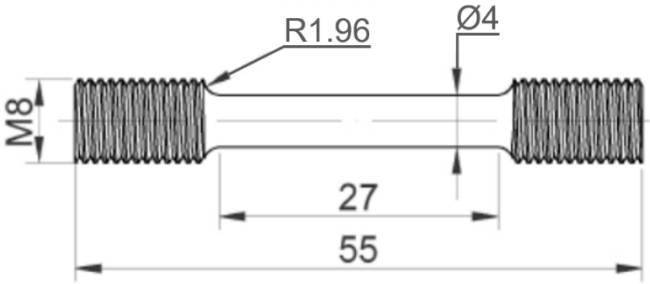

Figure 3.1 – Cylindrical tensile specimens.

3.1. Heat treatments

The condition referred to “initial condition,” or “WQ” through this text comprehends a basic recrystallization/solution heat-treatment followed by water quenching. Other common heat-treatments performed were the solution-heat-treatment followed by furnace cooling ST-FC), and the step-quench heat-treatments, in which the samples were directly aged (from the high-ST temperature) to several temperatures of interest. The step-quench heat treatment involved quickly moving the quartz tube containing the samples between two hot zones previously set to 800 °C and the aging temperature of interest, respectively. From previous measurements with thermocouples, the cooling rate between ST and the aging temperature was estimated to be near 600 K/min.

In this work, we did not explore classical quench-and-aging heat-treatments, since we were trying to avoid the formation of ω-phase while re-heating the microstructure [94].

3.2. General characterization

For the general characterization, all samples were metallographically prepared by sanding to #1500 grit sandpaper and polishing using a VibroMet® with 0.02 μm colloidal silica suspension. When necessary, it was employed a colloidal silica and H_2O_2 (3% v/v) solution for manual-polishing. Samples analyzed by optical microscopy were etched using standard Kroll’s reagent (6 ml HNO_3 + 2 ml HF + 92 ml distilled water) to reveal the phases in the microstructure.

The chemical composition of the experimental alloys (Table 3.1) was determined via X-ray fluorescence spectroscopy (Shimadzu EDX7000). Interstitial elements O and N were determined by the inert gas fusion method using a LECO TC400 analyzer. Vickers hardness measurements were obtained with a Buehler Vickers 2100 hardness tester, applying an indentation load of 1 kgf load applied for 15 s. Elastic modulus measurements of the 2 mm thick samples were taken using a pulse-echo Panametrics NDT 5072PR emitter-receiver equipped with 7.5 mm round transducers operating at a frequency of 5 MHz, as specified by ASTM E494 (2005) [95]. The results of hardness and elastic modulus expressed in the following text are based on the average and standard deviation of five measurements.

Table 3.1 – Composition of the 17 experimental alloys (wt. %); Ti in balance.

Alloy (wt. %)*	Nb	Fe	Zr or Sn	O	N
Ti-31Nb-1.0Fe	29.9 ± 0.2	1.1 ± 0.1	-	0.14 ± 0.02	0.007 ± 0.002
Ti-27Nb-1.5Fe	26.7 ± 0.5	1.6 ± 0.1	-	0.13 ± 0.01	0.009 ± 0.001
Ti-23Nb-2.0Fe	22.8 ± 0.4	2.2 ± 0.1	-	0.13 ± 0.02	0.008 ± 0.001
Ti-19Nb-2.5Fe	18.3 ± 0.2	2.7 ± 0.1	-	0.16 ± 0.01	0.011 ± 0.001
Ti-15Nb-3.0Fe	14.8 ± 0.2	3.0 ± 0.1	-	0.17 ± 0.01	0.008 ± 0.001
Ti-11Nb-3.5Fe	11.0 ± 0.1	3.7 ± 0.1	-	0.18 ± 0.02	0.011 ± 0.002
Ti-11Nb-3.5Fe-7Zr	10.9 ± 0.1	3.7 ± 0.1	7.1 ± 0.1	0.164 ± 0.004	0.011 ± 0.001
Ti-11Nb-3.5Fe-4Zr	11.0 ± 0,1	3.7 ± 0.1	4.1 ± 0.1	**	**
Ti-19Nb-2.5Fe-6Sn	18.6 ± 0.5	2.6 ± 0.1	5.8 ± 0.2	0.128 ± 0.004	0.017 ± 0.001
Ti-19Nb-2.5Fe-7Zr	18.2 ± 0.1	2.8 ± 0,1	7.2 ± 0,1	**	**
Ti-19Nb-2.5Fe-10Zr	18.9 ± 0.1	2.7 ± 0.1	10.1 ± 0.1	0.157 ± 0.001	0.007 ± 0.001
Ti-19Nb-2.5Fe-13Zr	18.9 ± 0.5	2.7 ± 0.1	13.2 ± 0.1	**	**
Ti-23Nb-2.0Fe-10Zr	22.2 ± 0.6	2.3 ± 0.2	9.9 ± 0.3	0.186 ± 0.002	0.006 ± 0.002
Ti-27Nb-1.5Fe-7Zr	24.8 ± 0.4	1.7 ± 0,2	7.1 ± 0.2	**	**
Ti-27Nb-1.5Fe-10Zr	26.1 ± 0.3	1.5 ± 0.1	10.1 ± 0.1	0.140 ± 0.009	0.014 ± 0.004
Ti-27Nb-1.5Fe-13Zr	25.4 ± 0.3	1.6 ± 0.1	13.1 ± 0.1	**	**
Ti-31Nb-1.0Fe-10Zr	29.7 ± 0.8	1.3 ± 0.2	10.2 ± 0.2	0.131 ± 0.002	0.08 0.002

* Throughout the text, compositions are often referred to as number alone, in this same order, e.g.: 3110 = Ti-31Nb-1.0Fe; 192510 = Ti-19Nb-2.5Fe-10Zr.

**O and N interstitials were not determined for these compositions.

Samples were also analyzed by X-ray diffraction (XRD) in a PANalytical X'Pert Pro diffractometer operating with a Cu-Ka radiation source at 45 kV and 35 mA. The diffractometer was equipped with a PIXcel fast detector and a spinner sample-holder. Yttria powder was tested to obtain the XRD instrument calibration file. The diffraction patterns were then analyzed using the EXPGUI/GSAS program suite.

To detect phase-transformation temperatures, samples were subjected to DSC measurements using a NETZSCH STA 409 C flushed with argon. Both heating and cooling rates were 25 K/ min, and the scans were completed over a wide temperature range, from RT (298 K) up to 800 °C (1073 K) – i.e., above β-*transus*. The samples for the DSC experiments weighed approx. 70 mg.

Scanning electron microscopy (SEM) analyses were performed with four microscopes: Tabletop Hitachi 200, an FEI Sirion, an FEI Quanta 650 FEG and an FEI Apreo system, all of them equipped with BSE detectors. As for TEM, four microscopes were employed: a JEOL 2100F, am FEI Tecnai F20, an image-corrected Titan G2 (The Ohio State University) and a

double-corrected Titan cubed Themis (CNPEM/LNNano). TEMs operated at 200kV or 300kV accelerating voltage. For the STEM measurements, the probe size of the electron beam was maintained at 1.0 nm. High angle, annular dark-field (HAADF) imaging were performed on the Tecnai F20 with a convergence semi-angle of 15 mrad at a camera length of 115 mm. The solid angle detection for the XEDS detector was 0.3sr. Images recorded on the Titan were obtained with a convergence semi-angle of 12 mrad and a camera length of 91 mm. Titan G2 was equipped with FEI ChemiSTEM technology (4 XEDS detectors).

3.3. TEM characterization

Although transmission electron microscopy is a subject in its own, a brief introduction is provided here with the aim of informing the reader about our approach to the characterization performed in this work. For a detailed review on TEM, please refer to the books by De Graef (2003), Williams and Carter (2009) and Chapter 8 from Physical Metallurgy, by Hamish et al. (2014) [96–98].

Very often, metallurgists employ conventional TEM imaging techniques, which rely on diffraction contrast, to characterize their samples. Conventional TEM is particularly good when the aim is to isolate secondary-phases based on their crystal structure, and for the characterization of dislocations or planar defects. As an example, conventional TEM was extensively employed in this work to verify the presence of ath-ω among ST-WQ samples. However, high-resolution images in the conventional TEM mode can be complex, since they incorporate phase contrast imaging.

Scanning transmission electron microscopy (STEM), on the other hand, has become the preferred technique for high-resolution imaging, due to the improvements of spatial resolution afforded by STEM in modern microscopes. In STEM, a condensed probe inspects the whole specimen, spot by spot, while recording signals that are later used to form an image. With the advent of high-angle annular dark-field (HAADF) detectors (Figure 3.2), it is possible to obtain images based on Z-contrast (differences in atomic numbers), simultaneously with elemental mapping techniques, such as X-ray Energy Dispersive Spectroscopy (XEDS) and Electron Energy-Loss Spectroscopy (EELS, which will not be treated here).

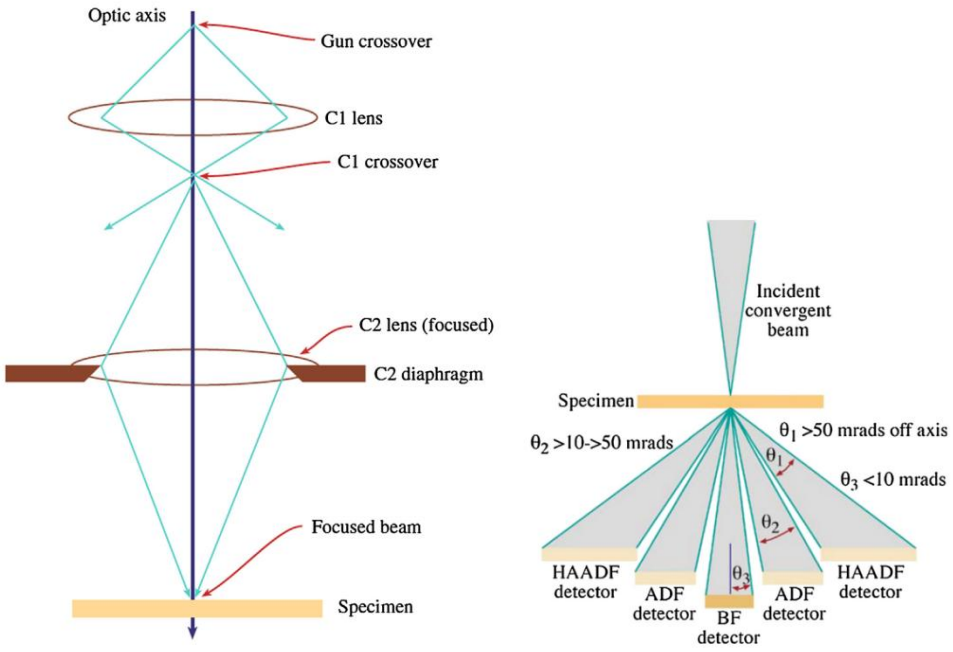

Figure 3.2 – Left - A schematic diagram of the electro-optical configuration in a STEM condition with two condenser lenses. Right - A schematic diagram depicting a common detector setup that allows for a collection of a large angular range of scattered electrons after the specimen. Extracted from Williams & Carter (2009) [97].

For the X-ray energy dispersive spectroscopy (XEDS), the specimen excitation due to the interaction with the electron beam probe causes a local emission of specific X-ray photons, according to the composition of the specimen. One interesting aspect of this phenomenon in the TEM is that since TEM foils usually have less than 300 nm in thickness - and given that probe sizes can be the size of angstroms - the beam interaction volume is very small, compared to bulk samples (Figure 3.3). Therefore, the spatial resolution of STEM is way better than electron-probe microanalysis (EPMA), performed on the SEM. According to Hamish et al., other significant advantages of using STEM are that thin foils produce (1) much-reduced effects of fluorescence and absorption, and (2) a low-intensity background spectrum. These aspects are very important since they simplify the process of making the quantification of the XEDS data.

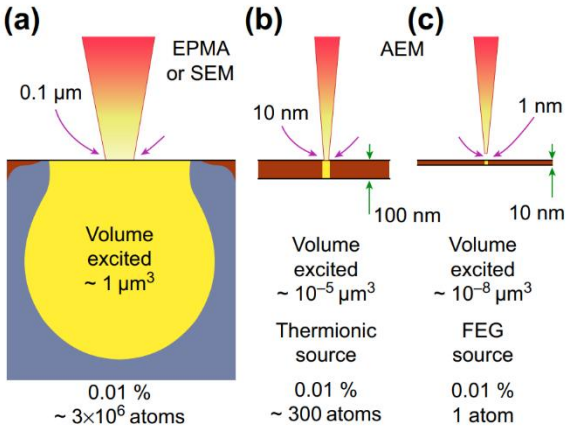

Figure 3.3 – Schematic diagram of the volume excited in bulk samples and thin foils. Extracted from Fraser et al. (2014) [98].

In this work, we employed STEM + XEDS to measure the compositional differences between the β-matrix and the α-plates. For the quantification of XEDS spectra, we used FEI's proprietary software with its native K-factors. After preliminary tests with a Ti-11Nb-3.5Fe-7Zr at the ST-WQ condition, the composition obtained via STEM + XEDS was less than 10.4 wt.% Nb, while the nominal composition was 10.9 ± 0.1 wt.%, obtained by XRF. We assumed this deviation to be irrelevant given other uncertainties associated with the alloy production and proceeded with the use of the native K factors for all data shown through this document. Previous works with a similar experimental setup reported that the difference between the Mo content in a TiNbTaMoZr alloy quantified externally (EPMA) and the one obtained with native K-factors could deviate 25% from the nominal composition, therefore, the development of average intensity experimental K-factors was necessary. The procedure to develop such experimental K-factors for metallic samples was reported in detail by Jensen (2017) [99]. For more information on XEDS quantitative analysis, please refer to Newbury et al. (2015) [100].

3.3.1 TEM of Ti alloys

Images are preferentially recorded through a low-index zone axis to analyze Ti-alloys in the (conventional) TEM mode. The best zone axis to characterize ω-phase is the [110]β, because the displacement vector of atoms needed to form ω is perpendicular to this direction, as represented in Figure 3.4a. Consequently, the projection of atoms in the [110]β direction is unique and allows one to directly observe the degree of ω collapse and possibly identify partially collapsed ω regions (also known as trigonal-ω), which are commonly observed at the β-ω interfaces [101,102].

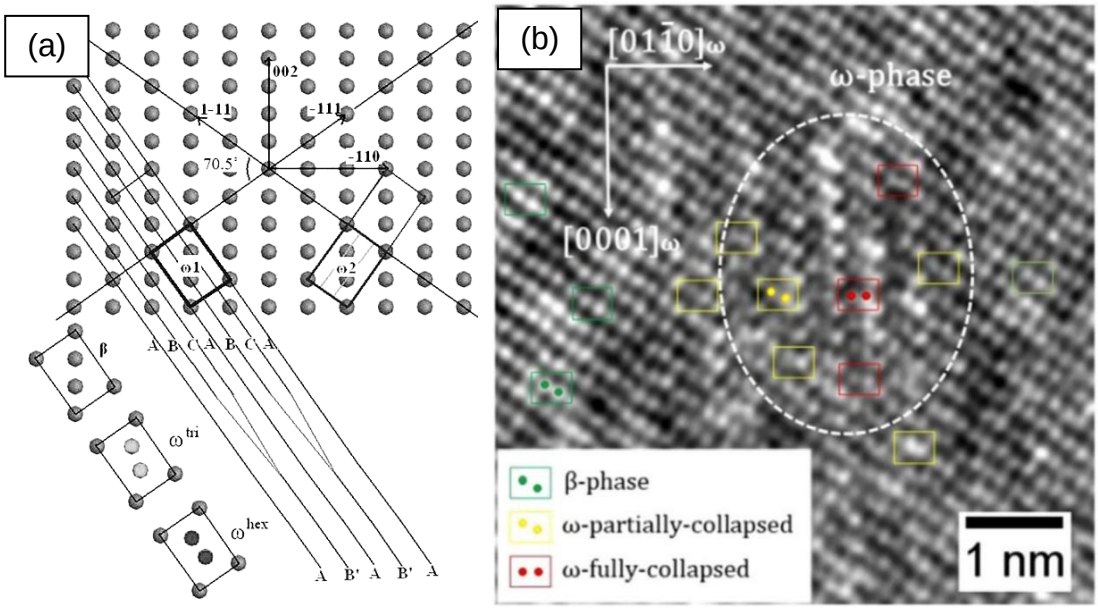

Figure 3.4 – (a) Projection of atoms in the [110]β direction, adapted from George et al. 2017 [103]. (b) A high-resolution image of a ω-precipitate found in Ti-5553.

Based on a collection of experimental selected-area-diffraction (SAD) patterns, other useful zone axes in which ω-phase can also be easily identified by secondary maxima spots and characteristic diffuse arcs are [102]β and [113]β. Diffraction patterns from [100]β and [111]β zone axes are not recommended to analyze ω-phase since they do not show any strong ω-phase spots. Given that there are four ω variants, a common misunderstanding is that each

quadrant (with four spots) is associated with a single ω-variant. However, there are always two distinct variants linked to a quadrant, as revealed in Figure 3.5.

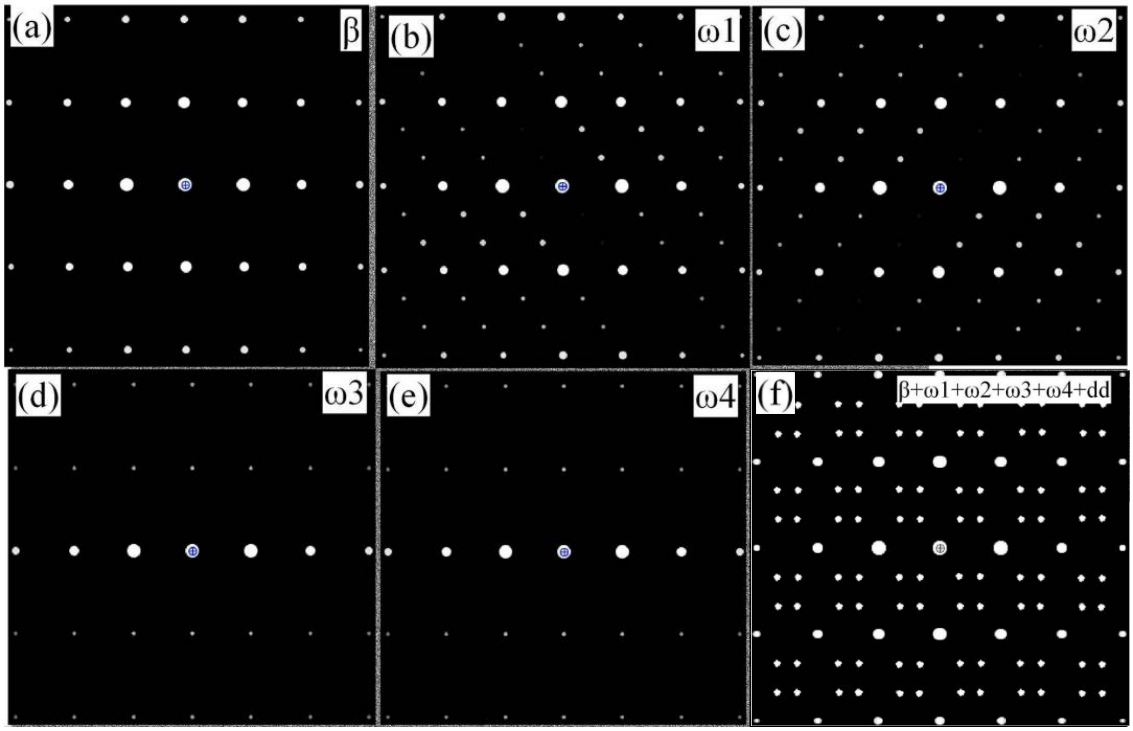

Figure 3.5 – Simulated diffraction patterns using the EMS software (Stadelmann 1987) [104] of (a) [110]β; (b) [2110]ω1; (c) [2110]ω2; (d) [1014]ω3; (e) [1014]ω4; (f) superimposed pattern of β and all variants of ω phase including double diffraction spots. Adapted from George et al. 2017 [103].

In addition to the secondary spots which can be associated with ω-phase, the [110]β also have well-defined α-spots, as presented in Figure 3.6. Considerable attention must be paid when analyzing α-phase double diffraction spots since they can be mistaken by ω-phase. To avoid this misinterpretation, note that the α-phase spots are always off-centered relative to the vectors g = [112]β, while the ω-spots precisely occupy the g = 1/3 [112]β, right on the axis.

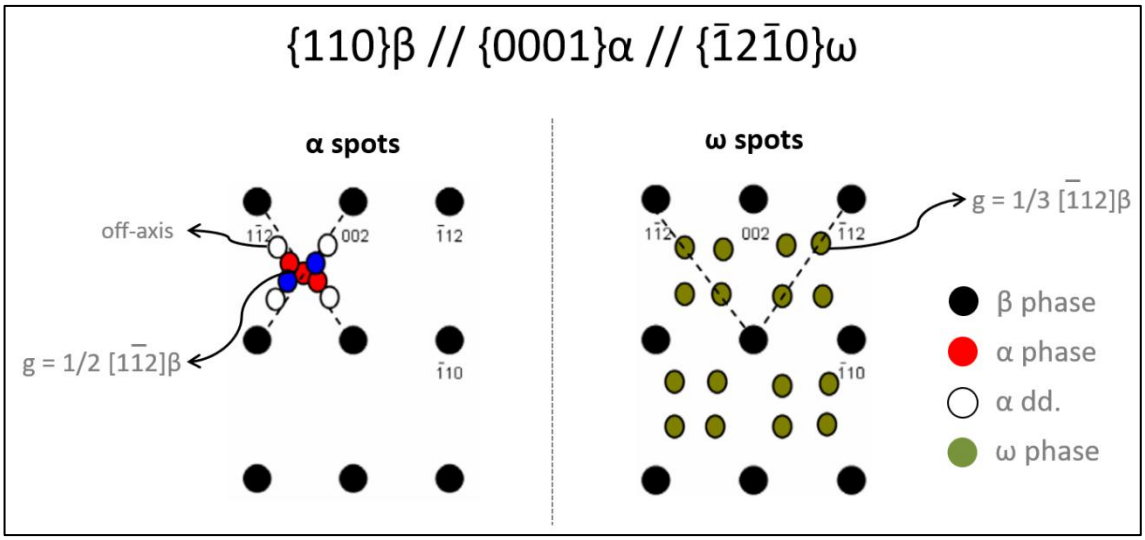

Figure 3.6 – A representation of the reciprocal space for β+α (left) and β+ω (right) through the [110]β zone axis. Adapted from Wu et al. 2006 [105].

3.3.2 TEM sample preparation

TEM samples were prepared in 2 ways. Initially, specimens were prepared by conventional 3 mm disks extraction, followed by dimpling (3 μm alumina) and argon ion milling at cryogenic temperatures. On the other hand, we employed the method commonly known as "lift-out" to obtain the FIB lamellae. In this method, a TEM foil/specimen is extracted from the bulk samples, at site-specific regions, and then it is transferred to an appropriate TEM grid with the aid of micromanipulator and a Dual-Beam Focused-Ion-Beam (DB-FIB) FEI Helios system.

Beyond the conventional lift-out technique, we used cross-referenced coordinates to the FIB foils from site-specific regions, containing the region-of-interest (in this case, the grain boundaries) at the exact 1/3 left portion of the foil - see Figure 3.7. This positioning enables a straightforward thinning process since the location of the ROI is known before starting thinning the foil. The lift-out technique is illustrated in Figure 3.8.

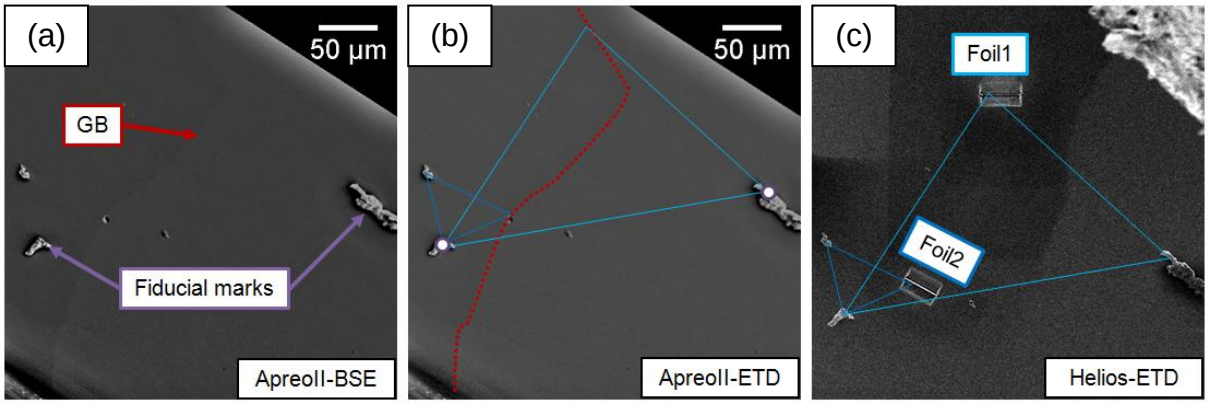

Figure 3.7 – The position of grain-boundary site-specific foils extracted from Ti11Nb-3.5Fe-7Zr aged for 1 min at 450 deg C. (a) "fiducial" marks, (b) coordinates and (c) final extraction.

It is important not to exceed 0.46 nA when using a high-voltage (20-30 kV) to avoid an extensive damage layer due to the Ga+ ions sputtering during the thinning process. Also, it is recommended to always mill from the outer edge of the foil towards the Pt deposition, avoiding Pt penetration to the foil and the occurrence of an undesirable "curtain effect." Thinning should alternate between the front and the back face of the foil (up to ± 2 degrees). According to Yu et al., an excessive incident angle can cause a large amount of Ga implantation, to the point of allowing the formation of Ga intermetallics [106]. From our experience, if the operator is careful with the preliminary thinning, low voltage (5 kV), cleaning steps should not be necessary for conventional TEM or low-magnification STEM analyses. If needed, low voltage cleaning steps should be executed the opposite way – from the platinum protected region to the outer edge of the foil.

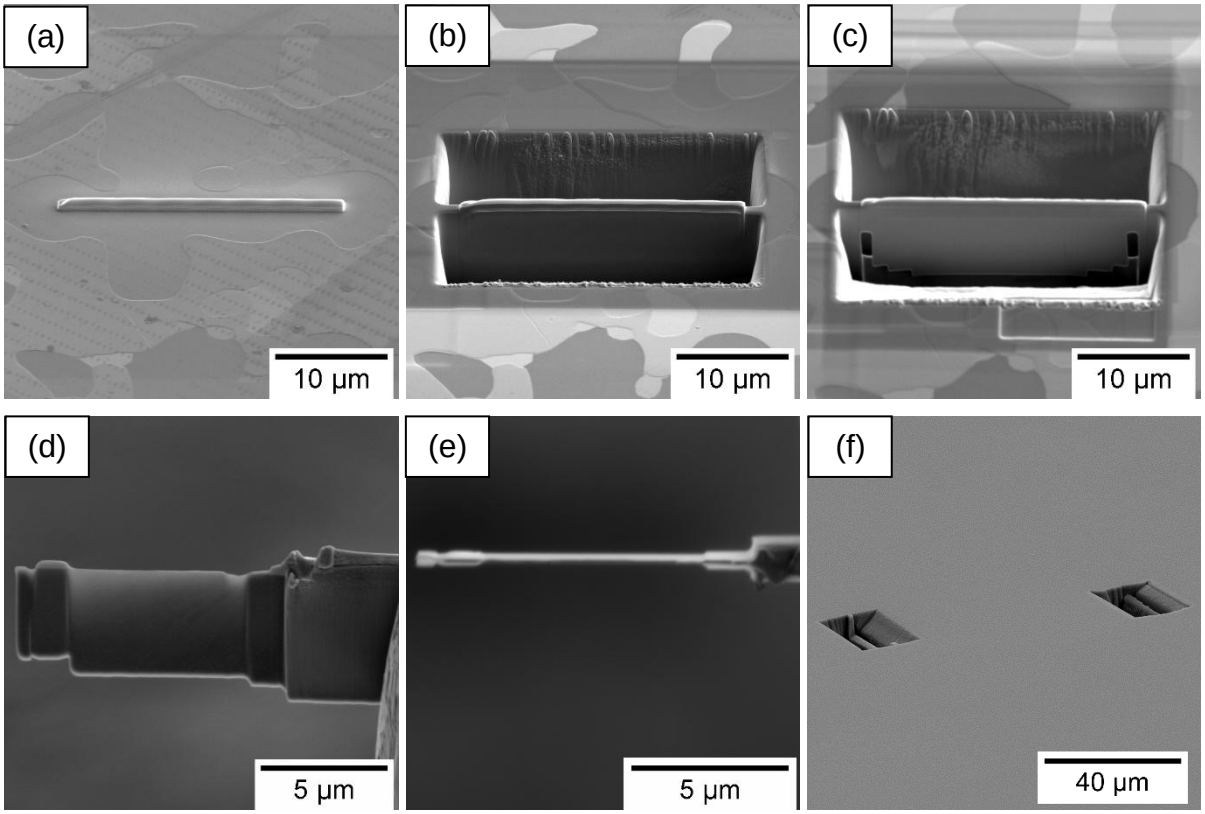

Figure 3.8 – The process of a foil extraction: (a) platinum deposition on the region of interest, (b) milling the trench, (c) milling the undercut, (d) top view of the foil fixed at the copper grid after preliminary thinning steps, (e) adjustment of the thickness of the foil, recorded with the ion-beam. Image (f) was added to illustrate the regions after the foil extraction.

To get rid of the damaged/amorphous layer induced by the focused-ion-beam, an additional gentle ionic milling step with low voltage is recommended. A few samples – especially the ones that were prepared to HRTEM – were subjected to this step. The final milling was performed on a NanomillTM Fischione Instruments, model 1040, at cryogenic temperatures. Samples were polished by an ion-beam projected on the ROI (approx. 15 x 5 microns), at an incidence angle of plus or minus 10 degrees of the surface. The first step was performed with 900 eV of acceleration for 7 min, and the second with 500 eV for 5 min, on each side. Emission current was set to 150 uA, which results in an effective ion-current of approx. 150 nA, depending on the atomic mass and thickness of the foil-target [107]. The thickness of our foils was estimated to be close to 70-80 nm, which is good for STEM-EDS at intermediate magnifications, up to 120.000x (i.e., with probe-sizes of 0.5-1 nm). In the case of high-resolution STEM-EDS or EELS measurements, the foils should be 10-50 nm thin [108].

4. EXPLORING THE TERNARY SYSTEM

The Ti-Nb-Fe ternary system is a relatively low-cost system with a potential for future long-term implant applications. To find the point of cost-effectiveness among Ti-Nb-Fe based alloys, in this chapter, we examined six novel compositions to ascertain the dependence of the elastic modulus on the Nb/Fe atomic ratio after water- quenching (WQ), furnace-cooling (FC) and isothermal aging at 350 °C. We chose Nb and Fe as alloying elements because Fe is the most common impurity in Nb ore; therefore, Fe-Nb master alloys usually cost about 20 times less than the vacuum grade Nb required for isolated Nb alloying. Mechanical properties such as the elastic modulus, hardness, and compressive yield-strength were evaluated. Furthermore, with the aid of DSC measurements, transformation temperatures (especially ω-*solvus*) in each alloy were detected and to confirmed via microstructural characterization.

4.1. Background

Several authors have investigated the addition of Fe to binary Ti-Nb alloys in recent years. Ti-5Nb-xFe, Ti-xNb-3Fe and Ti-30Nb-xFe alloys have been studied [67–69,109], with added Fe contents ranging from 1 to 7 (wt. %). Significant conclusions have been drawn from these previous works: A) Fe plays an important role as a β stabilizer element, reducing the martensite start temperature (Ms) and thus reducing α″ stability, thereby enabling the β phase to be metastable at room temperature [110]. B) Essentially, the ω phase is present in most of these compositions after rapid cooling from the β phase field, which is a controversial observation, considering the Bo−Md diagram predicts that Fe-rich alloys are fully β [69]. C) Fe increases the mechanical strength mainly due to solid solution strengthening [111]. D) Based on observations by Costa et al. 2016 [112], small additions of Fe, up to 1 wt. %, are enough to strongly refine α-phase distributions in Ti-Nb alloys subjected to low heating rates[5] - as shown in Figure 4.1.

[5] This conclusion, drawn by Costa et al (2016) in a collaboration with our group, has not been fully explored yet. It was not explored in this work either, since we did not perform classical quench and aging heat-treatments.

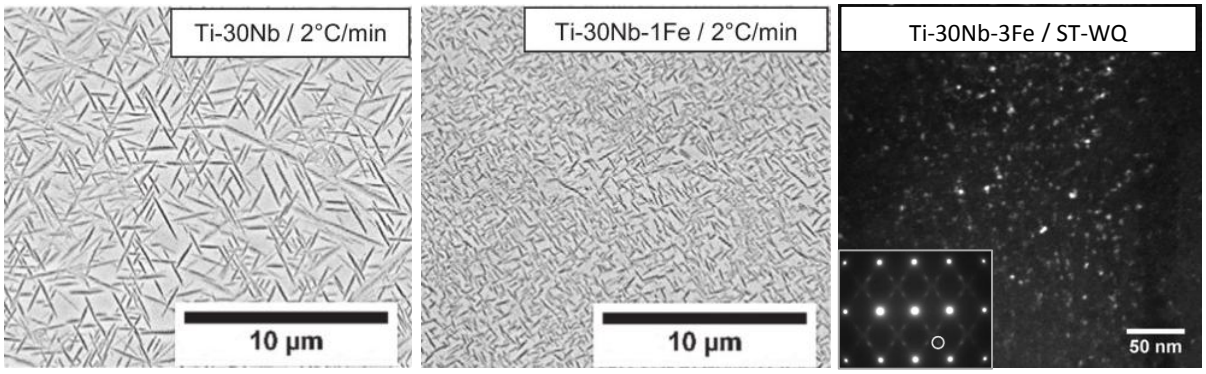

Figure 4.1 – The effect of 1 wt.% of Fe addition on Ti-30Nb (a, b) at the same heat-treatment condition and a dark-field image showing ω-precipitates in Ti-30Nb-3Fe (inset – SAD through <110>β). Adapted from Costa et al. 2016 [113].

Recent exploration by Ehtemam-Haghighi et al. assessed several mechanical properties of the Ti-Nb-Fe system in two papers, paying attention to Ti-11Nb-xFe alloys with Fe contents of 0.5, 3.5, 6 and 9 wt. % and a Ti-xNb-7Fe alloy. However, the authors did not evaluate the thermal stability of the alloys as mentioned earlier [111,114]. Notwithstanding all this attention, no study so far has systematically explored the changes in transformation temperatures and mechanical properties as a function of the Nb/Fe ratio.

4.2. Alloy design

As mentioned earlier, many biomedical-grade titanium alloys have been developed using the $\overline{Bo} - \overline{Md}$ diagram. However, no systematic study of Ti-Nb-Fe alloys has been done. Our proposal in this work was to study a broad range within the diagram to verify the behavior of these alloys in response to varying Nb/Fe ratios. Six different alloys were produced. The first composition chosen was Ti-31Nb-1.0Fe (wt. %), which is similar to the Ti-30Nb-1Fe (wt. %) investigated in a previous study [69]. Step-by-step, 4Nb (wt.%) was replaced with 0.5Fe (wt.%) until the Ti-11Nb-3.5Fe composition was reached. This substitution took into account the Mo equivalent number [Mo]eq., an indication of the β phase stability for the Ti-Mo binary system, which ranges from 11 to 12 among the experimental alloys. The Mo equivalent was calculated according to the equation provided by Weiss et al. (1999) [115][6].

[6] [Mo]eq = Mo + 0.6V + 0.44W + 0.28Nb + 0.22Ta + 1.25Cr + 1.25Ni + 1.7Co + 2.5Fe

Table 4.1 describes the electronic parameters computed for each of the experimental alloys. The $\overline{\mathrm{Bo}}$ and Md parameters were calculated taking the compositional average of every element [58]. Figure 4.2 shows the alloys in the $\overline{\mathrm{Bo}} - \overline{\mathrm{Md}}$ diagram. As can be seen, all the experimental alloys are located on the left-hand side of the β / β+ω phase boundary, which implies that when these alloys are subjected to water-quenching from the β phase field, they should present a full β structure. However, it is worth reminding that the position of this boundary line is not exact.

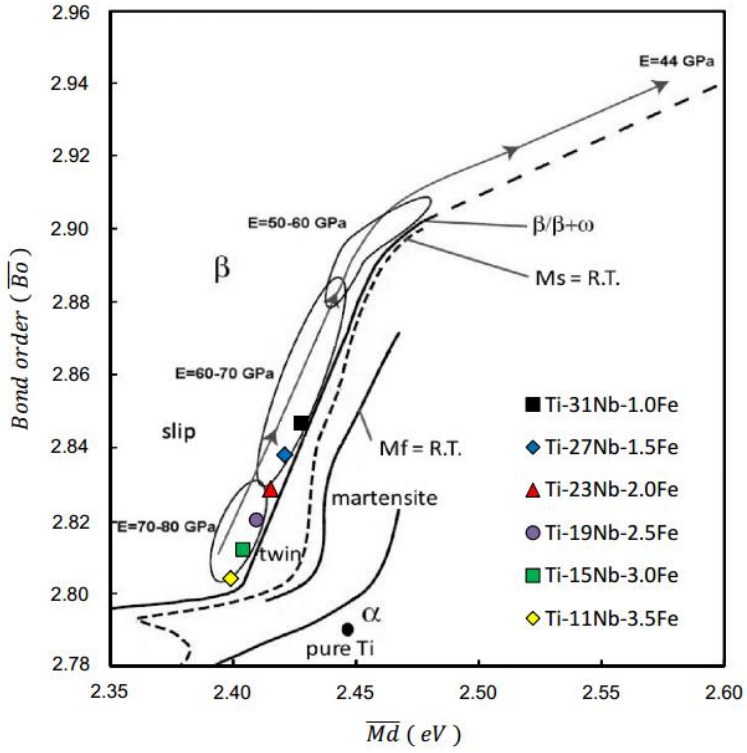

Figure 4.2 – Experimental alloys placed in the original $\overline{Bo} - \overline{Md}$ diagram

Concerning other relevant parameters, the higher the Fe content, the fewer valence electrons available per atom, reducing *e/a* from 4.229 to 4.188.

Table 4.1 – Important design parameters of the novel ternary compositions

Alloy	Bo	Md (eV)	*e/a*	Nb/Fe (at.)	[Mo] eq.
Ti-31Nb-1.0Fe	2.847	2.428	4.229	18.63	11.18
Ti-27Nb-1.5Fe	2.838	2.421	4.220	10.82	11.31
Ti-23Nb-2.0Fe	2.829	2.415	4.211	6.91	11.44
Ti-19Nb-2.5Fe	2.820	2.409	4.203	4.57	11.57
Ti-15Nb-3.0Fe	2.812	2.404	4.195	3.01	11.70
Ti-11Nb-3.5Fe	2.804	2.399	4.188	1.88	11.83

4.3. Water-quenched samples

Figure 4.3 depicts the XRD patterns of the water-quenched samples. The patterns were obtained with the beam diffracting on the rolling plane surface. As can be seen, characteristic β peaks are clearly the most intense in all the compositions. At higher Nb/Fe atomic ratios (3110, 2715, 2320), a preferred {211}β orientation (2θ=69.48) is visible parallel to the rolling plane. The Fe-rich samples show a conventional {110}β texture. In the alloys with higher Nb/Fe atomic ratio, athermal ω phase is detected by XRD, represented by the diffraction peaks at 2θ = 31.5° and 66.2°. However, the presence of ω phase in Fe-rich alloys detected by XRD was doubtful. Therefore, to confirm its presence, ST-WQ samples were analyzed by TEM, and the results are illustrated in Fig. 4.4.

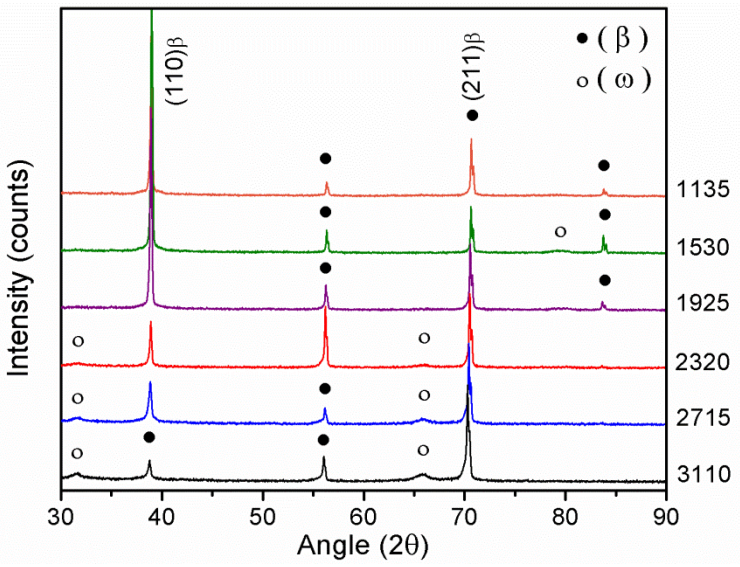

Figure 4.3 – X-ray diffraction patterns of water-quenched (WQ) alloys.

Like in previous reports [69], the ath-ω phase was in fact present in all the experimental compositions, suggesting that Fe shifts the β / β+ω phase boundary line of the Bo−Md diagram to lower Md values – i.e., to the left – expanding the ω stabilization field. According to Chaves et al. (2015), Ti-15Nb-3Fe alloys that had undergone rapid cooling via suction casting also presented ath-ω [109]. Although the electron diffraction spots become sharper with smaller Nb/Fe atomic ratios, a clear relationship between the ath-ω phase size or volumetric fraction and the Fe content cannot be established at this time based on the results (Figures 4.3 and 4.4).

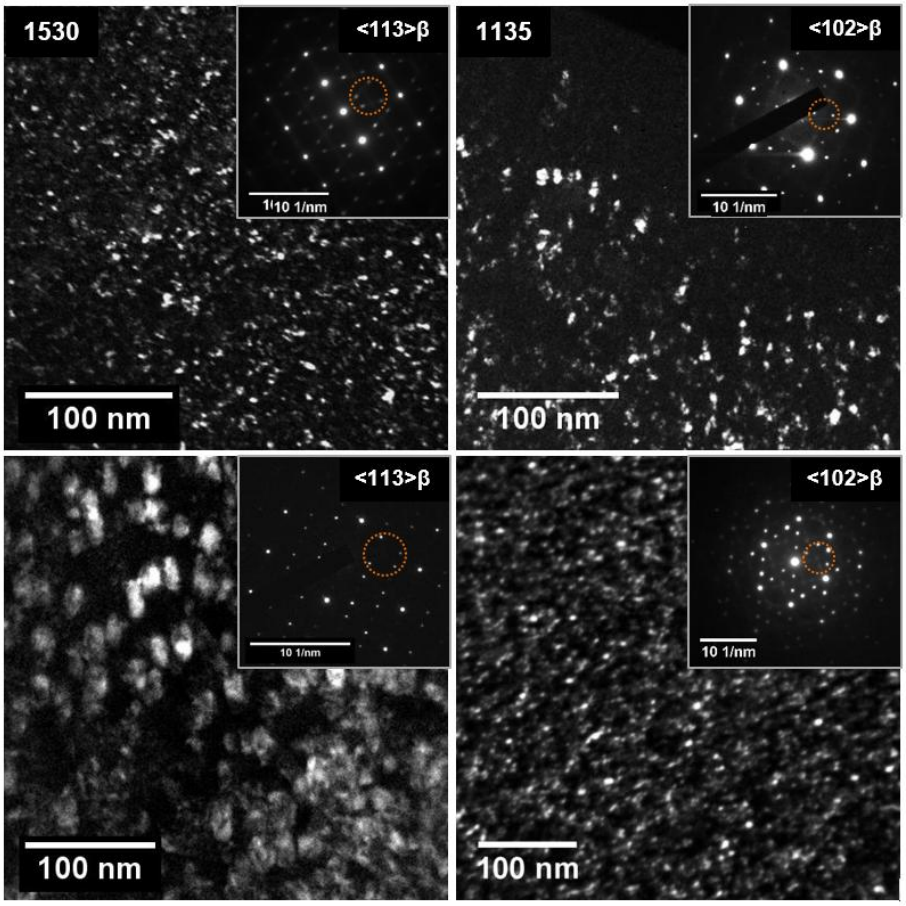

Figure 4.4 – TEM dark-field images of some water-quenched (WQ) experimental alloys. The ath-ω spots (1/3 and 2/3 positions) were selected to compose the DF image. The pictures on the left were recorded through the <113> β zone axis, and those on the right through the <102> β zone axis.

As for mechanical properties, hardness appears to vary greatly as a function of the substitution of Nb with Fe. Given that all the microstructures are composed of β+ath-ω, as depicted in Figure 4.4, it can be stated that Fe strongly reinforces the β phase matrix due to a solid solution effect. The solid solution effect of Fe is more marked than that of Nb because Fe has a higher number of valence electrons (Fe=8 vs. Nb=5) and a smaller atomic size. Accordingly, based on the compression stress-strain curves presented in Fig. 4.5, the presence of Fe also increases the yield stress of the alloys from 496 MPa (3110) to 715 MPa (1135) and causes a reduction in ductility, illustrated in Figures 4.5b–d. Ehtemam-Haghighi et al. (2016) reported slightly higher mechanical strength (932 MPa) for 1135 as cast alloy, possibly resulting from rapid cooling. The ST-WQ 1135 and 1530 alloys showed almost 30% of plastic strain, presenting a classical 45° fracture (maximum shear stress) due to their brittle Fe-rich matrix. Ti-1925 and 2320 presented small cracks that rendered the stress-strain curves unstable after 30–35% of plastic strain. Ti-2715 and 3110 did not fracture at all, extending to 70% of total deformation. Accordingly, 45º fractures that are typical of brittle materials are observed in 1135 alloy (Fig. 4.5b), due to its brittle Fe-rich β matrix [111]. By the end of the compression tests, the parts had become fixed together due to friction; therefore, it was impossible to record good images of the fracture surfaces.

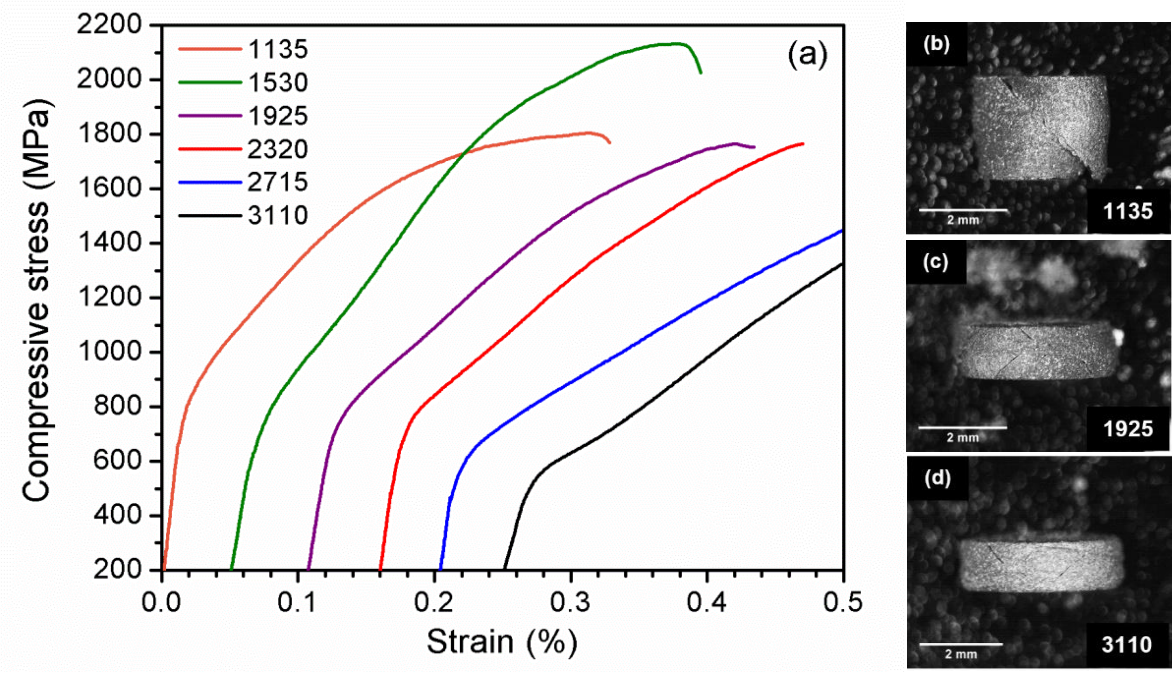

Figure 4.5 – (a) Compression, engineering stress-strain curves of all the water-quenched (WQ) experimental alloys. Yield strength is also presented in Table 3. Profiles of the fracture surfaces of: (b) 1135, (c) 1925, and (d) 3110 alloys, respectively.

Concerning the elastic modulus, all the alloys presented E=95 ± 4 GPa except for Ti-31Nb-1Fe, which presented a somewhat lower elastic modulus of about 80 GPa. Elastic modulus measurements were confirmed with an ultrasonic pulse-echo apparatus. Fig. 4.6 shows a compilation of the results summarized in Table 4.2.

Table 4.2 – Summary of the mechanical properties for WQ alloys

Alloy	HV_1	Elastic mod. (GPa)*	Yield Strength (MPa)
Ti-31Nb-1.0Fe	230 ± 11	81 ± 3	477 ± 79
Ti-27Nb-1.5Fe	277 ± 16	94 ± 2	496 ± 31
Ti-23Nb-2.0Fe	314 ± 6	95 ± 5	604 ± 55
Ti-19Nb-2.5Fe	334 ± 4	90 ± 3	672 ± 77
Ti-15Nb-3.0Fe	362 ± 3	94 ± 3	695 ± 40
Ti-11Nb-3.5Fe	382 ± 3	97 ± 1	715 ± 44

**via pulse-echo ultrasonic testing;*

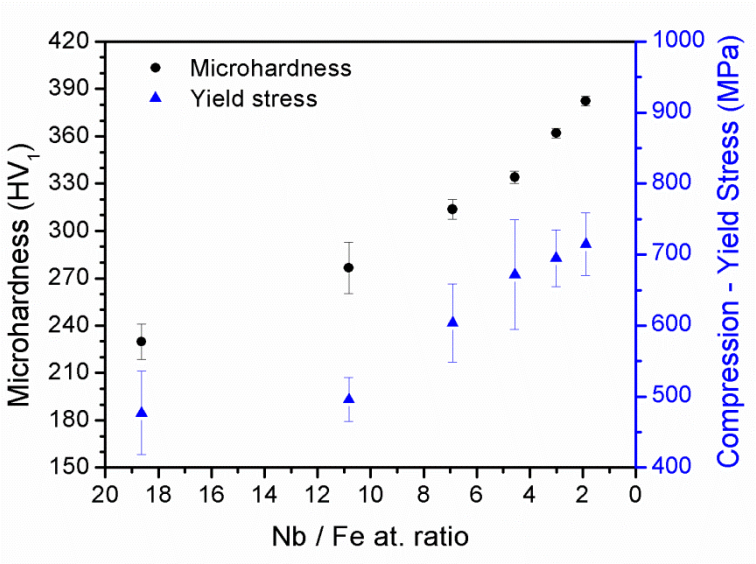

Figure 4.6 – Variations in Vickers hardness and compressive yield strength as a function of the Nb/Fe atomic ratio of all the water quenched (WQ) experimental alloys.

4.4. Furnace-cooled samples

In the furnace cooling process, the β phase slowly decomposes into the α phase. Initially, the temperature drops at a faster cooling rate, which diminishes as lower temperatures are reached. The kinetics of α phase precipitation during continuous cooling can

be estimated by examining the final microstructure at room temperature (RT). A higher α-phase volumetric fraction is related to intense α nucleation and growth at lower temperatures (at which the sample spends more time). Upon analyzing the SEM backscattered electron (BSE) images shown in Figure 4.7, one can see the contrasted β + α phase microstructures among the FC experimental alloys. While 2715 shows a microstructure composed of just a few allotriomorphic α precipitates and iso-ω phase detected by XRD (Figure 4.8), 2320 and 1925 show finely dispersed α phase laths and no ω phase. These laths appear to thicken as the Nb/Fe ratio decreases (reducing Nb, increasing Fe). EDS measurements of the thick α phase laths contained in 1530 and 1135 indicated that the β phase next to the laths is enriched in Nb and Fe, reaching 21 ± 1 Nb, 8 ± 1 Fe and 18 ± 1 Nb, 7 ± 1 Fe (wt.%), respectively.

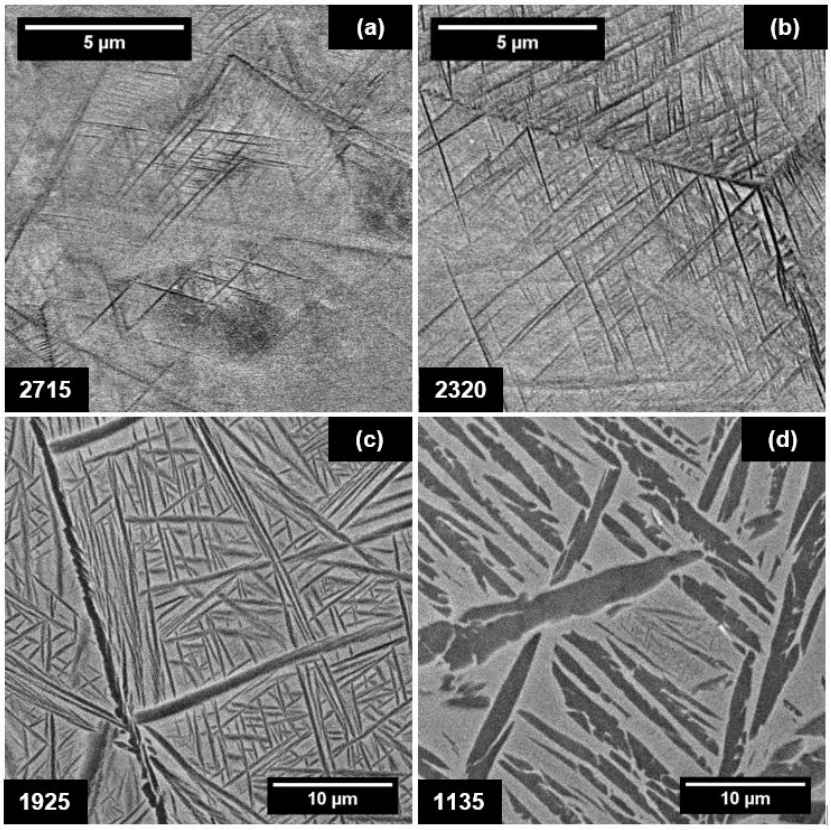

Figure 4.7 – SEM-BSE micrographs of furnace cooled (FC) experimental alloys: (a) 2715, (b) 2320, (c) 1925, and (d) 1135.

As expected, the presence of ω_{iso} in the 3110 and 2715 alloys increased the Vickers hardness and elastic modulus. Figure 4.9 illustrates the elastic modulus curves. The limited formation of the α phase during FC in 3110 and 2715 is attributed to the competition between α and ω formation in Nb-rich alloys [32]. The 1925 alloy presented the lowest elastic modulus

(83 ± 4 GPa) among the FC samples because of a combination of fine α phase laths and the complete absence of ω phase. It seems that α phase precipitation leads to marked solute rejection to the β phase, making the formation of ω phase unlikely [32]. The elastic modulus increased in 3.0 and 3.5 Fe (wt.%) rich alloys due to a higher volumetric fraction of α phase. Since α phase strongly rejects Fe, it seems that the higher the Fe content substituting Nb, the easier it is to grow α phase precipitates by solute rejection, which may be a consequence of the markedly high diffusion of Fe in Ti alloys [116].

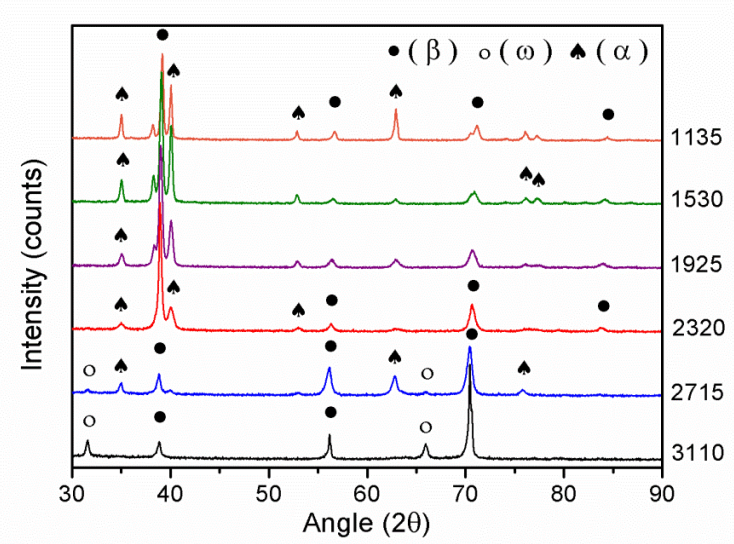

Figure 4.8 – X-ray diffraction patterns of furnace-cooled (FC) experimental alloys.

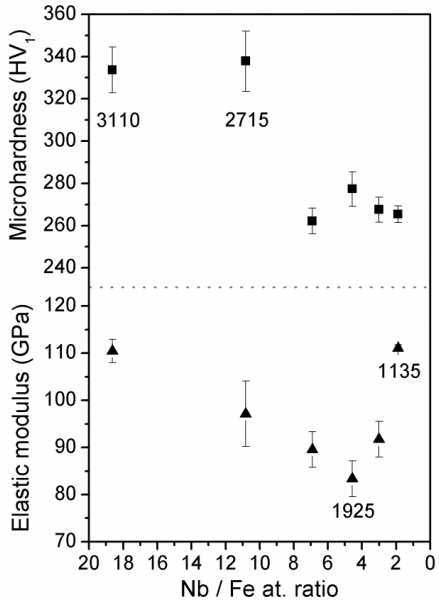

Figure 4.9 – Vickers hardness and elastic modulus of the furnace cooled (FC) experimental alloys as a function of the Nb/Fe atomic ratio.

4.5. Lattice structure differences between WQ and FC samples

By Rietveld refinement of the XRD diffraction patterns of the WQ (Figure 4.3) and FC (Figure 4.8) samples, the β phase lattice parameter was evaluated in both conditions, and the results are displayed in Table 4.3. In FC samples, the enriched β phase lattice parameter varies by approximately 0.0025 nm. This significant change in the lattice parameter due to alloying (Figure 4.10) may be one of the key points to understand the thermal stability of ω and α phases in these alloys. The smaller the β phase cell, the shorter the lattice displacement required along {222}β to form ω.

Table 4.3 – Lattice parameters obtained via the XRD patterns; uncertainty in parentheses

Composition	Condition	Phase	Lattice parameter (nm)
3110	WQ	β	0.3279(1)
	FC	β	0.3274(2)
2715	WQ	β	0.3274(0)
	FC	β	0.3273(1)
2320	WQ	β	0.3270(6)
	FC	β	0.3267(0)
1925	WQ	β	0.3269(8)
	FC	β	0.3263(1)
1530	WQ	β	0.3265(6)
	FC	β	0.3257(5)
1135	WQ	β	0.3265(4)
	FC	β	0.3249(8)

However, based on HRTEM images of 1530-WQ in Figure 4.11, ath-ω formed in WQ samples is still the result of a full collapse of the β lattice, which was expected in this solute content range – i.e., [Mo]eq. close to 12. The full collapse can be stated based on the ratio between the interplanar distances [0002]ω / [222]β = 0.666, which gives rise to perfectly matched characteristic 1/3 and 2/3 spots that are visible in the Fast Fourier Transform (FTT) image. Figure 4.11c was obtained by applying a filter to select only the 1/3 and 2/3 spots.

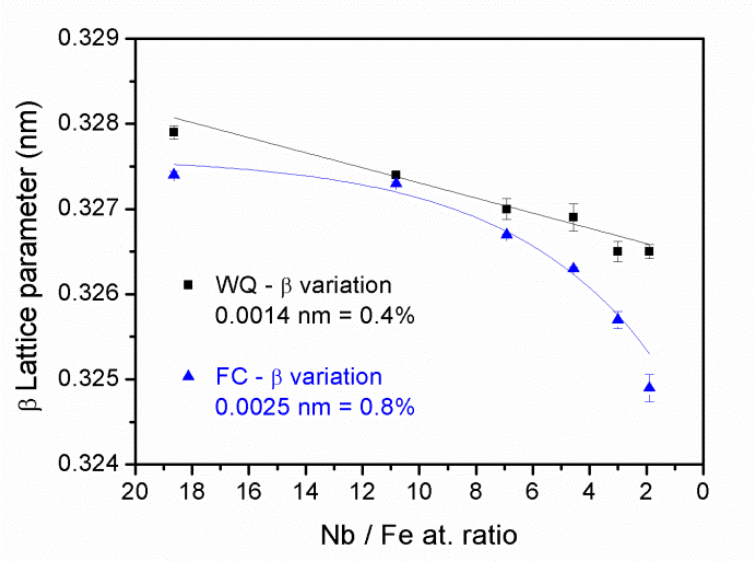

Figure 4.10 – Variations in the lattice parameter of the β phase in water quenched (WQ) and furnace cooled (FC) experimental alloys, calculated from the refined XRD patterns.

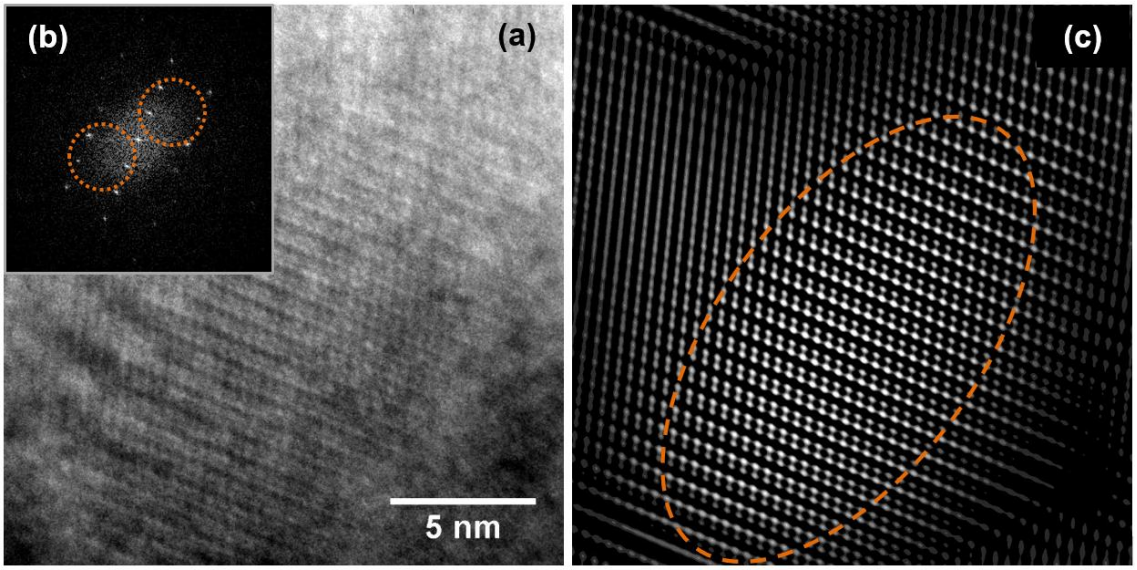

Figure 4.11 – (a) HRTEM images from water-quenched 1530 alloy through <113>β zone axis, (b) FFT showing pass band filters in orange, (b) Image obtained with (FFT) filtering showing (the core) of the full collapse of β to form ωath phase.

4.6. Step-quenching to 350ºC and thermal stability

DSC measurements were performed to obtain the transition temperatures of some phase transformations during heating from the initial condition (WQ). Nevertheless, it is worth noting that the enthalpy of formation and dissolution of ω and α phases are quite low,

making it difficult to identify the phase transformation events [113] properly. According to recent reports in the literature, a gradual conversion of iso-ω into β phase – i.e., what we call here ω-*solvus* – starts near 670K (~397ºC) in Ti-29Nb. Therefore, a step-quenching heat treatment (after solution treatment) to 350ºC was performed to ensure massive isothermal ω (ω_{iso}) phase formation in all the compositions. TEM investigations were performed to further clarify the resulting microstructure of 1135 after one hour of heat treatment. Figure 4.12 shows very large overlapping precipitates, confirming iso-ω phase formation. Their size is clearly much larger than that of the ath-ω particles depicted in Figure 4.3 (ST-WQ samples). Iso-ω precipitates will be further analyzed in the next Chapter.

Further evidence of this massive iso-ω formation is that the hardness (400 to 460 HV_1) and elastic modulus (110 to 130 GPa) of 1135 are the highest among all the compositions studied. In conclusion, a microstructure similar to that of the WQ alloys (also β+ω, albeit iso-ω), but with a higher volumetric fraction of ω phase was obtained. The aim was to obtain a microstructure that could be unequivocally identified by DSC.

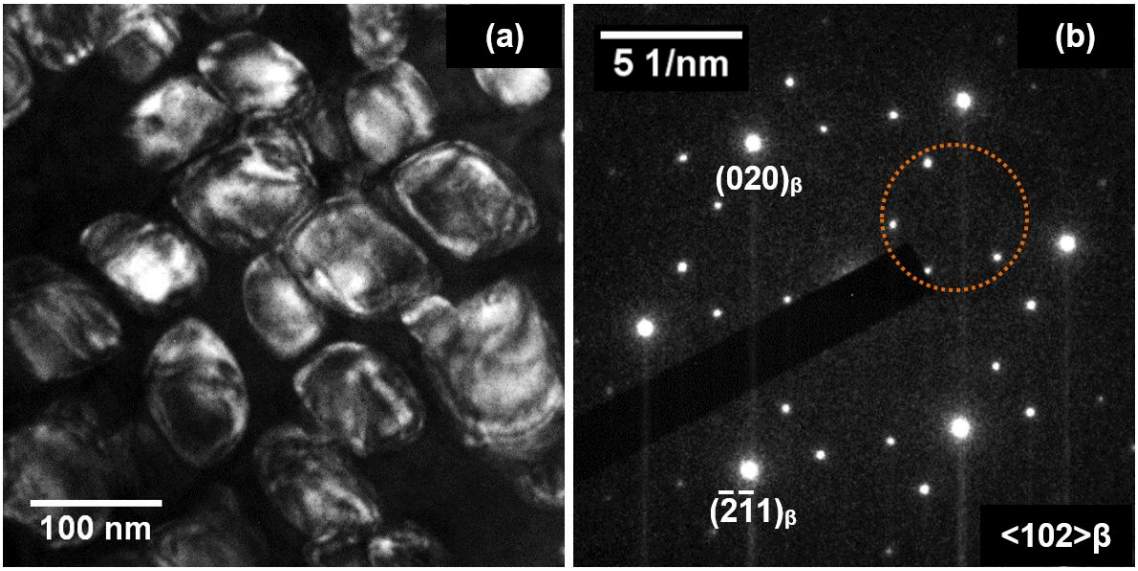

Figure 4.12 – a) Dark-field TEM images of 1135 quenched from 623K (350ºC) after 1 h of heat treatment. b) The corresponding selected area electron diffraction pattern obtained with the ωiso spots (1/3 and 2/3 positions) parallel to the <102>β zone axis.

Figure 4.13 presents a compilation of the DSC scans. A good signal-to-noise ratio was achieved, enabling the identification of the thermal transitions in all the experimental alloys. The phase transformations were analyzed and attributed to each peak, based on recent papers by Barriobero et al. [117,118]. In the heating step, the ω-phase decomposes into β phase,

originating the first endothermic peak. In the Fe-rich alloys 1135 and 1530, this process requires less energy and begins at lower temperatures.

On the other hand, the next peak, associated with α phase precipitation within the β matrix (exothermic), occurred abruptly only in 1135 and 1530 alloys – probably due to intense solute rejection resulting from the higher Fe content. At 800ºC, all the samples were above β-*transus* temperature, ensuring the full reverse transformation of the α-phase to β (not detected). Upon cooling, the same intense β → α transformation was observed in 1135 and 1530 alloys, possibly because these alloys undergo faster α-precipitation, considering that α phase forms easily in solute lean regions during cooling. Lastly, β → ω transformation can be detected, indicating that ω phase forms (and dissolves) easily in Fe-rich alloys. Given that ω phase forms at higher temperatures in 1530 and 1135 alloys, less energy is needed, which could be linked with the smaller β lattice parameter. The onset temperatures of the ω → β (heating) and β → ω (cooling) transformations were estimated from the intersection of the tangent line through the peak slope with the baseline, which are presented in Table 4.4. Based on ω decomposition, it appears that aging at temperatures over 450ºC is a satisfactory strategy to develop controlled α precipitation in alloys with lower Nb/Fe atomic ratios. At higher Nb/Fe atomic ratios, ω is formed within a much wider temperature range.

Table 4.4 – Transformation temperatures related to ω phase stability

Composition	**Transformation**	**Onset temperature (ºC)**
3110	ω → β	446
	β → ω	301
2715	ω → β	411
	β → ω	317
2320	ω → β	419
	β → ω	340
1925	ω → β	418
	β → ω	357
1530	ω → β	413
	β → ω	379
1135	ω → β	408
	β → ω	377

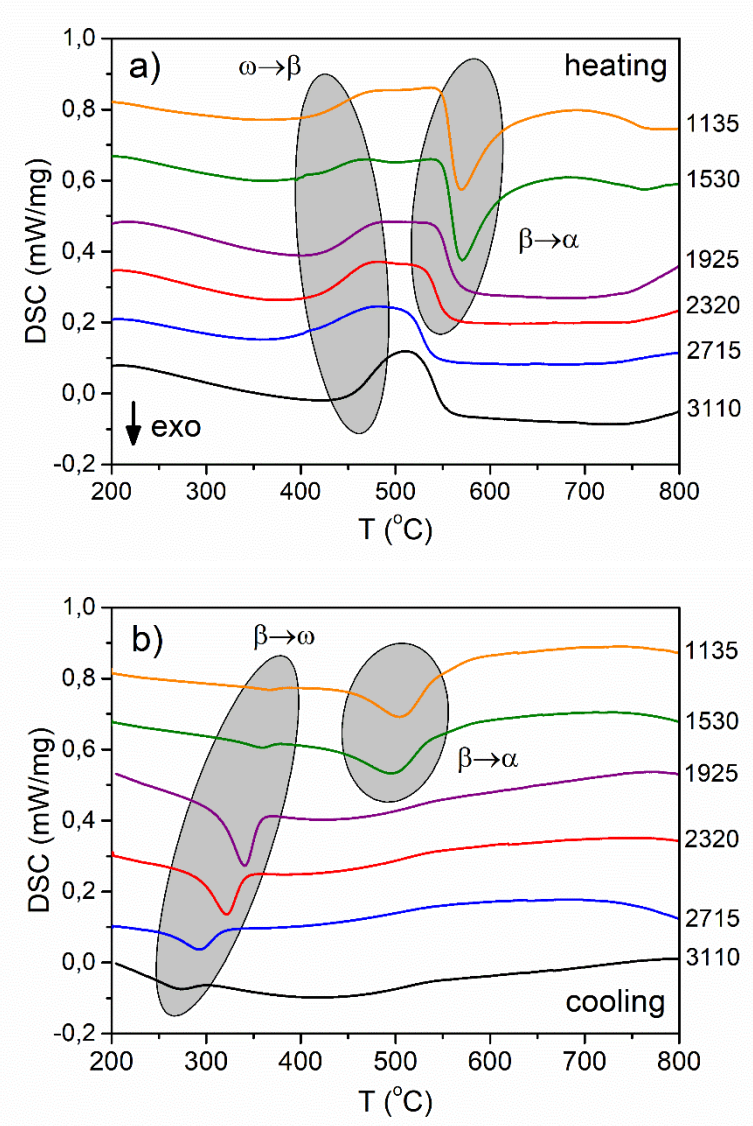

Figure 4.13 – DSC scans of experimental alloys step-quenched to 623K (350 ºC) for 24 h of heat treatment: (a) first heating and (b) first cooling cycles.

4.7. Final remarks

Much attention has focused on the Ti-Nb-Fe system in recent years, but some of its aspects remain unclear. This study sought to shed light on some aspects such as:

- Contrary to the $\overline{Bo} - \overline{Md}$ diagram, athermal ω phase was detected in all the alloys after water-quenching from the β phase field, suggesting that this phase originates from a fully collapsed β phase, based on HRTEM observations.
- According to the diagram, the elastic modulus obtained for the WQ alloys increased in response to increasing Fe content. The higher the Fe content that substituted Nb, the

higher the elastic modulus of the WQ alloys, whose mechanical strength also increased. In the alloys with Fe content higher than 1.0 wt.%, the elastic modulus exceeded 80GPa.

- As for the FC samples, the reduction in the Nb/Fe ratio was beneficial to α phase precipitation rather than to isothermal ω phase formation. It also drastically changed some aspects of α phase precipitation, such as morphology and the volumetric fraction.
- The addition of Fe reduces the β phase lattice parameter owing to its relatively low atomic size.
- Although all the designed compositions showed a similar Mo[eq.] number, the α phase volumetric fraction was higher in Ti-1530 and Ti-1135, which are Fe-rich alloys.
- DSC measurements indicated that better aging heat treatment routes could be designed for these alloys. Despite their dissimilar thermal stability, a temperature of 450 ºC is suggested, which is above ω-*solvus* for all these alloys.

Finally, Ti-19Nb-2.5Fe exhibited promising features for low-cost implants. This alloy presented the lowest elastic modulus after FC due to the suppression of ω phase formation and fine α phase precipitates – which did not significantly increase the elastic modulus. Furthermore, considering that ω phase can be formed only within a narrow range of temperatures in this composition, the addition of ω suppressor elements such as Zr and Sn may be a potential strategy to obtain low-modulus quaternary alloys, preserving the suggested Nb/Fe ratio.

5. ISOTHERMAL OMEGA-PHASE IN TERNARY ALLOYS

In this section, the formation of isothermal omega-phase in three Ti-Nb-Fe alloys with different concentrations of Nb and Fe from the last chapter was explored by scanning transmission electron microscopy, X-ray energy dispersive spectroscopy and X-ray diffraction. After being aged at 350°C for 24 h, semi-cuboidal omega precipitates with flat faces closely parallel to the [001]β-phase were characterized in the Ti-11Nb-3.5Fe (wt.%) alloy, while in the Ti-19Nb-2.5Fe and Ti-27Nb-1.5Fe the precipitates remained ellipsoidal. A high concentration of Fe in the β matrix was found to enhance the lattice misfit between

matrix and precipitates. Lattice strains higher than 0.1% along the [111]β-phase induced omega to a semi-cuboidal morphology.

5.1. Background

The formation of isothermal omega (iso-ω) phase in Ti alloys has been investigated for many years. The first papers on the subject date from the late '60s. While Williams and Blackburn explored the Ti-Mo and Ti-V systems [119], Hickman went through five binary systems: Ti-Cr, Ti-Mn, Ti-Fe, Ti-Nb and Ti-Mo [33]. At the time, the authors identified a massive ω formation during heat treatments performed at 350 and 400 °C, and by comparing the morphology of the particles among these many systems, it was established that the omega morphology was outlined by the lattice misfit between the β matrix and the ω particles. Omega precipitates tend to acquire a cuboidal morphology, with faces parallel to the [001]β direction, in systems which the linear misfit[7] is larger than 0.5%, e.g., in Ti-Cr, Ti-Fe and Ti-V alloys [33]. On the other hand, the ellipsoidal morphology prevails in systems where the elastic-strain energy is low (Ti-Nb, Ti-Mo). This hypothesis was later analyzed and confirmed in multicomponent alloys such as Ti-10V-2Al-3Fe [28], and Ti-20V (wt .%), by tracking the composition and morphology of the particles over time [36].

For decades, many works described the ω_{iso} particles' morphology by being binary. They were defined as either ellipsoidal or cuboidal. However, more recently, Ng et al. (2011) showed that for ternary systems such as Ti-10V-6Cu [120], iso-ω morphology changed depending on the heat-treatment that the samples were subjected (see Figure 5.2). Based on their observations, we inferred that given a system containing both high and low-misfit alloying elements, several ω transient states with morphology between ellipsoidal and cuboidal could be formed, depending on the local composition.

[7] The "linear" misfit was defined as the average misfit $L = \frac{1}{3}\left(\frac{V_\omega - V_\beta}{V_\beta}\right)$

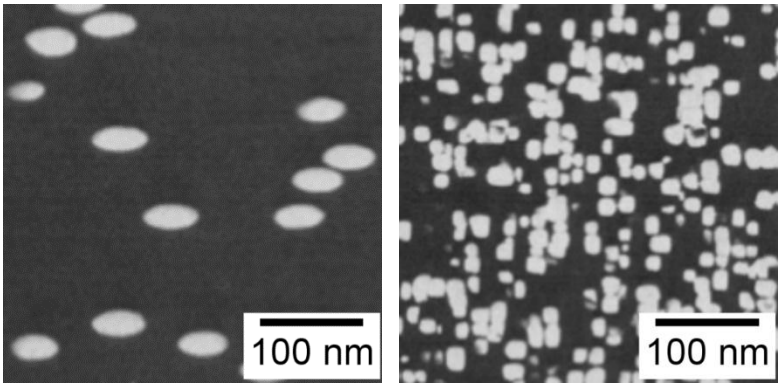

Figure 5.1– Ellipsoidal ω-phase in a Ti-Mo based alloy aged at 480 °C for 5 min (left) and Cuboidal ω-phase in Ti-8Fe (wt.%) aged at 400 °C for 4 h. Adapted from Hickman (1969) [33].

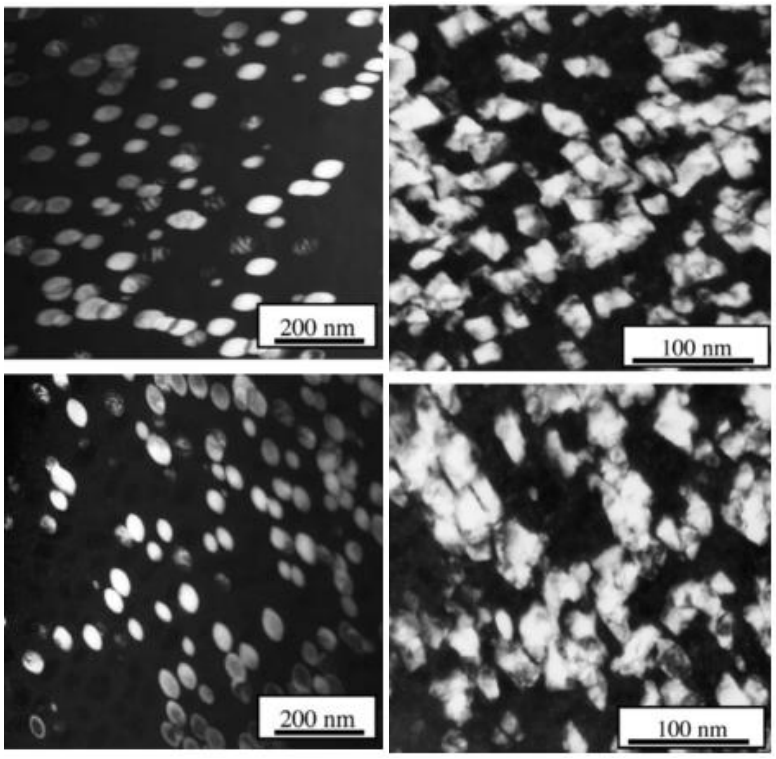

Figure 5.2 – Ellipsoidal ω-phase in a Ti-10V-6Cu aged at 500 °C for 10 min (left) and Cuboidal ω-phase in the same alloy after solution-treatment followed by air-cooling. Both images were adapted from Ng et al. (2011) [120].

5.2. Experimental setup

The present chapter aimed to explore the iso-ω phase formation in three alloys with different contents of Nb (high misfit) and Fe (low misfit). The compositions employed here were the Ti-27Nb-1.5Fe, Ti-19Nb-2.5Fe and Ti-11Nb-3.5Fe (wt.%). Given that Nb is a low-misfit alloying element and Fe is the opposite, substituting Nb with Fe should induce the alloys to more likely form cuboidal ω particles. With this setup, we systematically analyzed the influence of the misfit and the composition on ω-phase morphology.

For characterization purposes, the solute redistribution between the β phase matrix and the ω precipitates was assessed by scanning transmission electron microscopy, X-ray energy dispersive spectroscopy (STEM-XEDS) on an Image-Corrected Titan3^{TM} G2 equipped with four EDS detectors (FEI's ChemiSTEM technology), at the Ohio State University. Further details about the design and production of the Ti-Nb-Fe alloys are presented in Chapters 3. For this experiment, samples were solubilized at 750°C per 10 min and step-quenched to 350°C for 24h, then water-quenched. According to Hickman et al. (1968) experiments with Ti—6Fe (wt.%), the volumetric fraction of omega phase evolves quickly from 0.25 (1h) to 0.78 after 24h of aging at 350°C, reaching a pseudo-stability [33].

5.3. Morphology and composition

Dark-field images of the iso-ω particles through the [110]β zone axis are shown in Figure 5.3. Figure 5.3a shows that most precipitates in Ti-11Nb-3.5Fe present flat edges nearly parallel to the (002)β planes and round edges pointing to [112]β directions, which give them a semi-cuboidal shape. In contrast to the completely cuboidal precipitates previously described in the Ti-Fe and Ti-V systems, the smooth edges might be linked with the Nb presence in this alloy. The iso-ω particles observed in Ti-11Nb-3.5Fe have, on average, 130 x 80 nm, and outsize most precipitates previously reported in binary systems such as Ti-Nb [94], Ti-Mo [101] and Ti-V [36], which never exceed 100 nm. Furthermore, their orientation with the matrix is following previous micro-elasticity assessments by Choudhuri et al. [36] and Bin Tang et al. [121]. On the other hand, in Ti-19Nb-2.5Fe (Figure 1b) and Ti-27Nb-

1.5Fe (Figure 1c), the ellipsoidal ω precipitates display size and morphology much similar to the ones observed in the Ti-Nb binary system [32,39].

It is worth reminding that neither α nor α" phases were identified among the samples. The absence of α-phase may be related to the limited aging time [122], and the formation of α" is restricted due to the presence of Fe, which is reported to reduce martensite start (Ms) and finish (Mf) temperatures [123]. In the case of Ti-11Nb-3.5Fe, additional images at others low-index zone-axes were recorded and are presented in Figure 5.4.

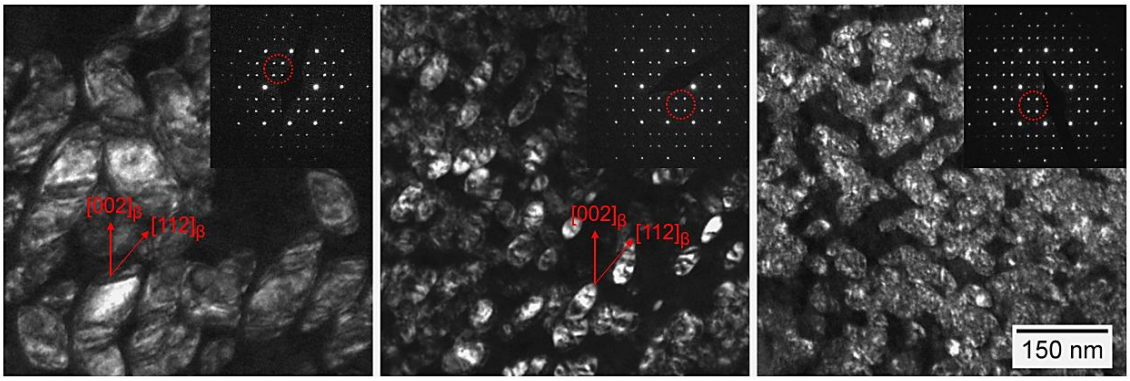

Figure 5.3 – Dark-field images of Ti-11Nb-3.5Fe (a), Ti-19Nb-2.5Fe (b) and Ti-27Nb-1.5Fe (c) from the ω-phase spots indicated in the diffraction insets for each experimental alloy. The diffraction patterns (insets) and the dark-field images were rotated (preserving the rotational-calibration) to match the same $\vec{g} = [112]_{\beta}$ vector orientation. All samples are oriented to <110>β zone axis. Images at the same magnification.

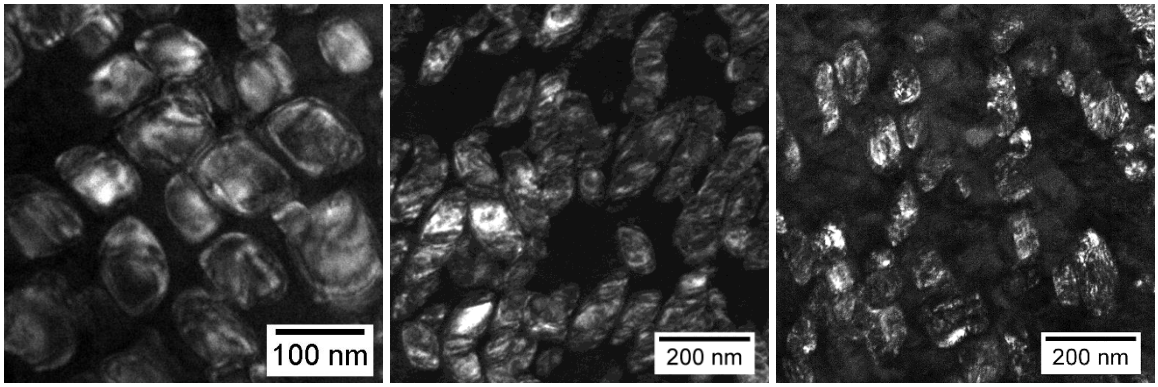

Figure 5.4 – The semi-cuboidal omega seen from several low-index zone axes: (from left to right): <102>, <110> and <113>β. Images are not at the same magnification (check the scale bar).

The STEM-XEDS data (Figure 5.5) points to a forceful rejection of Fe from ω phase among all the experimental alloys. Thereupon, the β matrix surrounding the omega particles in Ti-11Nb-3.5Fe can reach 10 wt.% of Fe, which is certainly linked to the semi-cuboidal morphology observed in this composition only. Otherwise, there's still a significant Nb amount ranging from 12 to 7 wt.% remaining into the precipitates, depending on the alloy, as can be seen in Table 5.1.

Table 5.1 – Summary of the STEM-XEDS data showing the composition of the β matrix and the iso-ω precipitates for the experimental alloys reported in wt. %.

Composition (wt.%)	**β matrix**		**ω precipitates**	
	Nb	Fe	Nb	Fe
11Nb-3.5Fe	14.3 ± 0.7	5.0 ± 0.9	6.7 ± 0.8	0.8 ± 0.3
19Nb-2.5Fe	21.6 ± 1.2	3.9 ± 0.7	8.2 ± 1.2	1.7 ± 0.6
27Nb-1.5Fe	30.1 ± 1.4	2.8 ± 0.5	11.7 ± 1.6	1.8 ± 0.6

Similar behavior has been reported among Ti-Mo based alloys, in which a residual Mo content is present within the precipitates, even after long aging heat treatments [30,31]. A particularity of this system, however, is the presence of Nb and Fe altogether. The enthalpy of mixing (ΔH_{mix}) between these two elements is drastically lower (-22.2 J/mol) [124], which points to an aggregation of Nb and Fe in the β-phase. More details about miscibility models involving the enthalpy of mixing will be presented in Chapter 6. To simplify, it is possible that Fe forces Nb out of the precipitates, via solute dragging, resulting in an extensive Nb diffusion to the β matrix at relatively low temperatures (350 °C).

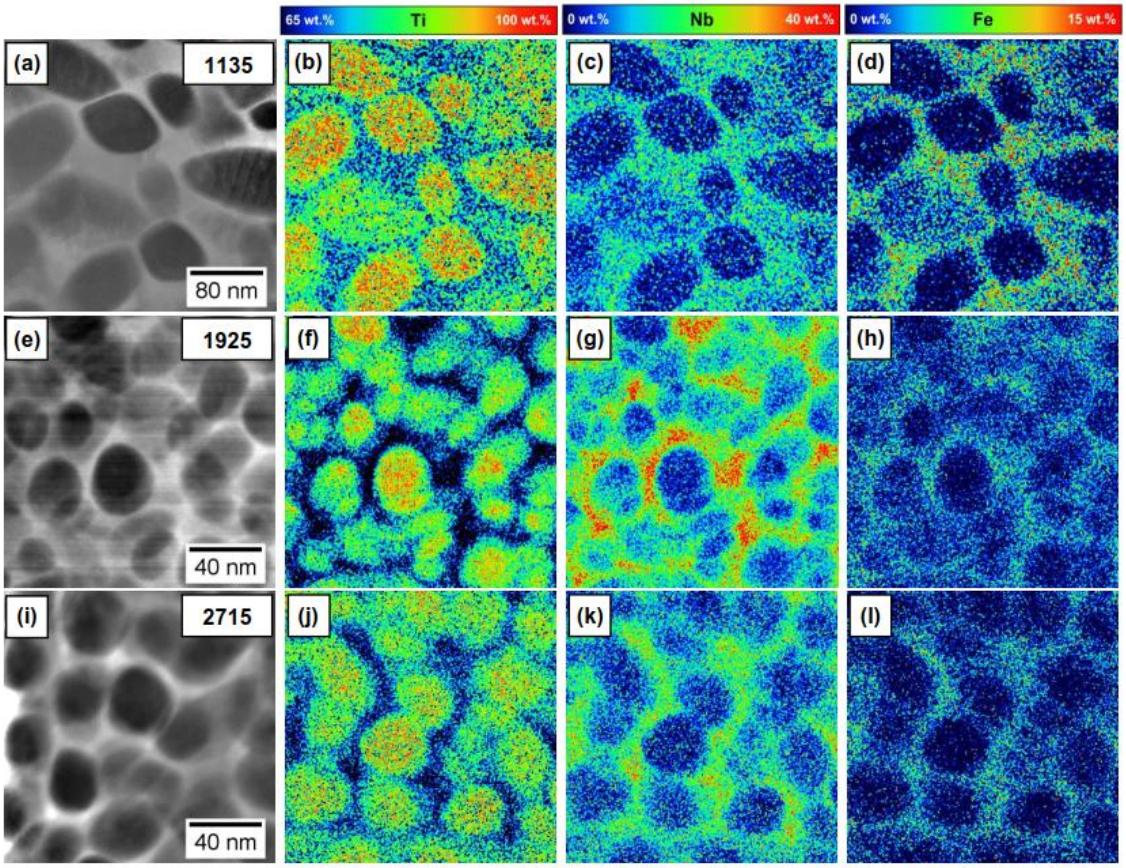

Figure 5.5 – HAADF (a, e, i) and STEM-XEDS compositional maps for Ti-11Nb-3.5Fe (a), Ti-19Nb-2.5Fe (e) and Ti-27Nb-1.5Fe (i), respectively. Images were composed of the same color-grade scale for each element.

5.4. Crystal structures and misfit

The crystal structure is also an important parameter in understanding how the ω-precipitates in Ti-11Nb-3.5Fe diverge from the others. Figure 5.6 shows the XRD data of the three samples. The sharp diffraction peaks associated with the ω-phase shift from left to right, the higher the Fe content. By refining the XRD data presented in Figure 5.6, it can be seen a gradual decrease of the β lattice parameter from Ti-27Nb-1.5Fe (0.3270 nm) to Ti-11Nb-3.5Fe (0.3255 nm). That behavior was expected since the β-phase lattice parameter is reduced with the enrichment in Fe [125]. We reported analogous behavior among ST-FC samples in Chapter 4 [122]. While Ti-27Nb-1.5Fe presented strong (001)ω reflections, the Fe-rich alloys presented strong (201)ω reflections instead.

Furthermore, a lattice decrease of the ω-phase hcp crystal structure can also be supported by Fe. Despite all the lattice constants (a,b and c) being decreased (with the increase of the Fe content), the c/a ratio is not the same for all compositions, changing from 61.17% (2715) to 61.25% (1135). This change might be an indication of higher elastic anisotropy in Ti-11Nb-3.5Fe alloy [35], comparing to the other two selected alloys in this study.

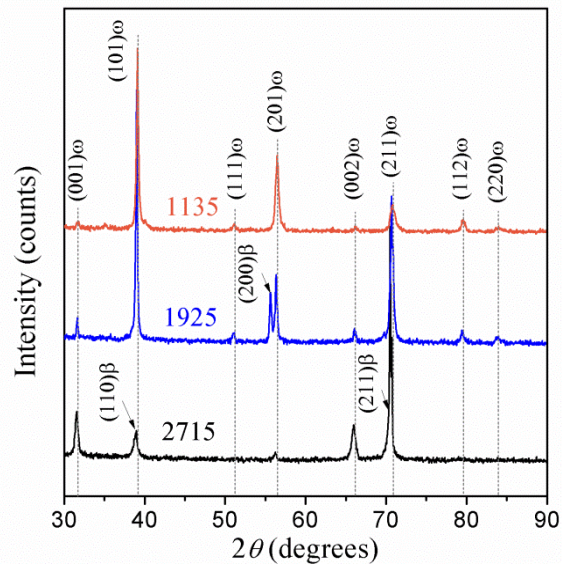

Figure 5.6 – X-ray diffraction patterns of the heat-treated alloys and the ideal reflections of ω phase. Extra reflections are associated with the β (bcc) matrix.

Using the lattice parameters obtained by XRD, we estimated the lattice strain between the β and ω phases applying the stress-free transformation strain (SFTS) matrix provided by Choudhuri et al. (2017). Based on the lattice correspondence between β and ω phases, the transformation strain along each orthogonal axis is calculated by Equation 2. It is assumed that the [111]β // [0001]ω direction corresponds to the z-axis (ε_3) - further details are presented in reference [36]. A compilation with the lattice parameters and the calculated transformation strains along the z-axis is presented in Table 5.2. As a reference, we estimated that ε_3 = -0.0361% for an ideal ellipsoidal ω particle (in Ti-30Nb wt.%) at the same heat treatment condition. On the other hand, the strain along the z-axis for Ti-11Nb-3.5Fe was estimated to be ε_3 = +0.1095%, one order of magnitude higher, in absolute numbers, than what was verified for Ti-19Nb-2.5Fe (ellipsoidal). Therefore, the correlation between

composition and ω-structure observed among the selected alloys indicate that the mechanism behind the iso-ω formation may be concurrently diffusive and displacive, as some in-depth studies suggest, since strains along the z-axis change with the composition [38,101]. From an atomistic perspective, it might be the case that Ti-Fe, Nb-Fe and Fe-Fe bonds are stiffer than Ti-Nb and Ti-Ti bonds, so the Fe enrichment in the adjacent β-matrix increases the misfit between matrix and precipitates, which drives the morphology of the precipitates to change accordingly. For this reason, a distortion of the nearest-neighbor bonds around Fe could be expected [126].

$$\varepsilon_{ij} = \begin{bmatrix} \frac{a_\omega - \sqrt{2}.a_\beta}{\sqrt{2}.a_\beta} & 0 & 0 \\ 0 & \frac{a_\omega - \sqrt{2}.a_\beta}{\sqrt{2}.a_\beta} & 0 \\ 0 & 0 & \frac{2c_\omega - \sqrt{3}.a_\beta}{\sqrt{3}.a_\beta} \end{bmatrix} = \begin{bmatrix} \varepsilon_1 & 0 & 0 \\ 0 & \varepsilon_2 & 0 \\ 0 & 0 & \varepsilon_3 \end{bmatrix} \quad (2)$$

Assuming a fully coherent transformation on the following directions

$$\varepsilon_{11}(x) \rightarrow [1\bar{1}0]_\beta \,||\, [2\overline{11}0]_\omega,$$

$$\varepsilon_{22}(y) \rightarrow [11\bar{2}]_\beta \,||\, [01\bar{1}0]_\omega,$$

$$\varepsilon_{33}(z) \rightarrow [111]_\beta \,||\, [0001]_\omega,$$

The experimental results presented in this chapter reveal that semi-cuboidal iso-ω precipitates were obtained among Ti-11Nb-3.5Fe samples only, while the regular ellipsoidal precipitates were detected among Ti-19Nb-2.5Fe and Ti-27Nb-1.5Fe (wt.%).

Table 5.2 – Phases lattice parameters and transformation strains for each alloy. As a reference, Ti-30Nb (wt.%) binary alloy was included for comparison.

Composition (wt.%)	**Lattice parameters (Å)**			**SFTS (%)**	
	a_β	a_ω	c_ω	$\varepsilon_1 = \varepsilon_2$	ε_3
11Nb-3.5Fe	3.255	4.607	2.822	+0.0812	+0.1095
19Nb-2.5Fe	3.263	4.617	2.826	+0.0524	+0.0056
27Nb-1.5Fe	3.270	4.628	2.831	0.0761	-0.0318
30Nb, ref [94]	3.285	4.634	2.834	-0.2210	-0.0361

5.5. The β-ω interface

Now that the morphology and crystal structure of the isothermal omega phases in this system are elucidated, we invested time in some high-resolution characterization of the particles using the double-corrected FEI Titan Cubed Themis, at the LNNano/CNPEM facilities. Ti-11Nb-3.5Fe was selected for this analysis, considering that the particles from this sample are the ones which need the higher STFS to be formed. As it can be seen in Figure 5.7c, the collapse from β to form ω is certainly full. The characteristic 1/3 and 2/3 spots associated with omega are clearly identified in Figure 5.7d (red circles). Furthermore, given the spherical aberration (Cs) correction capabilities of the employed microscope, compared to Figure 4.11, omega variants can be identified based on the spots obtained from each local FFT (Figure 5.7e and 5.7f). From the four possible omega variants, only two were detected. The misalignment between these variants is of 69º. As one can observe from the β-ω interface displayed in Figure 5.7f, it seems despite the high misfit between these β and ω phases, the interface seems to be fully coherent, since ω-phase is formed from a 1st order structural transition. Furthermore, a β phase film - which is rich relatively in Nb and Fe, according to Section 3.2 - between two divergent ω particles is necessary to guarantee this coherent interface.

5.6. Final remarks

In conclusion, an intermediate ω morphology between ellipsoidal and cuboidal has been obtained by partially substituting a low misfit alloying element (Nb) with a high misfit alloying element (Fe). The morphology of the iso-ω precipitates is related to the composition of the parent β-phase and, indeed, to the misfit between β-matrix and ω-precipitates. STEM-XEDS data point out to a sound rejection of Nb and Fe from the ω-precipitates to the adjacent β-matrix. Based on our XRD data and analyses, the semi-cuboidal morphology appears in systems which ε_3 is approx. 0.1%, an intermediate number among the well-known misfits for ellipsoidal (ε_3 approx. 0.01%) and cuboidal ω (ε_3 > 0.5%). Fe plays an important role in this scenario, being the element that drives the necessary lattice modifications in both β and β phases, even if present in low amounts. The use of an aberration-corrected microscope increases overall quality and resolution of the high-resolution images, providing better data for posterior analyses.

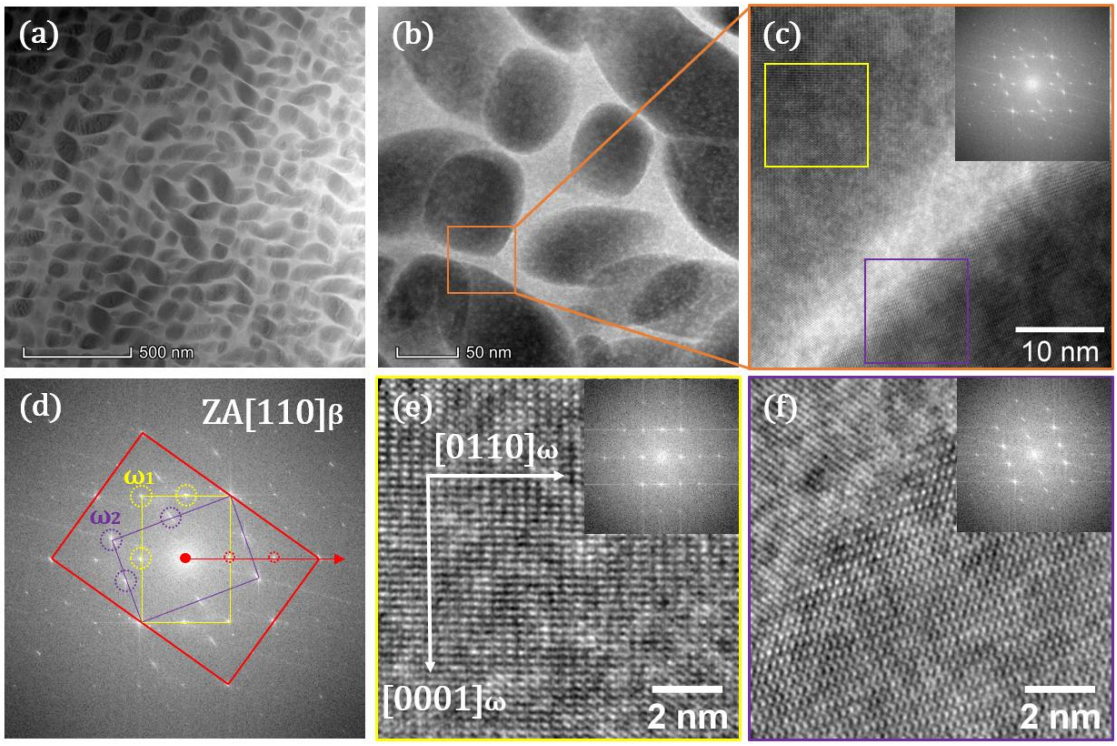

Figure 5.7 – (a, b) HAADF images of the isothermal omega formed in Ti-11Nb-3.5Fe, (c) high-resolution image of a interface of two omega particles with its respective FFT, (d) high-magnification of the FFT from image (c) magnified and with indications of the spots associated with beta (red), and two omega particles (yellow and purple), (e, f) detail of HR-image showing the atomic planes of each omega particle and its respective local FFT.

6. MECHANISMS OF ALPHA-PHASE PRECIPITATION

This chapter aimed to investigate the mechanisms of alpha (α) phase formation in Ti-Nb-Fe and Ti-Nb-Fe-Zr alloys from an in-depth analysis of the microstructure resultant of distinct aging heat-treatments. After a brief review from the literature, the discussion starts with the ternary Fe-rich alloys Ti-19Nb-2.5Fe, Ti-15Nb-3.0Fe and Ti-11Nb-3.5Fe (wt. %). The first section is focused on the activation of a homogeneous α-phase formation via pseudospinodal mechanism in Ti-11Nb-3.5Fe (wt.%) alloy, coupling thermodynamic data and experiments. The phenomenon had been verified twice the last years by subjecting commercial alloys such as Timetal-5553 and Timetal-21S to step-quenching heat treatments; however, it had never been observed in Ti-Nb based alloys. Afterward, the formation of

allotriomorphic (GB) α-phase will be discussed. Results from ternary and quaternary alloys subjected to a series of aging heat-treatments will be presented, detailed, and discussed. Finally, given the characteristics of the β-α interfaces, we used a classical ledge-wise model to estimate the difference between GB and bulk diffusion among Ti-11Nb-3.5Fe alloy' samples.

6.1. Heterogeneous alpha-phase precipitation

An essential step to ensure proper control of α phase precipitation during heat treatments is to investigate the mechanisms of α phase formation in binary and ternary systems. Two main mechanisms drive α-phase formation: (i) heterogeneous or (ii) homogenous nucleation. In the case of heterogeneous nucleation, grain boundaries, ω-phase, β' phase (a solute-enriched β-phase product of a spinodal decomposition) and crystalline defects might act as nucleation sites for the α-phase formation. One method of refining α-phase via heterogeneous nucleation is to promote the nucleation of finely dispersed iso-ω precipitates at the first stage of aging to then activate the ω-assisted α-phase mechanism at a second stage, at a higher temperature – also known as "double aging" [39]. On the other hand, the homogenous formation of α-phase can be obtained mediated by compositional fluctuations in the β-phase, leading to a congruent formation of the α-phase inside the grains, with composition far away from the equilibrium. This mechanism is known as pseudospinodal. More details on the topic can be found in [43,127–131].

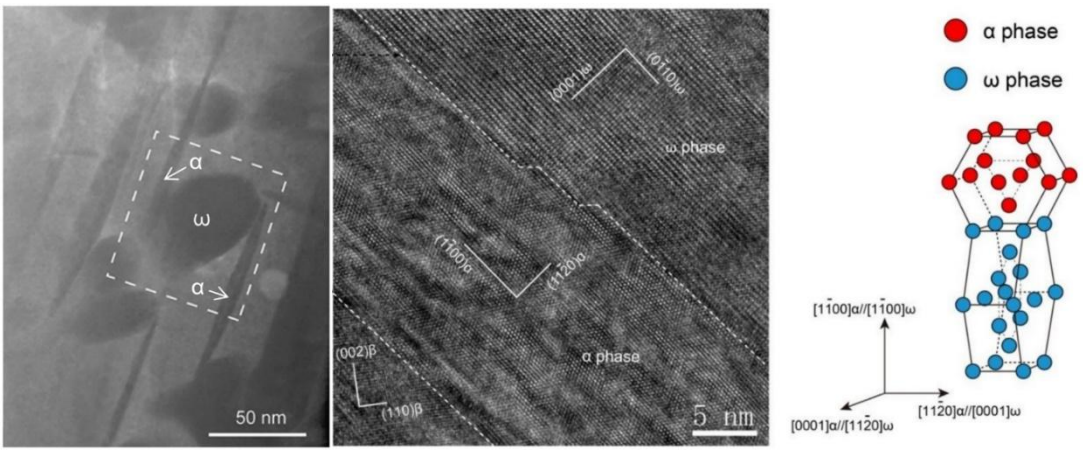

Figure 6.1 – Left - A typical mesoscale observation of α and ω precipitates in the β matrix. Center- HRTEM of the ω-α interface. Right – The ω-α lattice correspondence. Adapted from Li et al. 2018. [131]

6.2 Pseudospinodal alpha-phase

6.2.1 Background

As described earlier, the mechanism of ω-assisted α phase precipitation has been widely investigated for β-metastable Ti alloys subjected to up-quench (re-heating) aging heat-treatments [38,42,43,131–133]. However, another mechanism of α precipitation can also play an important role during aging heat-treatments of these alloys. According to Nag et al. (2012), thermodynamic calculations that predict a non-classical homogeneous formation of α phase in Ti-Mo based-alloys may accurately describe the reactions observed in Ti-5553 alloys at 600 °C, assuming minor compositional fluctuations of Mo at this temperature [134]. This reaction is often referred to as pseudospinodal. According to Nag et al (2012), pseudospinodal reactions can happen when "*the nominal composition of the parent phase lies close to the intersection point of the free energy-composition curves (G-X) of the parent and product phases for a particular temperature, and particularly, in the side where the free energy of the parent phase is lower than that of the product phase*" [134]. The fluctuations in the solute content are thermally-induced and can be estimated with the aid of the Landau-Lifshiftz distribution [135], whose variance "c" is given by Equation 3. A Gaussian probability density function (Equation 4) is often used to represent the compositional distribution at a given temperature.

$$\langle(\Delta c)^2\rangle = \frac{1}{\beta} = \frac{T}{N\left(\frac{\delta\mu}{\delta c}\right)_{P,T}} \tag{3}$$

$$\omega(x) = \sqrt{\frac{\beta}{2\pi}}\exp\left(-\frac{1}{2}\beta(x-\overline{\mu})\right) \tag{4}$$

In a follow-up paper, Boyne et al. (2014) performed a series of simulations of the pseudoespinodal process via the Langevin force method[8] and illustrated how the nucleation

[8]With this method, nucleation processes are associated with random fluctuation in the free energy landscape. Nevertheless, the method has several drawbacks, such as (1) dimensionless parameters (i.e. it is impossible to make a direct correlation with experiments) and (2) the contributions from the coherency elastic energy were ignored. However, despite being

rate changes with respect to composition and temperature. According to the simulations (Figure 6.2), the pseudospinodal pathway could prompt a sound increase of the nucleation rate of α-phase in Ti-Mo alloys, such as Ti-5553 and Beta-21S with only small changes in temperature, exactly as proposed by Nag et al. (2012).

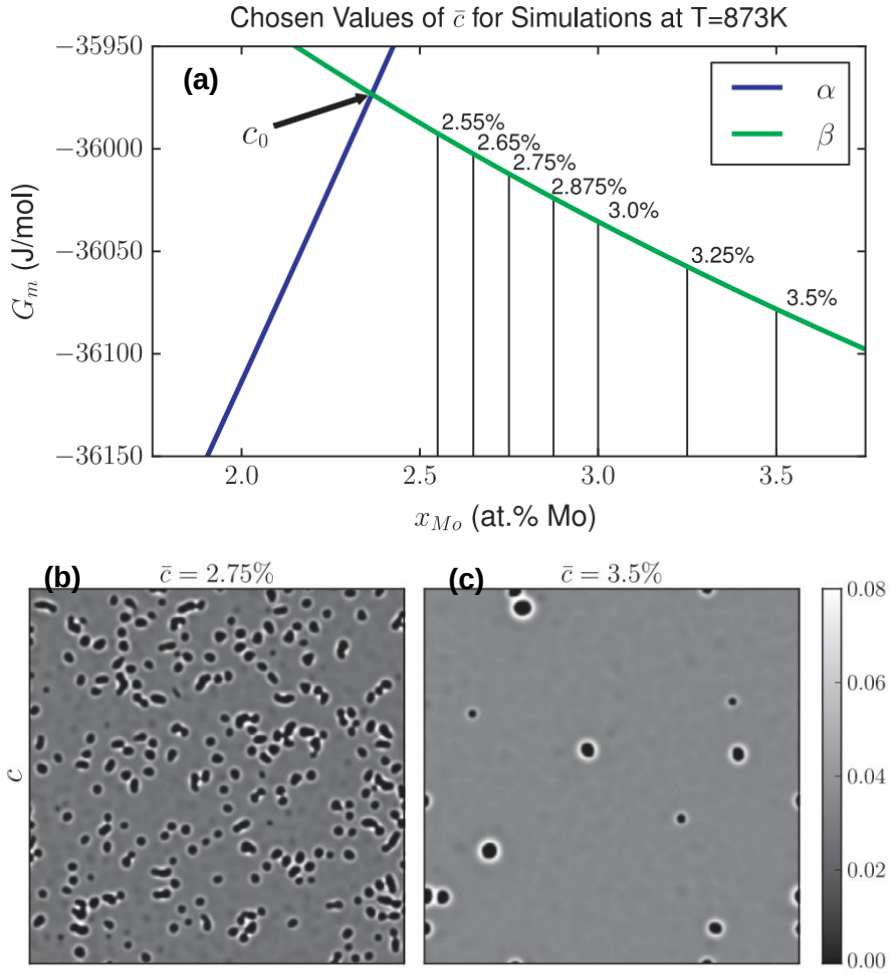

Figure 6.2 – (a) Free energy curves of the α and β phases in the region of the simulations with constant temperature (T= 873 K and c ~ 3.0%). At this temperature, the value of C0 – i.e., the intersection of Gα and Gβ - is 2.365%. (b) Composition fields closer and further from C0. Adapted from Boyne et al. (2014).

However, in the same way, Van Bohemen et al. had reported a congruent partitionless formation of α-phase that occurs at 615 °C in Ti-4.5Fe-6.8Mo-1.5Al. Using an electron probe

---

ignored, they can play an important role on nucleation, shifting c_0 toward the solute-lean side, and increasing the total energy barrier for nucleation.

micro-analyzer (EPMA), the authors observed a strong Fe partitioning between the β phase and supersaturated α phase laths, attesting that Fe plays an important in this transformation. On the other hand, at higher temperatures, they found that classical α phase precipitation was driven mostly by Mo and Al partitioning. Based on Van Bohemen's results and experimental setup, it seems they were the first ones to identify and characterize a pseudospinodal reaction, in this case, driven by Fe and not Mo fluctuations. With that in mind and considering this phenomenon had never been reported in Ti-Nb based alloys, we designed two Fe rich compositions from the Ti-Nb-Fe system, with relatively low Nb content, in which pseudospinodal decomposition could take place.

6.2.2 Pseudospinodal in Ti-11Nb-3.5Fe

In this study, the temperature at which pseudoespinodal could be activated (T_0) was estimated assuming that the α and β phase compositions were the same as those of the alloy compositions, i.e., C_0 = Calloy. The thermodynamic calculations were performed using the MatCalc package [136] and the same Thermo-Calc database utilized by Nag et al. (2012), referred here as Ti_data (2009).

Based on our simulations, T_0 increases from 407 °C (Ti-15Nb-3.0Fe) to 463 °C in Ti-11Nb-3.5Fe (Figure 6.3). Despite the difference between the [Mo]eq of the experimental alloys (11.7 and 12.3), the difference alone is too small to cause a significant shift in the G-X curves' intersection. Based on simulations with the Ti-Mo binary system, the shift would be only +19 °C between Ti-11.7Mo and Ti-12.3Mo wt% (Figure 6.3), while the shift observed between Ti-15Nb-3.0Fe and Ti-11Nb-3.5Fe is -55 °C. In other words, the shift is related to Nb and Fe contents in each alloy, and not to changes in the [Mo]eq.

At a temperature of 450 °C, we estimated the predicted Nb compositional variation for Ti-11Nb-3.5Fe using Equation 1. Figure 6.4 shows evidence that the non-classical α precipitation can be triggered in Ti-1135, given that the thermally-activated compositional variation at 450 °C extends to approx. 0.8 wt% Nb (6σ), although only 0.6 wt% (Fig. 6.4d) is needed to reach the G-X curves' intersection (C_0). In other words, Calloy lies minimally close to C_0, and the conditions for the pseudospinodal reaction to being active are therefore satisfied, despite Calloy < C_0 [137]. The same does not apply to Ti-15Nb3.0Fe, whose

composition is far away from the C_0 point at 450 °C, as can be seen in Figures 6.4c-e. In other words, the pseudospinodal reaction may not occur in the Ti-15Nb-3.0Fe alloy because of the heat treatment route chosen. It is worth reminding that the decision of choosing 450 °C as the aging temperature was arbitrary. According to the DSCs presented in the last chapter, 450 °C was surely above ω-*solvus*, ensuring no ω-assisted α-phase formation.

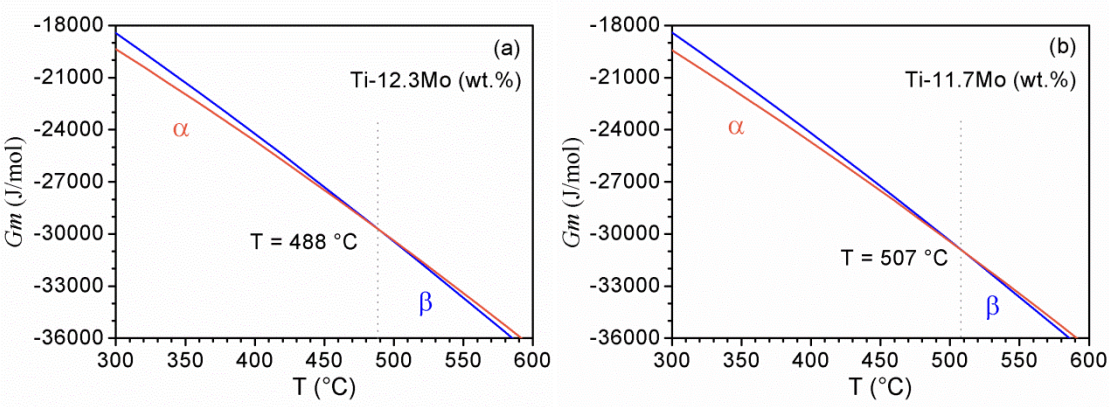

Figure 6.3 – G-X curves' intersections in Ti-12.3Mo (a) and Ti-11.7Mo (b). The curves are the Ti-Mo binary equivalents of Ti-1135 and Ti-1530, respectively.

Figure 6.5 shows dense concentrations of α precipitates in both compositions, which appeared in response to step-quenching at 450 °C; however, the apparent nucleation rate increased markedly in Ti-11Nb-3.5Fe. Also, note that the precipitates are distributed homogenously throughout the entire sample. Thus, it seems that 450 °C is reasonable temperature to obtain fine and well dispersed intragranular α precipitates in Ti-11Nb-3.5Fe alloy, regardless of ω-assisted α phase precipitation.

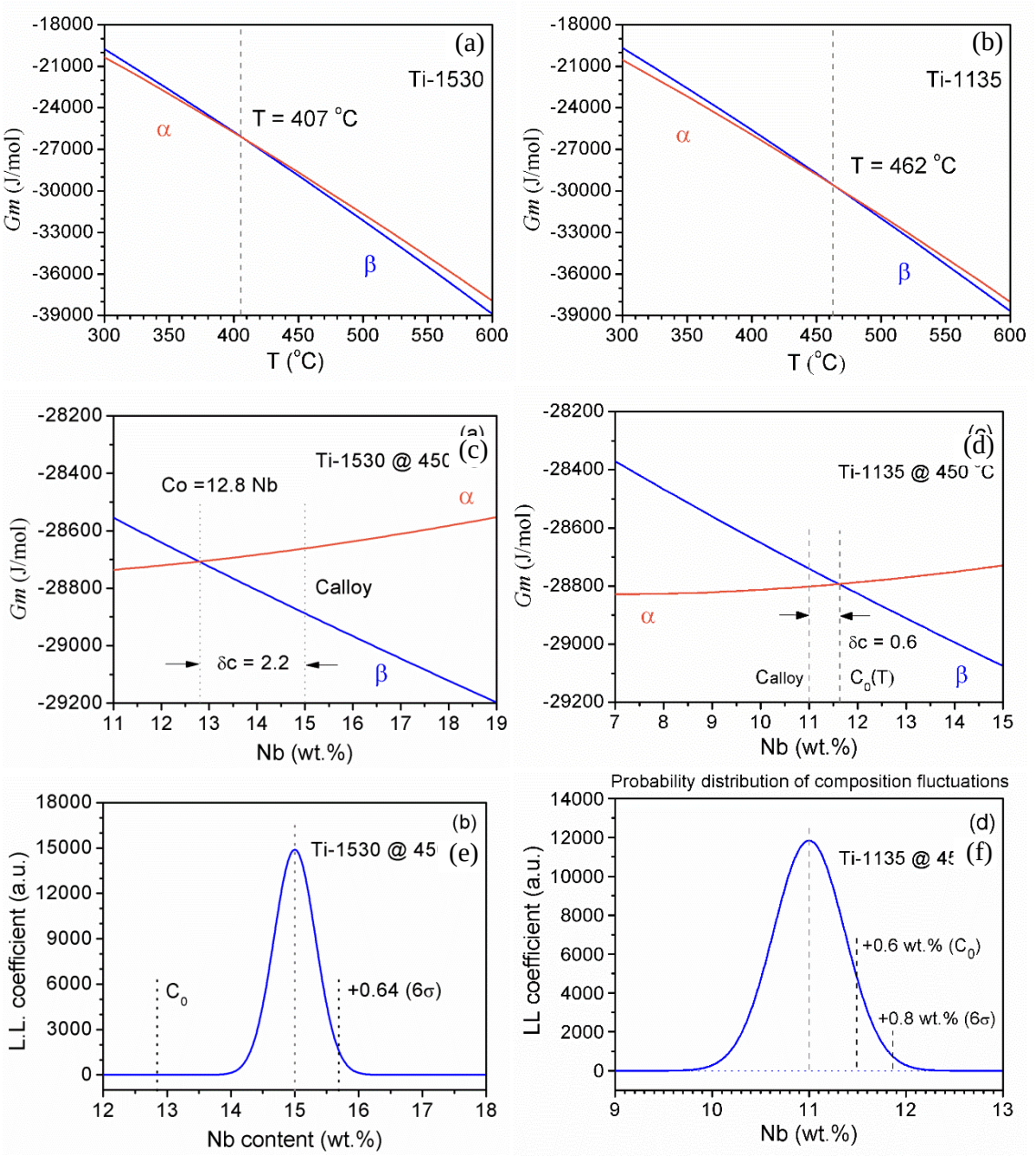

Figure 6.4 – Optimal temperature (T) for pseudospinodal decomposition in (a) Ti- 15Nb- 3.0Fe and (b) Ti-11Nb-3.5Fe, (c) G-X curves for α and β phases at 450 °C, showing the proximity between the composition that most likely undergoes spinodal decomposition (11.6Nb) and the average composition of the alloy (11Nb), and (d) compositional fluctuations at 450 °C predicted by the Landau-Lifshitz equation.

The TEM images presented in Fig. 6.6 show that the thickness of the α phase laths nucleated at 450 °C is less than 80 nm, and that the OR relationship (111)β // (11-20)α is

satisfied [8]. The three main crystallographic variants are visible, proving that this mechanism is non-selective in terms of crystallographic orientation. Based on the SEM-STEM images (Fig. 6.6b-c) we counted about 200 α phase laths within 14 μm^2. The aeral number of laths, of ~ 14 laths/ μm^2, is higher than those determined by Zheng et al. [138] for Ti-5553 step-quenched to 600 °C (~ 6 laths/μm^2). No ω phase was detected, as expected. The compositional line profile (Fig. 6.6b) indicates rapid depletion of Fe; thus the growth of α laths must be subsequently limited by Nb diffusion until the laths reach another nucleated variant in their vicinity. From left to right, three α phase laths (darker) are visible in Fig. 6.6b. The laths all have a similar composition, with an average Nb content of 8.3 wt%. Furthermore, a negligible amount of only 0.2 wt% of Fe was left inside the laths; β phase in the vicinity of two α phase laths seems massively enriched in Nb and Fe, presenting 20.3 wt% Nb and 6.5 wt% Fe, similarly to the β phase detected in the FC samples. In summary, the finer α phase that precipitated during the step-quench is still far from the equilibrium composition, probably due to a lower Nb diffusion coefficient at 450 °C.

In this section, new pieces of evidence were provided that the mechanism proposed by Nag et al. (2012) and Boyne et al. (2014) could be activated in Ti-11Nb-3.5Fe (wt%) alloy. Fe appears to play an important role in the transformation, being depleted from the α phase nuclei. An analogous case has been observed in steels, upon analysis of C redistribution during the early stages of bainite transformation at low temperatures [139].

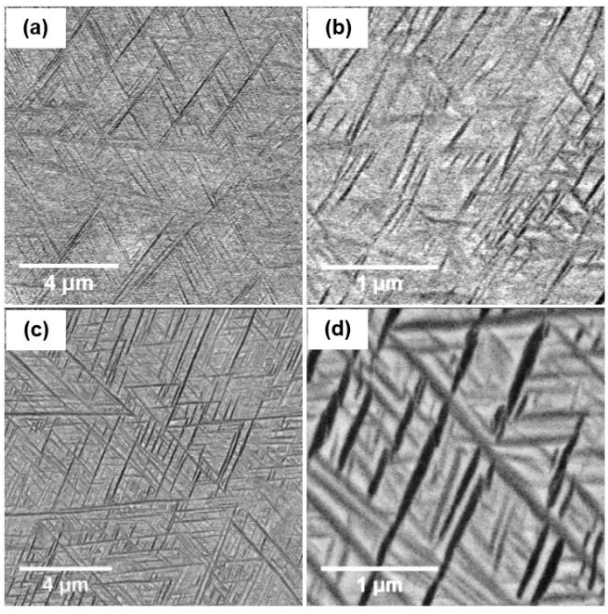

Figure 6.5 – FE-SEM BSE images of Ti-15Nb-3.0Fe (a and b) and Ti-11Nb-3.5Fe (c and d) subjected to recrystallized/solution heat treatment and step-quenched to 450ºC for 30 min.

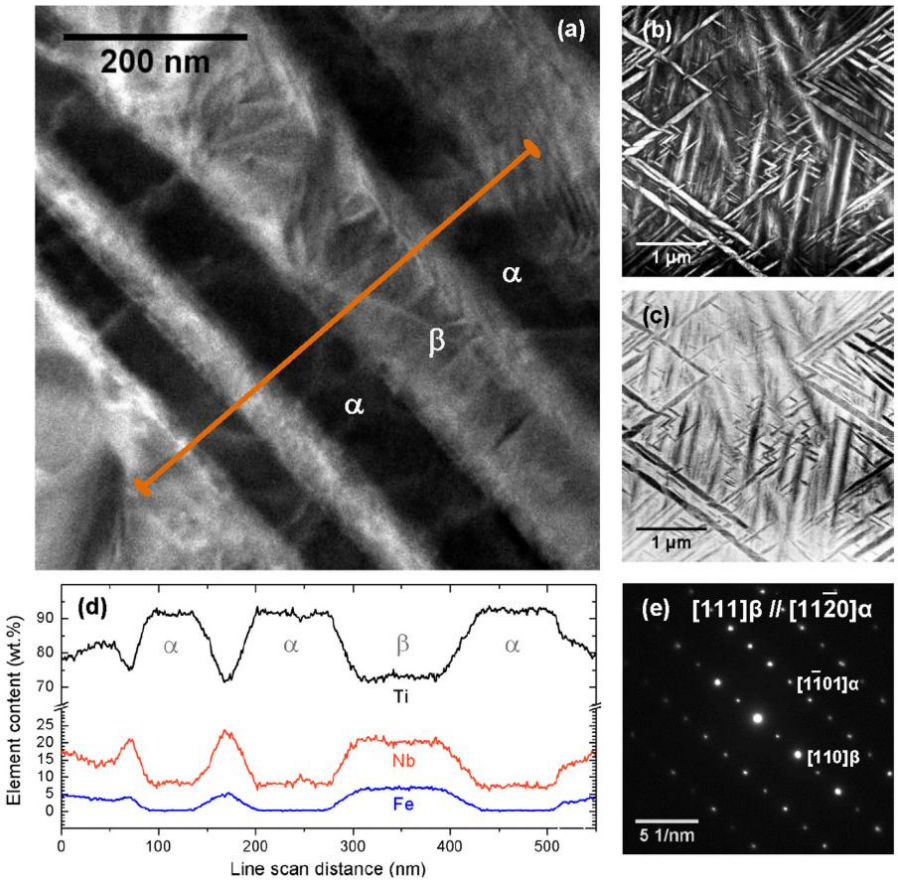

Figure 6.6 – Ti-11Nb-3.5Fe solution-treated followed by SQ to 450 °C for 30 min: (a) Bright-field TEM-STEM image; line scan indicated in orange, (b) HAADF SEM-STEM image, (c) Bright- field SEM-STEM image, (d) EDS line scan measurements along the orange line* and (e) TEM selected area diffraction through <111>β zone axis. *Preliminary line scan performed on a JEOL2100F without any K-factors correction.

6.2.3 New CALPHAD assessments

According to preliminary data [140], Ti-11Nb-3.5Fe (wt.%) alloy could have the pseudospinodal mechanism triggered near 450 °C. However, based on the new ThermoCalc® database (TCT1) released on December 2017, the actual composition that could undergo pseudospinodal at this temperature would be Ti-6.5Nb-3.5Fe (wt.%) - see Figure 6.7a. With this new database, the Gibbs free energy curves shifted drastically compared to the previous database, thanks to improvements from the incorporation of more than 30 assessments of Ti-related ternary systems (e.g., Ti-Fe-X, Ti-Al-X, and others). Also, the new database predicts a great change due to the Zr addition, which is also at odds with the previous database. Based

on this controversy, CALPHAD data did not clearly demonstrate whether pseudospinodal could be activated or not. Thus, further studies on the mechanism of α-phase formation were necessary, especially for the earlier stages of the transformation – i.e., shorter aging times – which will be presented in the next section.

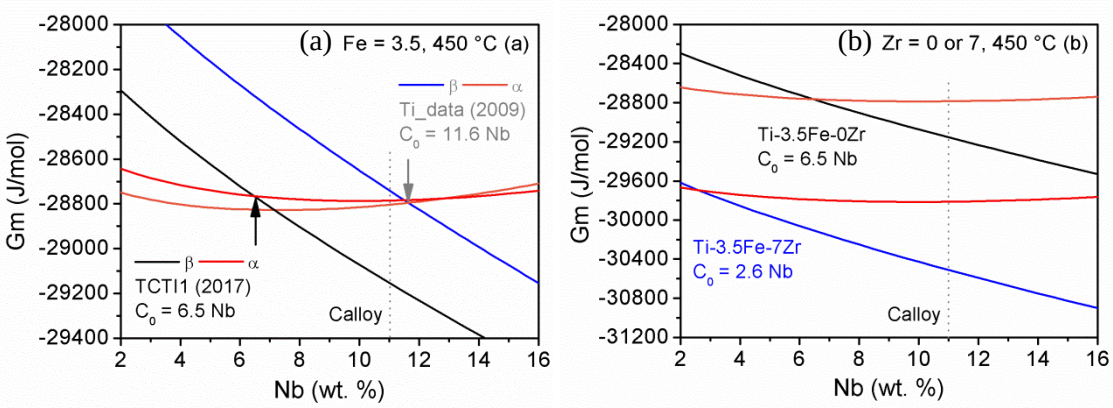

Figure 6.7 – Comparison between the old (Tidata_2009) and new (TCT1_2017) ThermoCalc databases (a) and the influence of Zr addition on the Gm curves (b).

6.2.4 Early stages of α-phase formation

Given the limitations on the STEM-EDS data obtained in Figure 6.6 and the divergences between previous and modern thermodynamic databases, we decided to explore the early stages of α-phase formation with short-time aging heat-treatments to further evaluate the problem.

The pivoting point of this work, compared to previous studies by Nag et al. [134] and Boyce et al. [137], was the shortest aging time (1 min) evaluated. Before that, the earlier nucleation stage evaluated in this respect had been after 10 min of aging in a Ti-5553 alloy (Ti-Mo based). At the 1 min aging condition, we expected to see intragranular, nanometric clusters of α-phase derived from the pseudospinodal reaction. On the opposite, primary α-phase precipitates at grain boundaries (GBs) are observed in Figure 6.8. With that, we turned our attention to the reactions happening at the grain boundaries and performed an in-through analysis with the aid of STEM.

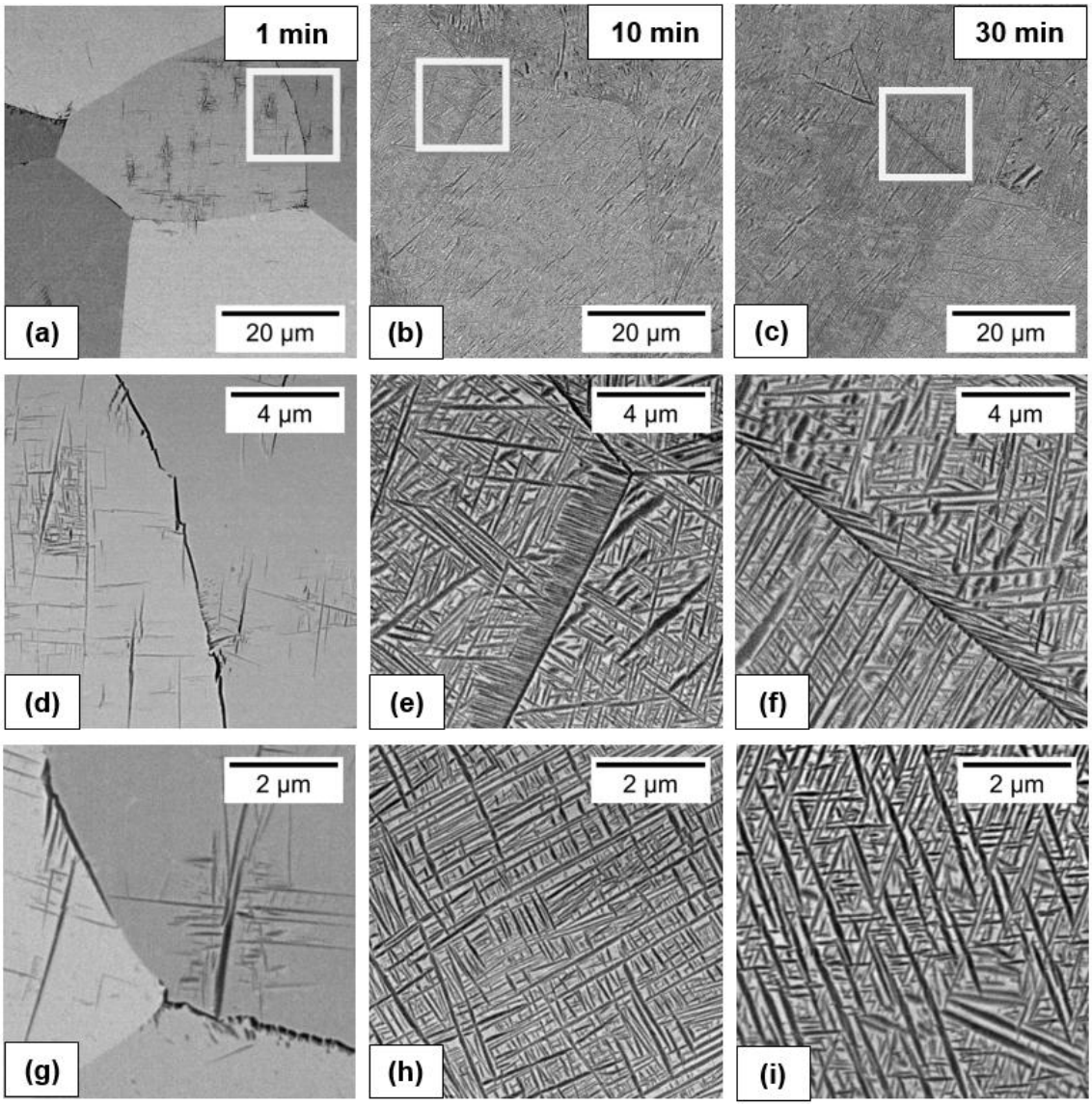

Figure 6.8 – Ti-11Nb-3.5 (wt.%) aged for 1 (a, d, g), 10 (b, e, h) and 30 min (c, f, i). Images recorded with the aid of a backscattered electrons detector (BSE) on an FEI Apreo system.

The secondary variants displayed inside the grains appear to emanate from the grain boundaries (Figures 6.8 and 6.9). Almost every GB display α-phase precipitation. According to the literature, the movement of fast diffusing elements along boundaries has great influence on the generation of compositional gradients in multi-component alloys, especially at lower temperatures and extremely short annealing times. In these kinetic regimes (B-C), the diffusion length $(Dv.t)^{1/2}$ at a given temperature is smaller than the diffusion through grain boundaries; then, grain boundary precipitation tends to occur faster. The main strategy for suppressing the GB α-phase formation would be increasing the aging temperature, but that

would lead us to ignore the previous conditions for pseudospinodal. Other options would be to (1) limit the GB diffusion by changing the composition or (2) increasing the grain-size [92].

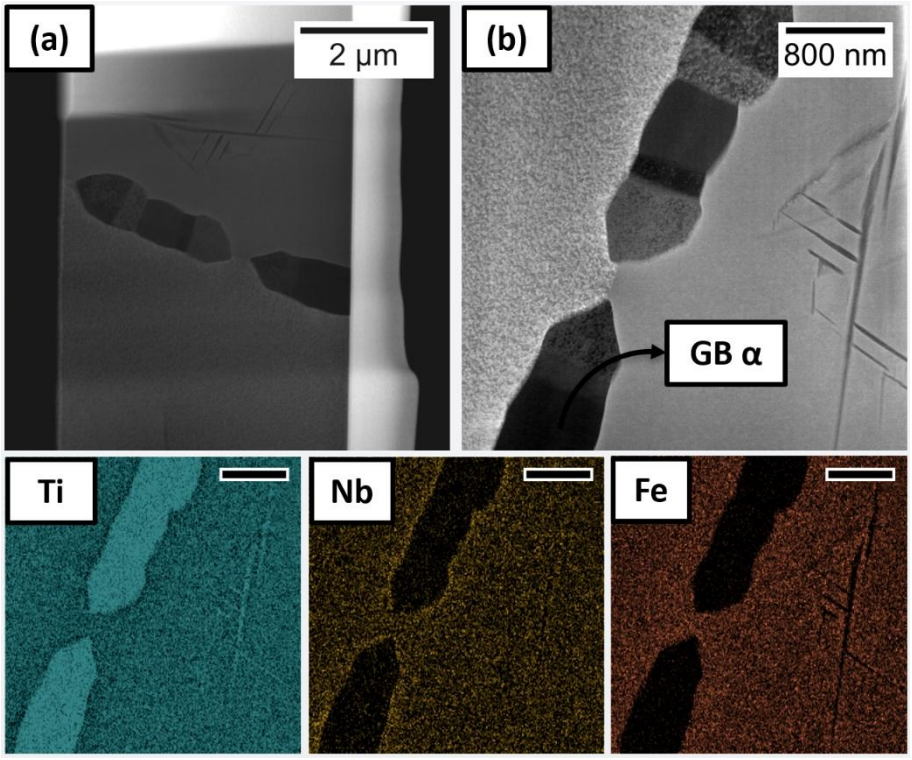

Figure 6.9 – (a, b) HAADF images of the α-precipitates in Ti-11Nb-3.5Fe aged for 1 min. At the lower part, the elemental mapping obtained via STEM-EDS is presented.

From a compositional perspective, given the limited aging time (1 min), the intragranular precipitates (IG) are still moderately rich in Nb and Fe, comparing to the grain-boundary GB-α, as can be seen comparing Figures 6.10 and 6.12. However, even at this earlier stage of nucleation, α-phase has fewer solute elements than expected by the thermal-induced compositional variance at 450 °C. We concluded, thus, that the pseudospinodal mechanism is not the dominant one in this system, being the GB α-phase formation the lowest energy (and probably first-to-happen) mechanism.

Samples aged for 10 min and 30 min still display GB-α; however, based on our STEM results, it seems that compositional partitioning between matrix and particles are similar to IG-α after such times. For example, at this condition, GB α and IG α have the same Fe content

– which tends to zero. Thus, it seems the time the material spends at 450 deg C is enough to extinguish local gradients created at GB at the earlier stages of aging. A compilation with the STEM-EDS data from all samples is presented in Figure 6.12 and Table 6.1.

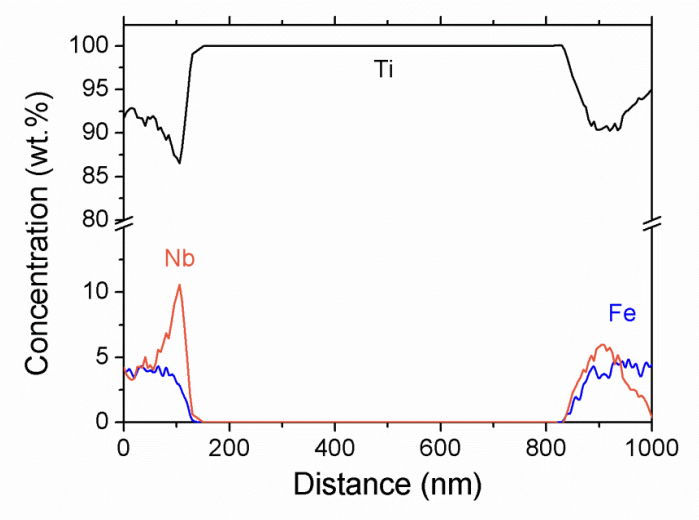

Figure 6.10 – Composition of the alpha-phase at the grain boundaries in Ti-11Nb-3.5Fe measured via STEM-EDS on a Tecnai F20.

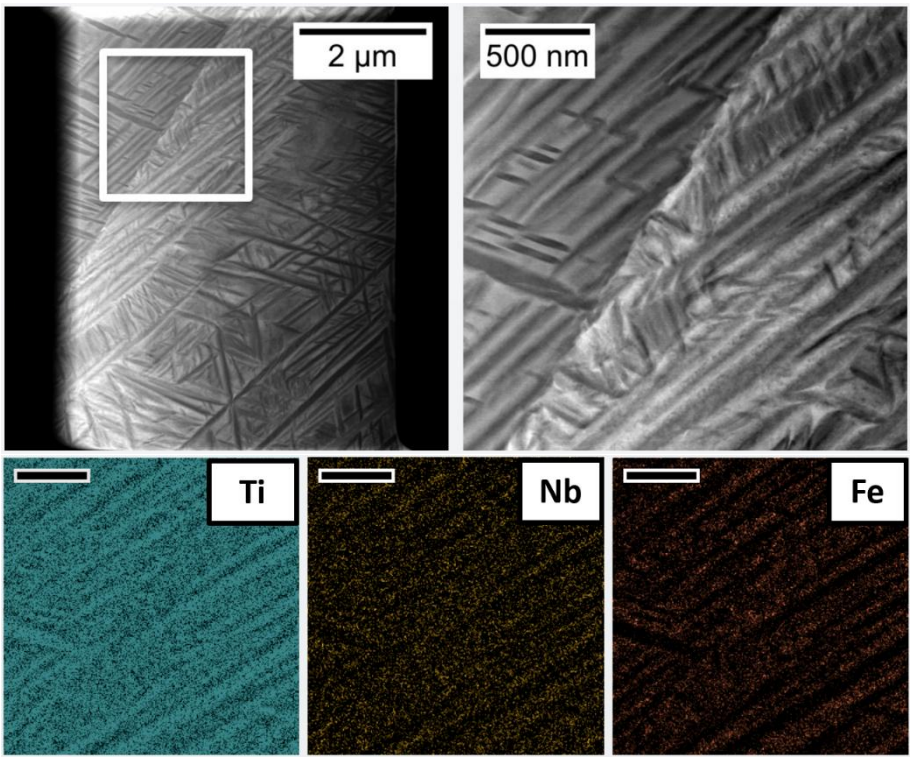

Figure 6.11 – (a, b) HAADF images of the α-precipitates in Ti-11Nb-3.5Fe aged for 30 min. At the lower part, the elemental mapping obtained via STEM-EDS is presented.

It is apparent from Figure 6.12 that very few precipitates were formed inside the grains. These findings further support the idea of grain boundary α-precipitates are formed first, and then give origin to the IG-α seen in Figure 6.11. According to Banerjee et al., side-plates that emanate from GB α-phase usually dominate the microstructure if the transformation takes place at high temperatures, e.g., during slow cooling [8]. However, this is not the case presented here, given the cooling rate from ST temperature in our experiments is relatively high, and the aging temperature selected for this work is relatively low, thus limiting the extent to which the GB side-plates are observed to a few microns (see Fig. 6.8e and 6.8f)

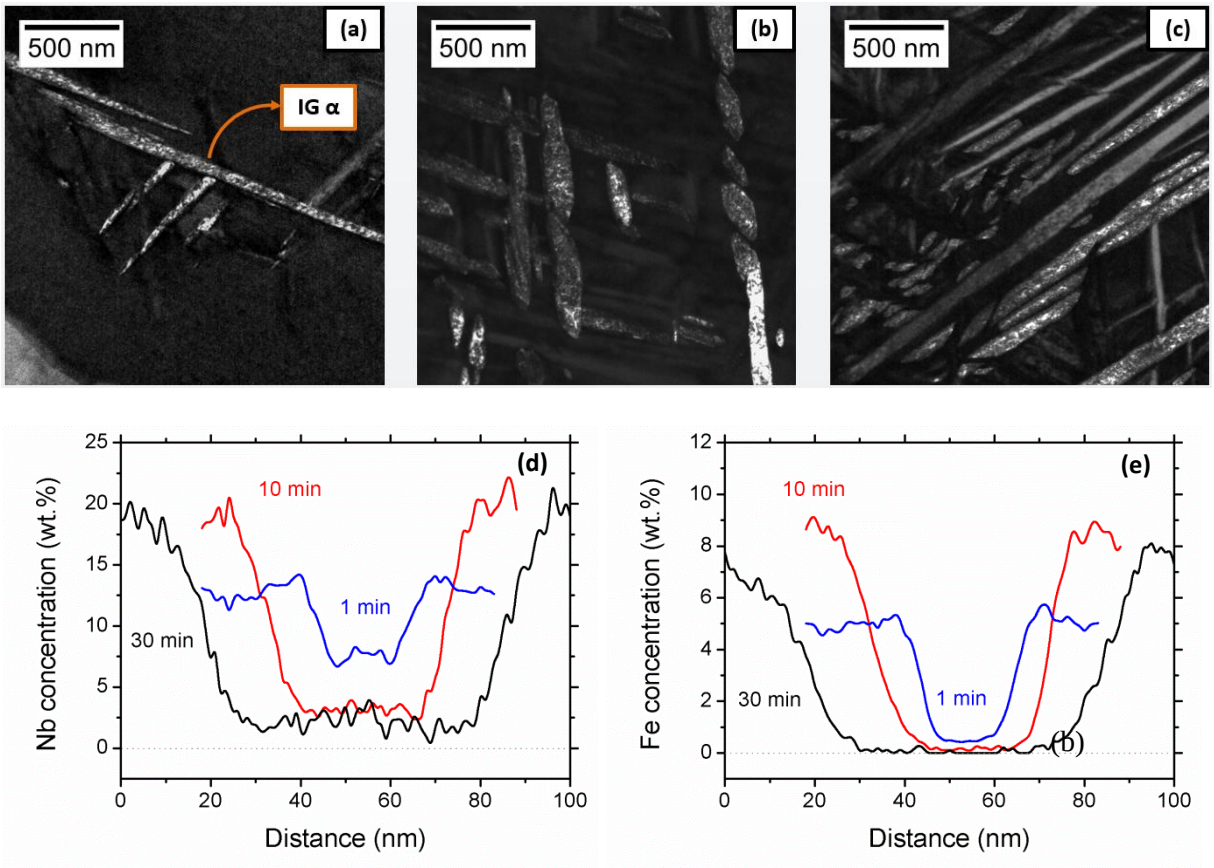

Figure 6.12 – (a, b, c) Dark-field images of the intragranular alpha precipitates after 1, 10 and 30 min, respectively. Variations in Nb and Fe concentrations between beta and alpha (core) by STEM-EDS measurements. A compilation with these results is presented in Table 6.1.

It seems that the precipitation of grain-boundary α-phase prevails over other mechanisms of α-precipitation in both ternary systems. Even though, independent IG α-phase

might still be formed. One downside regarding our methodology is that it is not possible to be positive of the exact nucleation mechanisms that took place within the first minute of aging since the analyses were performed post-mortem (i.e., after 1 min). The activation of GB α-phase formation, however, would explain the marginal ductility and the GB brittle and intergranular fractures observed among microstructures containing super-refined α-phase when subjected to fatigue tests [85].

Interesting results were found in this work, mainly regarding the element partitioning between β and α during the α phase precipitation and growth. Nevertheless, it has not been possible to account for most observations using the classical nucleation theory to interpret the nucleation mechanisms among Fe rich-alloys [141]. During aging heat-treatments, α phase precipitates are quickly formed at the grain boundaries, strong (and quickly) rejecting Fe. In Ti-5553 [134], Al appears to play an analogous role in the α-phase precipitation, displaying the opposite behavior of Fe, given that it is rapidly incorporated into α phase laths.

Similarly to the quick rejection of Fe reported here, an analogous case has been observed in steels, upon analyses of C redistribution during the early stages of bainite transformation at low temperatures [139]. Furthermore, our results have several similarities with Van Bohemen et al. ’s (2006) findings, in which the authors reported the formation of α-phase “black plates” as a product of a bainitic-like reaction. For that matter, a model which displays the bainitic ferrite growth in steels is presented side-to-side with a series of images recorded during Van Bohemen’s experiments and SEM images acquired through this thesis (Figure 6.13). The similarities between results and model are astonishing; however, this question is still open to debate. Carefully designed in-situ experiments will be necessary to confirm this hypothesis. Further data to support a GB-mediated α-phase formation is presented in the following section (section 6.3).

Concerning the α-phase kinetics, based on the compositional profiles above, it is possible to affirm that the α laths growth is later limited by Nb diffusion until they reach another variant nucleated in their vicinity. Therefore, we decided to carry on with the STEM-EDS data analyses and try to model the α-phase growth. Herein, a diffusion-based model was chosen to describe the α-phase growth observed in Ti-11Nb-3.5Fe (wt. %) at the GBs and inside the grains, as follows (section 6.4).

Table 6.1 – Compilation of the STEM-EDS data* for several HT applied to Ti-11Nb-3.5Fe.

Isothermal hold (min)	Location	Nb content (wt.%)		Fe content(wt.%)	
		α (core)	β	α (core)	β
1 min	GB	0	7.4	0	3.9
1 min	IG	5.1	12.8	0.4	7.9
10 min	IG	3.1	17.6	0.2	8.2
30 min	IG	1.3	18.6	0	7.6

*Uncertainty associated with these measurements is estimated to be around 0.01*content

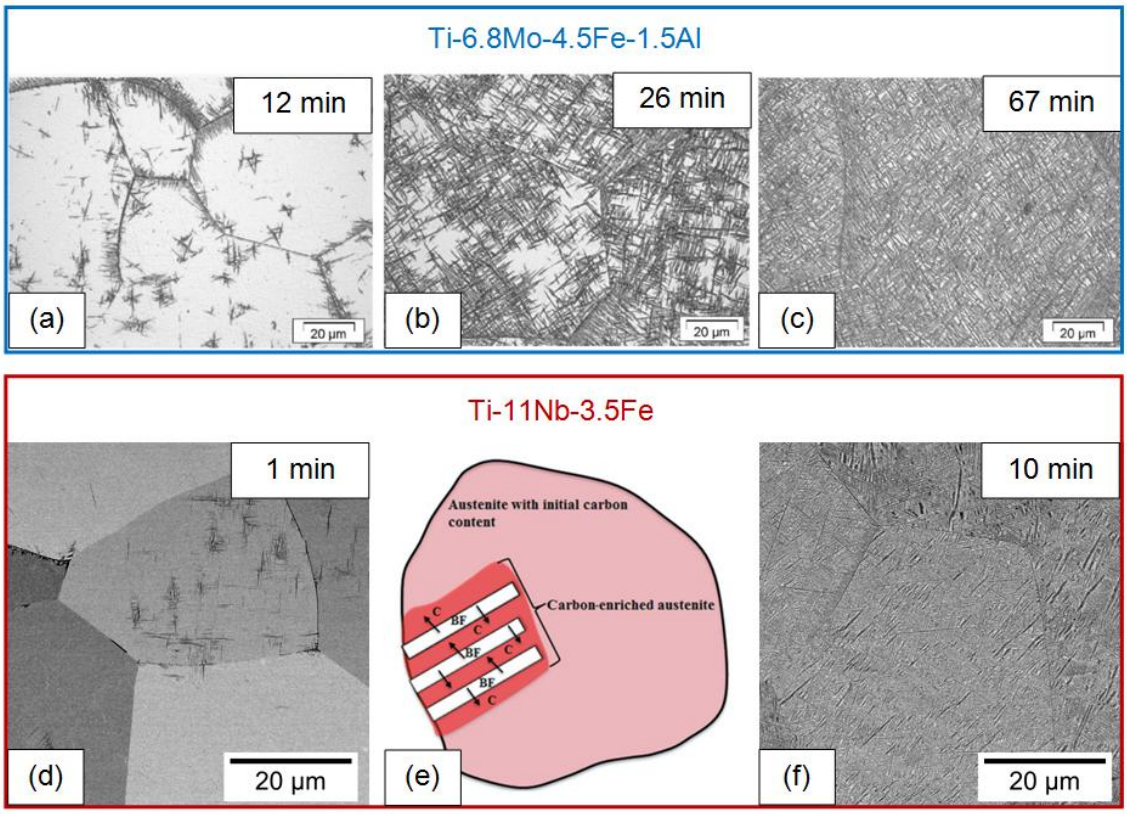

Figure 6.13 – Comparison between the Ti-Mo-Fe-Al (a, b, c) – extracted from Van Bohemen et al. (2006) [142] - and Ti-Nb-Fe systems under similar aging conditions. The α precipitation evolves faster in the Ti-Nb-Fe system. A model for the bainite ferrite in steels is presented in (e), extracted from Timokhina et al. (2016) [139].

6.3 Grain boundary reactions in the Ti-Nb-Fe system

In this section, we will apply the model by Xing et al. (2018) – described in the introduction - to the Ti-Nb-Fe system. The enthalpy of mixing between Ti, Nb, Fe, Zr, and Sn was compiled and are presented in Table 6.2. Making use of the same method (Chapter 2, Equation 1) and assuming[9] coefficients a, b, c = 1/3, we estimated the effective enthalpy of GB segregation for Fe (element C) among many systems explored through this work. Beyond the calculations, a detailed discussion on the influence of each pair of elements' enthalpies of mixing on the phase transformations that occur at the GBs was elaborated. It is worth mentioning that the model agrees with the experimental observations. Thus, we paid special attention to its use, as follows. For all systems, elements will be referred to as A-B-C for simplification purposes (A – base element, B – main alloying element, C – ternary alloying element).

In our binary system, the enthalpy of mixing of Ti-Nb is negative, but close to zero (approx. -15 J/mol); thus, little or no segregation to the GBs is expected. When we add Sn, the effective enthalpy of GB segregation for Sn can be estimated using Equation 2 as -37 J/mol, considering the enthalpies of each pair as H_{mix}(A-B) = +8 J/mol, H_{mix}(A-C) = +100 J/mol and H_{mix}(B-C) = -26 J/mol. Given these enthalpies, it can be inferred that both Nb and Sn can be segregated to GBs, but the site competition between them might decrease the overall segregation efficiency. This prediction corroborates with experimental data from the literature: in this system, the precipitation at GBs only occurs after extended aging heat-treatments, of 24-48 h [94]. As for the Ti-Nb-Fe system, one should pay special attention to the enthalpies of mixing of Ti-Fe (-32 J/mol) and Nb-Fe (-22 J/mol), both indicating a strong tendency of these elements to bond to each other. From the pair's enthalpy, we can use Equation 2 to estimate the net enthalpy of GB segregation for Fe as +6 J/mol - which points to a moderate Fe segregation. However, Fe segregation might increase Nb segregation as well. This phenomenon is known as co-segregation of Nb induced by Fe. Our experiments also agree with these predictions. The higher the availability of Fe atoms in the alloy - i.e. the smaller the Nb/Fe ratio - the more prominent is the precipitation of α-phase observed at the

[9]In particular, the analysis of the coordination number for a GB with 2xBCC lattices was problematic. Coordination number is likely between 3 and 4 for most low-index zone axes, so we assumed 3.

GBs after 1 min of isothermal annealing at 400 deg C. On the other hand, in alloys with a reduced Fe content, phase-transformations occur slowly, as in the Ti-Nb and Ti-Nb-Sn systems.

After all, despite the success of using the model of Xing et al. (2018), there are a few sources for error associated with this model. The most important one is related to the enthalpies of formation of specific elements. The Miedema model, for example, contemplates only metallic bonds; thus, it cannot predict the influence of elements such as B, C, N and O on the enthalpy of formation of binary compounds. Also, the model describes in a precise manner only enthalpies of mixing of transition metals, which have multiple valence states. In the case of Sn, the Miedema enthalpies are only estimations based on specific Brillouin zones available and the expected crystal structure for that binary system. In other words, the enthalpies of mixing of Ti-Sn, Nb-Sn, and Fe-Sn are potential sources of error and could be refined via atomistic techniques.

Table 6.2 – Enthalpies of mixing of some binaries at the proportion of 1:1

Binaries	**Miedema (J/mol)**			**RKM (J/mol)**		
	ΔHmix	**ΔHseg**	**ΔHint**	**ΔHmix**	**ΔHseg**	**ΔHint**
Ti-Nb	8.031	-15.408	8	11.742	-14.970	12
Ti-Sn	99.811	25.272	-163			
Ti-Fe	-31.159	26.213	-62	3.061	38.348	-49.7837 + 0.0231*T
Nb-Fe	-22.191	42.161	-57	1.933	64.340	-32.5147 + 0.0063*T
Nb-Sn	-25.527	52.404	-68			
Nb-Zr	26.461	19.478	17	1.143	17.603	-14.6427 + 0.0055*T
Fe-Zr	-35.220	61.444	-118	-19.000	37.318	-97
Fe-Sn	92.310	138.873	-8			

*Data extracted from [143].

Another approach to analyzing how the GBs influence many properties of functional materials has (re)appeared last year. It consists of analyzing structural transitions at interfaces (such as GBs) as “two-dimensional” phase transformations. According to classical literature, transitions at GBs can be categorized into congruent or faceting types, being the later much more common in metallic systems [144]. In a recent paper by Peter et al. (2018), the authors

detected a nanoscale faceting transition at GBs in Cu-Ag alloys induced by segregation of Ag. According to the study, overall GBs in pure-Cu appear to be flat, even after annealing at 800 deg C for 120 h. On the opposite way, the sample doped with Ag presented symmetric and asymmetric clusters at GBs with a length close to 2 nm, with Ag atoms being concentrated in the symmetric segments. The stabilization of such facets at GBs upon cooling indicates that GB phase transformations can also occur for any GB orientation/inclinations whenever a solute has a low solubility in the bulk and symmetric GB structures with high solute adsorption exist [145]. We believe this is a mechanism that could be associated with quick α-phase precipitation seem in the Ti-Nb-Fe GBs. Not only the diffusion of Fe is greatly enhanced at GBs (section 6.4), the formation of small and faceted clusters at the GBs might operate as effective nucleation sites for the α-phase, given their specific interfacial properties.

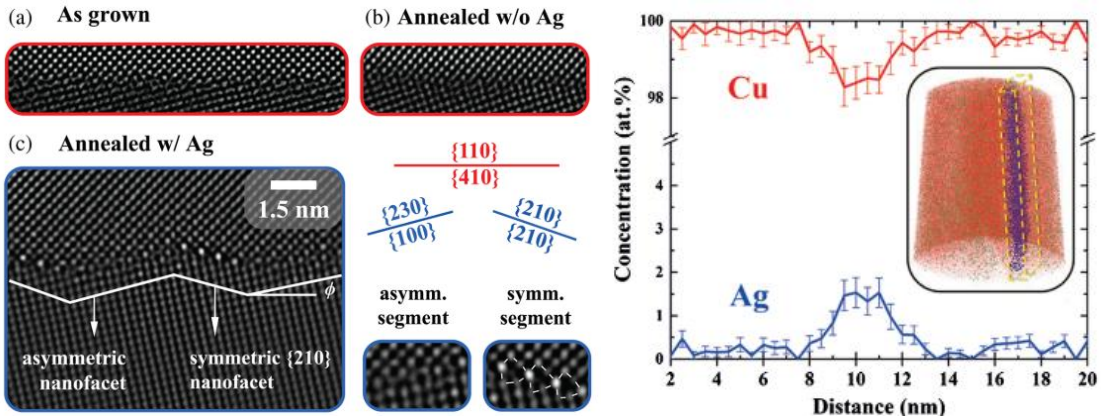

Figure 6.14 – HAADF STEM micrographs in [001] zone axis orientation of (a) the relatively flat as-grown GB structure, (b) the relatively flat annealed GB structure, and (c) the Ag-segregated GB structure exhibiting distinct faceting with preferential segregation to the symmetric {210} segments. The scale applies to all a, b, and c. 3D APT reveals the inhomogeneous segregation of Ag to the asymmetric GB (d) 1D line profile across the boundary. Samples aged at 800 deg C for 120 h. Adapted from Peter et al. 2018 [145].

6.4. Diffusion of Fe

In a recent study in collaboration with Costa et al. (2016), results concerning the classical α phase formation in Ti-30Nb and Ti-30Nb-1Fe alloys were reported. It was

concluded that Fe addition to binary Ti-30Nb allows α-phase to form at lower temperatures, reducing by 40°C the temperature at which the heterogeneous α-phase precipitation begins. Also, Fe alters the α-phase precipitation kinetics, making it viable during continuous heating at any heating rate from 2 to 600°C/min. The addition of 1 wt. % Fe to Ti-30Nb alloy also refines the precipitation of α-phase. It is believed that all of these observations are related to the faster diffusion of Fe in the β-phase matrix – Fe's diffusion coefficient is 90 times greater than Nb one at 550°C [112]. According to the solid-solution diffusion coefficients found in Smithells Metals Reference Book [116], at 450 °C (723 K), Nb diffusion occurs with D = 1.84 x 10^{-20} m²/s, while Fe diffusion is almost 80 times faster than that[10], reaching D = 1.44 x 10^{-18} m^2/s.

6.5 Ledgewise growth

Enomoto & Fujita (1990) proposed a useful approach to model the α-phase growth in Ti alloys, termed as the α-phase "ledgewise diffusion growth" mechanism [146]. The model was based on the microstructural development of bainitic-ferrite in steels, in which a shear-mode enables a quick transformation for short distances, with subsequent solute redistribution between parent and product phases during rest periods [146]. In the past, the thickening of proeutectoid α-plates in the Ti-Fe system was also related to a bainitic phase formation [63]. Notwithstanding, differently from steels, in Ti-alloys, the α-phase is not necessarily a product of a eutectoid reaction. Furthermore, a few aspects of the transformation such as the formation of an invariant plane strain (IPS) surface and other aspects of PTMC (phenomenological theory of martensite formation) are still open to debate, according to Aaronson et al. [147], and will not be inspected here.

One aspect of the β to α phase transformation that reinforces the validity of Enomoto's model is the lattice-site correspondence between β and α after the α-phase formation. As we know, ledges at the interface boundaries between β and α are linked to a partially coherent interface, which could support a mechanism of growth ledge by ledge. In this section, we intended to put the ledgewise growth model to use and then compare it to the experimental

[10] D_0 and Q (the activation energy) are reported on pages 94 (Nb) and 87 (Fe), respectively. By choosing a specific temperature, it is possible to estimate diffusion at that temperature with a simple Arrhenius plot.

data presented in the last section. Additionally, we used Enomoto's equations to estimate the effective diffusion coefficients in Ti-11Nb-3.5Fe and compare them to previous data from the literature. In summary, Enomoto's model can be synthesized in Equation 5. With equation 5 it is possible to obtain the composition at a specific position (x) relative to the center of the plate after a given time (t), given the initial concentration of a specific solute, the diffusion coefficient of that solute, and half-width of the α-phase lath.

$$c = \frac{C_0}{2}\left[erf\left(\frac{w+x}{2\sqrt{Dt}}\right) + erf\left(\frac{w-x}{2\sqrt{Dt}}\right)\right] \qquad (5)$$

$$C_0 = initial\ concentration;\ \text{erf} = error\ function; w = \alpha\ half - width$$

Assuming a ledgewise growth for the α-phase, we computed the Nb and Fe profiles near the β-α-interface for many annealing times. Let's start with the regular volume (intragranular) diffusion. The reported levels of Nb and Fe measured via STEM-EDS at the core of the IG α-laths are 7.9 and 0.4 (wt.%), respectively (Table 6.1). The average levels of the same elements near the outer edges of the laths (i.e., in the neighbor β-phase) are 12.8 and 5.1 (wt.%), respectively. For the model, assuming an α-lath width of 20 nm, therefore a half-width of w = 10 nm, t = 60 s, and choosing "x" to be inside and outside the laths, 2 nm from the edge interface – i.e. x_i = 8 and x_o = 12 nm, we estimated the compositions at x_i and x_o with the aid of Smithells diffusion coefficients [116]. The thermally induced compositional variance (3σ) was added to C_0 for each element[11]. According to the model, after 1 min, Nb levels should be 9.7 and 11.9 (wt.%) inside and out of the α-laths, respectively. In other words, if the transformation proceeds as a ledgewise growth, the diffusion coefficients from Smithells are slightly underestimated. To match the solute delta between inside and out of the laths of the experimental data, we estimate the diffusion coefficient of Nb at 450 ºC should be D_{Nb} (450 ºC) = 5.10^{-20}, i.e., 3 times greater than the reported coefficient on Smithells book. For Fe, to ensure a core with less than 0.5 wt.% of Fe in such a short annealing time, the effective diffusion coefficient had to be at least D_{Fe} (450 ºC) = 3.10^{-17}, i.e., 20 times greater.

[11] Enomoto & Fujita (2000) considered C_0 to be the nominal composition. In this respect, the composition differences between matrix and precipitates we found are slightly higher than those estimated with the original equation.

Still, in this case, the differences between the model and experimental data for intragranular α-phase can be considered small – see Figure 6.15 - just of about one order of magnitude.

Let's now turn our focus to the GB precipitates. Since both GB and IG-α present a negligible amount of Fe (0.2 and 0.4 wt.%) and knowing they were annealed for the same time (1 min = 60s), it is possible to rearrange Equation 6 and write the GB diffusivity as a function of the α-lath width (w). While the average width of the IG-α was 20 nm, the GB precipitates were way thicker, reaching approx. 720 nm. With that, we conclude GB diffusion of Fe should be approx. 1600 greater than its volume diffusion.

$$\tau_{0.1} \approx \frac{1}{D_V}\left(\frac{w_V}{0.18}\right)^2 = \frac{1}{D_{GB}}\left(\frac{w_{GB}}{0.18}\right)^2 \rightarrow \frac{D_{GB}}{D_V} = \frac{720^2}{20^2} \cong 1600 \qquad (6)$$

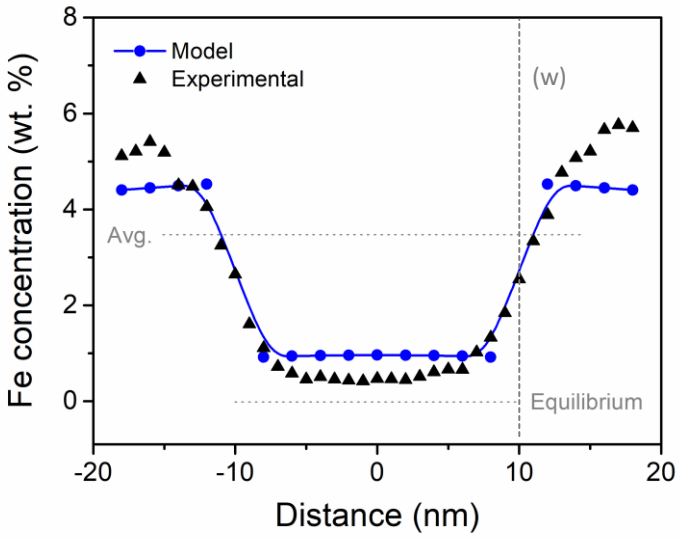

Figure 6.15 – Simulation of the residual Fe inside the intragranular α-phase laths for various distances (x). Values obtained with aid of Equation 6.1 assuming -20 > x > 20, t = 60 s and c0 = 3.5 ± 0.295 of thermal-induced compositional variance (T = 450 ºC). Note: 0.295 is half the Fe compositional variance estimated in section 6.2.2 since the equation works with the half-width of the lath (w).

Unfortunately, we cannot assume the same for Nb, since there is still a significant residual content in the IG α-phase laths (7.9 wt. %), while the Nb content is close to zero at the GBs. In this case, applying Equation 5 again, now with the half-width w = 360 nm, and choosing an arbitrary position inside the α-lath, x_i = 358 nm, we see that only extremely high Nb diffusion coefficients would cause Nb depletion in the core of the α-laths after such short annealing. To reach a residual Nb of 0.2 wt.%, diffusivity should be D_{Nb} (450 ºC) = $1.8.10^{-12}$, i.e., from 7 to 8 orders of magnitude greater than the volume diffusion. The sequence of simulations with several Nb coefficients is presented in Figure 6.16. A summary with the effective diffusion coefficients estimated based on Enomoto's model and our experimental data is presented in Table 6.3.

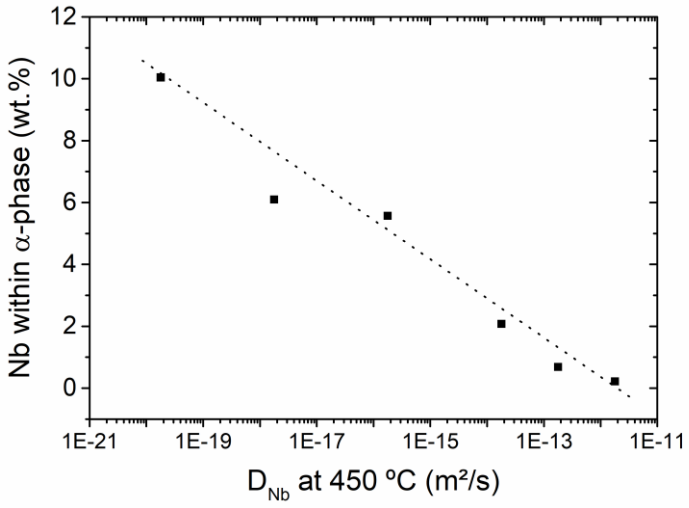

Figure 6.16 – Simulation of the residual Nb inside the GB α-phase laths vs the Nb diffusion coefficients in log scale. Values obtained with aid of Equation 6.1 assuming xi = 358 nm, w = 360 nm, t = 60 s and c0 = 11 ± 0.405 of thermal-induced compositional variance (T = 450 ºC). Note: 0.405 is half the Nb compositional variance estimated in section 6.2.2, since the equation works with the half-width of the lath (w).

We conclude the increase in the Nb diffusion coefficient must be enormous (8 orders of magnitude) to support the Nb depletion observed in the GB α-plates. On the opposite, in the case of Fe, an increase of three orders of magnitude (1600x) would be enough[12]. As stated

[12] It is worth reminding that the model did not encompass the cooling ramp from 750 ºC to 450 ºC, assuming a perfect isothermal experiment, and possibly overestimating the diffusion coefficients.

before, diffusion through GBs is a very complicated process. Therefore, it is hard to ascertain about how these solutes behave during the α-phase formation. With the data presented here, we can only infer that the divergence between Nb and Fe behaviors should be linked to the divergences between substitutional and interstitial diffusion. As the growth happens ledge-by-ledge, the substitutional diffusion on grain boundaries occurs in an orchestrated way, highly favored by the lattice discontinuities near the GBs, which have high interfacial energy and favor the ledges "jumps." On the opposite, Fe diffusion remains basically with the same mechanism (random walk), is slightly increased due to scarcely higher availability of interstitial sites. Curiously enough, Nb diffusion becomes even higher than Fe's through the GBs. To investigate this even further, we would have to look at the correlation factors between Nb and Fe, and how they dispute the neighborhood of the GB (see future works).

Table 6.3 – Effective diffusion coefficients at 450 ºC based on the (inverse) application of Equation 5 using experimental STEM-EDS data from Table 6.1.

Element, Experiment	**Diffusion coefficient (m^2/s)**	**Ratio to the D_{coef} from Smithells Book**
Nb, Intragnular α	5.10^{-20}	3
Nb, GB α	$1.8.10^{-12}$	10^8
Fe, Intragnular α	3.10^{-17}	20
Fe, GB α	$2.9.10^{-14}$	$3.2.10^4$

Concerning multicomponent alloys, it seems the diffusion coefficients always diverge from the binary data available in the literature. Furthermore, there is always initial solute segregation associated with the GBs for each element. Usually, the lower the element solubility in the phase-lattice, the higher the segregation [64,93]. We are currently in the process of investigating the GB in WQ samples with the aid of APT to see if a detectable solute rejection could occur during high-cooling rates (~100 ºC/s).

Also, in the light of these observations, if look back at the criteria for pseudospinodal (whose aim is to obtain an intragranular precipitation), the statement that says that "*the nominal composition of the parent phase lies close to the intersection, in the side where the free energy of the parent phase is lower than that of the product phase*" makes sense. If this is

not the case, even small solute segregation at GBs could alone trigger the GB α-phase precipitation as soon as the material reaches any temperature below β-*transus*.

6.6 Final remarks

Our study indicates that some aspects of the α phase formation are controversial in the TiNbFe system. Besides having a strong β-stabilizing effect, Fe accelerates the α phase formation during aging heat treatments while can also restrict α phase size. If a pseudospinodal mechanism were active in Ti-11Nb-3.5Fe alloy, a congruent-partitionless formation of α-phase inside the β grains in the first minute of aging would be expected. However, a significant α-phase formation at GBs was observed instead.

Experimental evidence presented in this chapter (especially in Figures 6.12 and 6.13 points to an independent α-phase formation at grain boundaries and inside the grains. However, given out methodology, it is impossible to establish which of these mechanisms take place at the earliest stage of aging. While allotriomorphic α nuclei are expected to form during the cooling ramp, intragranular α nuclei are expected at lower temperatures and could be linked to pseudoespinodal.

The formation of primary α is accelerated at the grain boundaries, given the high-diffusivity of GBs and the net energetic gain of remodeling these interfaces. The growth of α emanating from the GBs occurs massively, via a ledgewise growth, as a product of an autocatalytic α-phase formation. Such nucleation rate is high enough to impede primary GB alpha to advance to the interior of the grains, and the high density of product-α hinges the growth of other plates/laths in their vicinity. From a thermodynamic perspective - grain boundary segregations are prone to occur massively among Ti-Nb-Fe based alloys, given the co-segregation of Nb induced by Fe, which can trigger a preferential α-phase formation at the GBs. Knowledge of the enthalpies of mixing could be an important strategy to suppress large GB segregations.

Finally, Enomoto's model proved useful to describe the kinetics of α-phase growth in the Ti-Nb-Fe system. It follows that the use of similar, more refined methods such as transient models via ThermoCalc-DICTRA® and the growth velocity model proposed by Ackerman et al. (2018) could also be worth testing with the same experimental data set [53,148].

7. ADDING ZIRCONIUM TO THE TERNARY SYSTEM

As stated before, Zr additions could help to decrease the elastic modulus of Ti-Nb-Fe alloys by changing elastic anisotropy and suppressing the formation of ω phase. Still, what would be the optimal content of Zr that should be added to each alloy to destabilize ω-phase? This chapter is devoted to answering this question. However, given limitations regarding time and resources, a vast experimental matrix adding different contents of Zr to each one the six alloys explored in the previous chapters would be impractical. Therefore, we opted to pick only three alloys (Ti-11Nb-3.5Fe, Ti-19Nb-2.5Fe and Ti-27Nb-1.5Fe) and run try-outs, varying Zr additions from 4 to 13 wt.%, depending on the composition. These contents were arbitrarily determined based on alloys already available in the literature, such as TNTZ, TNZT and Ti-13Nb-13Zr.

7.1 Water-quenched and Furnace-cooled samples

To establish a frame of reference, we started analyzing samples subjected to ST-WQ and ST-FC, that could easily be compared to their parents from the ternary system (Chapters 3-5). It is worth reminding that the presence of ath-ω also causes meaningful alterations in the Vickers hardness, beyond changing the elastic modulus [8,94].

Vickers hardness for Ti-27Nb-1.5Fe, Ti-19Nb-2.5Fe and Ti-11Nb-3.5Fe with Zr additions are shown in Figure 7.1. Zr additions can significantly reduce Vickers hardness in comparison to the base alloy. For Ti-27Nb-1.5Fe and Ti-19Nb-2.5Fe, it seems the reduction reaches a threshold between 10-13 wt.% of Zr. Furthermore, the reduction in hardness for Ti-11Nb-3.5Fe based alloys is modest in comparison to the others. A compilation with the elastic modulus is presented alongside the hardness data (Figure 7.1d). In the ST-WQ condition, an elastic modulus close to 65 GPa was obtained for Ti-27Nb-1.5Fe with additions of 10 and 13 Zr (wt.%). These results can be considered promising relatively to other compositions with much higher Zr contents, such as Ti-25Nb-41Zr [149]. As for alloys based on Ti-19Nb-2.5Fe, the minimum modulus obtained was close to 70 GPa. For Ti-11Nb-3.5Fe based alloys, the reduction of hardness and modulus was negligible. For such Fe rich alloys, elastic modulus with and without Zr are close to 90 GPa. Regardless of the Zr additions, high quantities of Fe contribute to the reduction of the β-phase lattice parameter, thus limiting the elastic modulus

reduction obtained with reference to the base alloy. In general, the elastic modulus measurements are correlated to the Vickers hardness results. As for Ti-11Nb-3.5Fe-xZr, no significant changes in the elastic modulus were observed with the Zr addition; thus these data were not included in the graphs. Concerning the FC samples, for Ti-27Nb-1.5Fe, a significant drop in hardness and elastic modulus is observed with the Zr addition. It can be inferred that the Zr additions help to suppress the iso-ω phase previously formed in Ti-27Nb-1.5Fe (ternary) upon FC. Concerning Ti-19Nb-2.5Fe, hardness and elastic modulus are increased with Zr additions up to 10 wt.% and are only decreased with 13 wt. % (Figure 7.2). Zr additions help to increase the resistance of Ti-19Nb-2.5Fe samples by refining the α-phase precipitates found in this condition, in comparison to the ternary alloy, which commonly helps to improve mechanical strength.

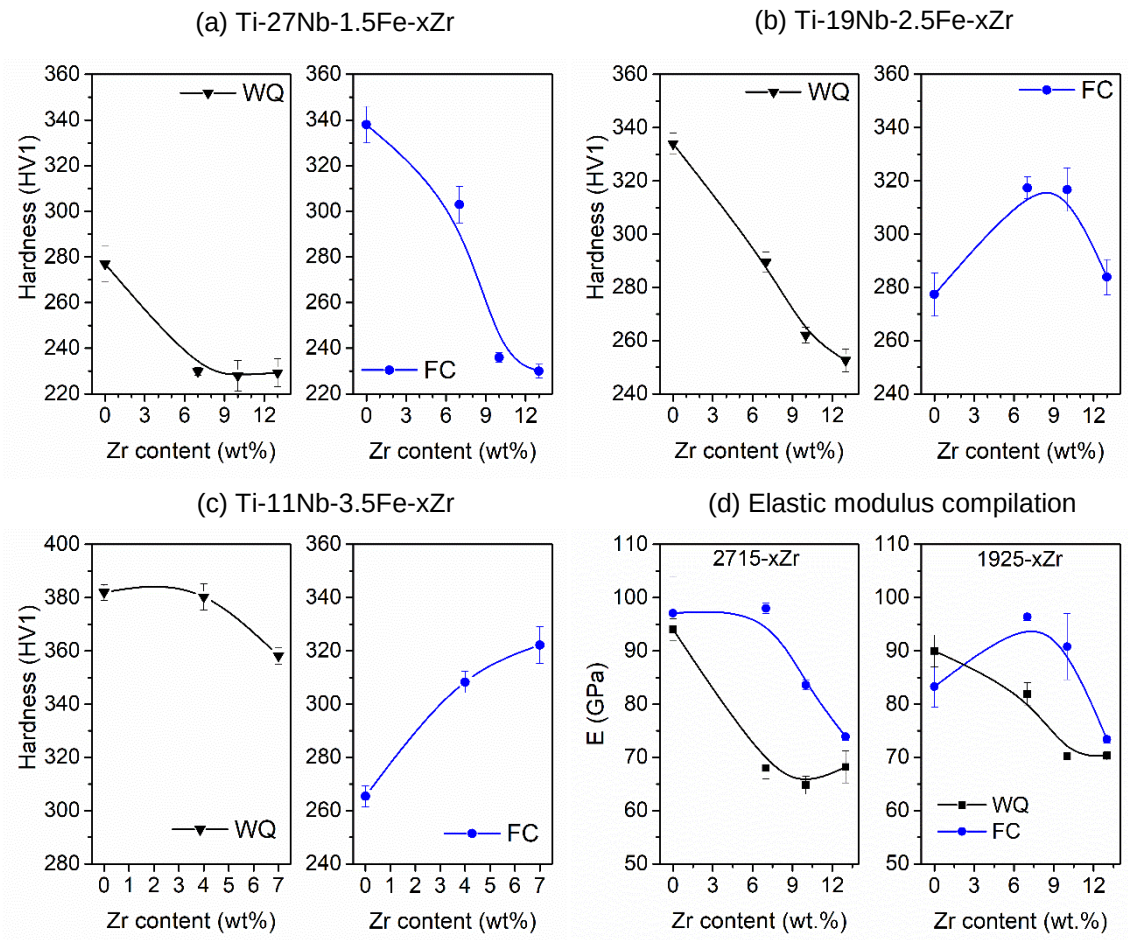

Figure 7.1 – Hardness as function of the Zr content for (a) Ti-27Nb-1.5Fe-xZr, (b) Ti-19Nb-2.5Fe-xZr and (c) Ti-11Nb-3.5Fe-xZr alloys, respectively. A compilation of the relevant elastic modulus measurements is presented in Figure 7.1d.

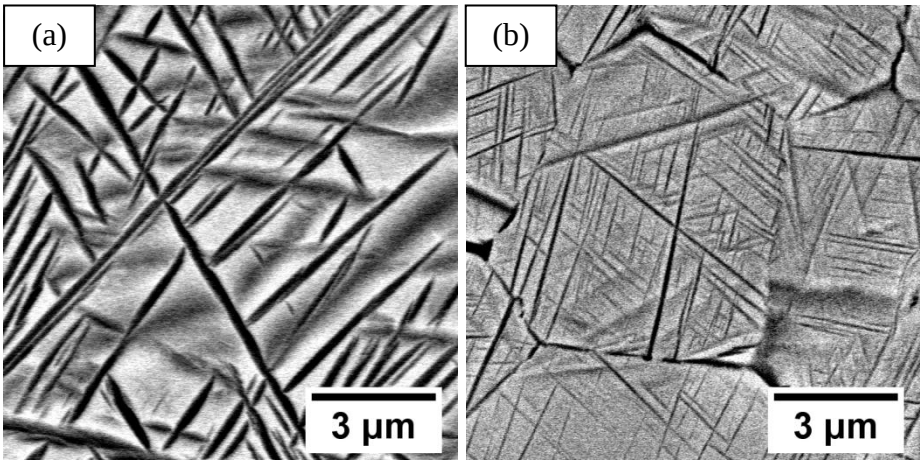

Figure 7.2 – Comparison between furnace-cooled (a) Ti-19Nb-2.5Fe and (b) Ti-19Nb-2.5Fe-7Zr alloys

The addition of Zr to the Ti-Nb-Fe ternary system has led to interesting divergences, comparing to the ternary system. The initial idea behind the Zr addition was to partially suppress the omega (ω) phase formation after water-quenching by a structural destabilization. XRD analyses were performed for all the experimental alloys after WQ or FC and are presented in Figure 7.3 and 7.4. As the microstructure have phases with a limited size, the analysis of conventional XRD data must be performed with caution. For the ST-WQ samples, the addition of Zr seems to efficiently hinder the formation of ω-phase, since no ω could be detected via XRD. Also, we noticed a moderate improvement in the cold formability in the quaternary system. However, ω-phase was still detected in Ti-11Nb-3.5Fe-xZr samples after ST-WQ (Figure 8.1) via TEM.

As for the FC condition, Nb-rich alloys presented β+ω microstructures while Fe rich alloys presented β+α microstructures, which is following previous results from the ternary system (Chapter 3). Among the ST-FC (furnace cooled) samples, one can see Zr slightly modifies the α-phase final volumetric fraction, from 56% to 50%, acting as a weak β-stabilizing element (Figure 7.5)

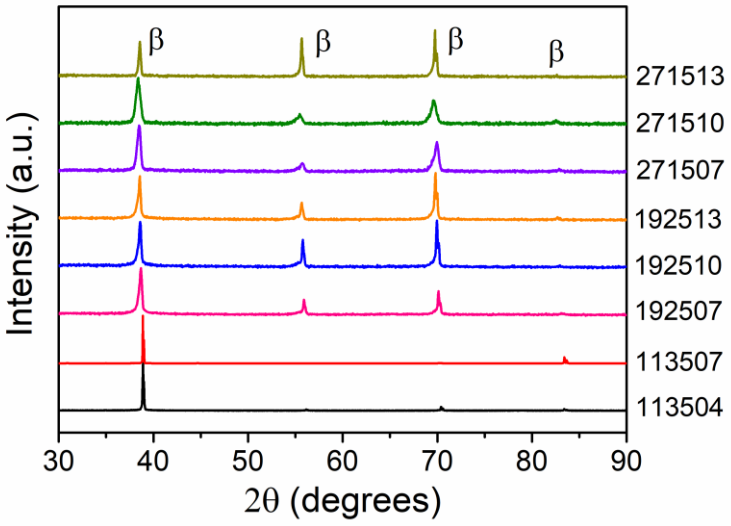

Figure 7.3 – XRD of the quaternary alloys after ST-WQ. The normalized intensity is displayed in arbitrary units.

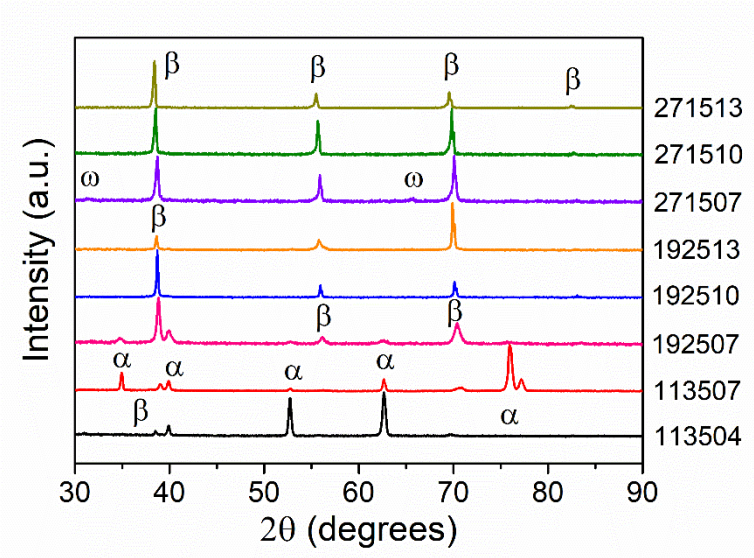

Figure 7.4 – XRD of the quaternary alloys after ST-FC. The normalized intensity is displayed in arbitrary units.

7.2 Aged-samples

The main alteration relatively to the ternary system, though, was noticed during the aging heat-treatments. Surprisingly, the α-phase precipitation on GBs was drastically reduced in the quaternary alloys. In Ti-11Nb-3.5Fe-7Zr, only approx. 5% of the grain boundaries

presented visible α-precipitates (Figure 5d). The cause for these observations is still unclear. Speculations are that the higher average grain size in this alloy could reduce the total grain boundary area, thus reducing the density of GB α-phase. Also, Zr could influence Fe's mobility (inside grains and on GB), due to the cocktail effect, commonly observed in compositionally complex alloys - i.e., the higher the number of elements, more sluggish is the diffusion. Near the GB, Zr atoms were found fairly distributed between phases (Figures 7.7f).

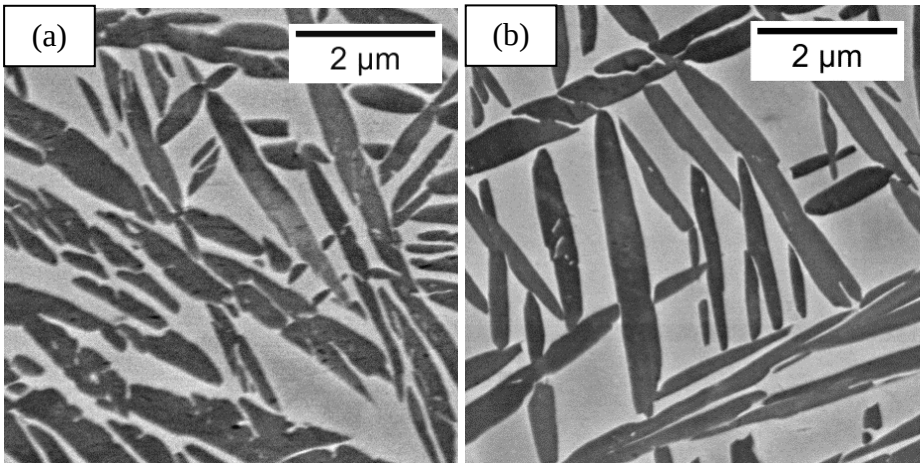

Figure 7.5 – Comparison between furnace-cooled (a) Ti-11Nb-3.5Fe and (b) Ti-11Nb-3.5Fe-7Zr alloys

By analyzing the samples subjected to long-aging heat treatments (Figure 7.6), Zr seems to restrain the α-phase laths lengthening, but not their thickening. The composition of the precipitates among ternary and quaternary alloys evolves similarly over time, even though Zr atoms were evenly distributed between both phases after the aging heat-treatments

7.3 Final remarks

Considerable insight has been gained about the addition of Zr to the Ti-Nb-Fe system. Taken together, the results implicate Zr can successfully hinder the formation of ω-phase upon WQ, increasing the cold-workability and reducing the elastic modulus. Also, Zr interferes with the formation of α-phase on grain-boundaries, which can be helpful to the

mechanical properties, especially increasing ductility. Zr additions have no significant role on the element partitioning between the β-matrix and the GB α-plates.

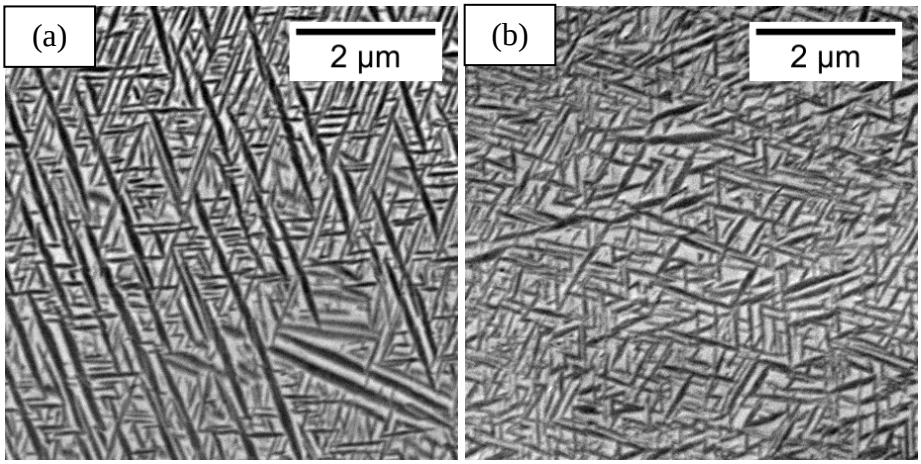

Figure 7.6 – Comparison between (a) Ti-11b-3.5Fe and (b) Ti-11Nb-3.5Fe-7Zr alloys step-quenched to 450 ºC for 30 min.

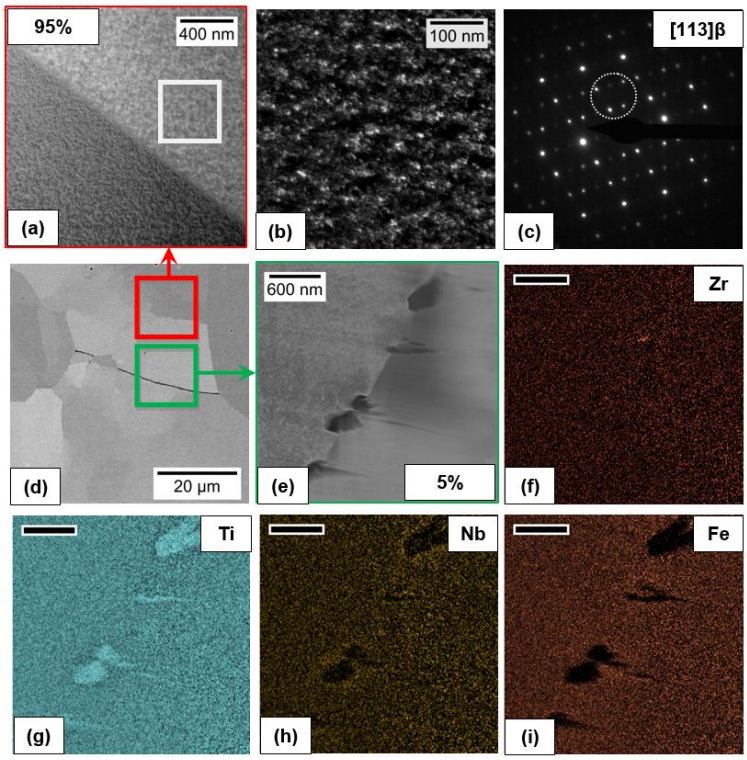

Figure 7.7 – Ti-11Nb-3.5Fe-7Zr - (a) HAADF, (b) DF and (c) SAD images of a GB without α-phase. SEM images are showing a GB α-phase. Image and compositional maps (e-i) of the selected GB.

8. MECHANICAL BEHAVIOR OF QUATERNARY ALLOYS

8.1 Mechanical behavior of quaternary alloys rich in Fe

As stated before, an open challenge on structural biomaterials is to obtain low-cost Ti-alloys with high elastic admissible strength (the ratio of yield strength to elastic modulus). To reach this goal, we designed and characterized three quaternary alloys relatively rich in Fe[13], that were based on Ti-11Nb-3.5Fe and Ti-19Nb-2.5Fe: Ti-11Nb-3.5Fe-7Zr, Ti-19Nb-2.5Fe-10Zr, and Ti-19Nb-2.5Fe-6Sn (wt. %). One important aspect of this work is to compare the influence of either Zr or Sn on the microstructure of Ti-19Nb-2.5Fe as an isolated problem.

As usual, we start with the ST-WQ samples. The average grain-size of Ti-19Nb-2.5Fe-10Zr and Ti-19Nb- 2.5Fe-6Sn were estimated at around 70 μm, while the grains of Ti-11Nb-3.5Fe-7Zr reached 100 μm, on average, corresponding to Fig. 8.1a– c. Given the three alloys possess grains with a size of the same order of magnitude, this should not be considered as the main factor while making distinctions between their mechanical properties. Analogously to the ternary system, α″ phase was not detected among quaternary alloys at this condition, since Fe additions play an important role in avoiding the formation of α″ phase [123]. In the case of Ti-19Nb-2.5Fe-10Zr, the combined addition of Nb, Fe, and Zr to Ti allowed the retention of a full β-phase microstructure after ST-WQ. For the other two experimental alloys, athermal-ω (ω-ath) was detected, as can be seen in selected-area diffraction (SAD) patterns and the TEM images displayed in Figure 8.1, even though the combined presence of Fe and Zr can often destabilize ω [150]. Therefore, we infer that the ω-suppression capabilities of 6Sn are not the same as 10Zr (wt%). However, when comparing the ω-phase detected among the experimental alloys with their respective ternary alloys, quaternary additions with either Sn or Zr reduce the volumetric fraction of ω-phase by some content [20,58,151]. The same happens for alloys with a similar Mo equivalent – e.g., comparing Ti-19Nb-2.5Fe with and without quaternary additions.

Tensile tests performed at the ST-WQ condition are presented in Figure 8.2. The similarities of the stress-strain curves of the Ti-19Nb-2.5Fe-6Sn (wt%) and TNZT gum metals are evident. Just after the specimens start yielding, a drop in the resistance is observed, and the stress reaches a plateau, which could be linked to stress-induced phase-transformations,

[13] We assumed "relatively rich in Fe" alloys to have a Nb/Fe (atomic) ratio inferior than 5, according to Table 4.1.

such as α′ phase [152], α″ phase [153], stress-induced ω-phase and deformation twins. According to Koli et al. (2015), deformation mechanisms of Ti alloys vary widely, even within a specific range of solute content [154]. Preliminary XRD data collected on the fractured edges of the tensile test specimens after testing indicate that the main deformation mechanism among the experimental alloys might be twinning and dislocation slip since no stress-induced phases were detected (see Figure 8.3). Despite these observations, the influence of ωath and the grain-size on the stress-induced formation of α″-phase requires further studies [155].

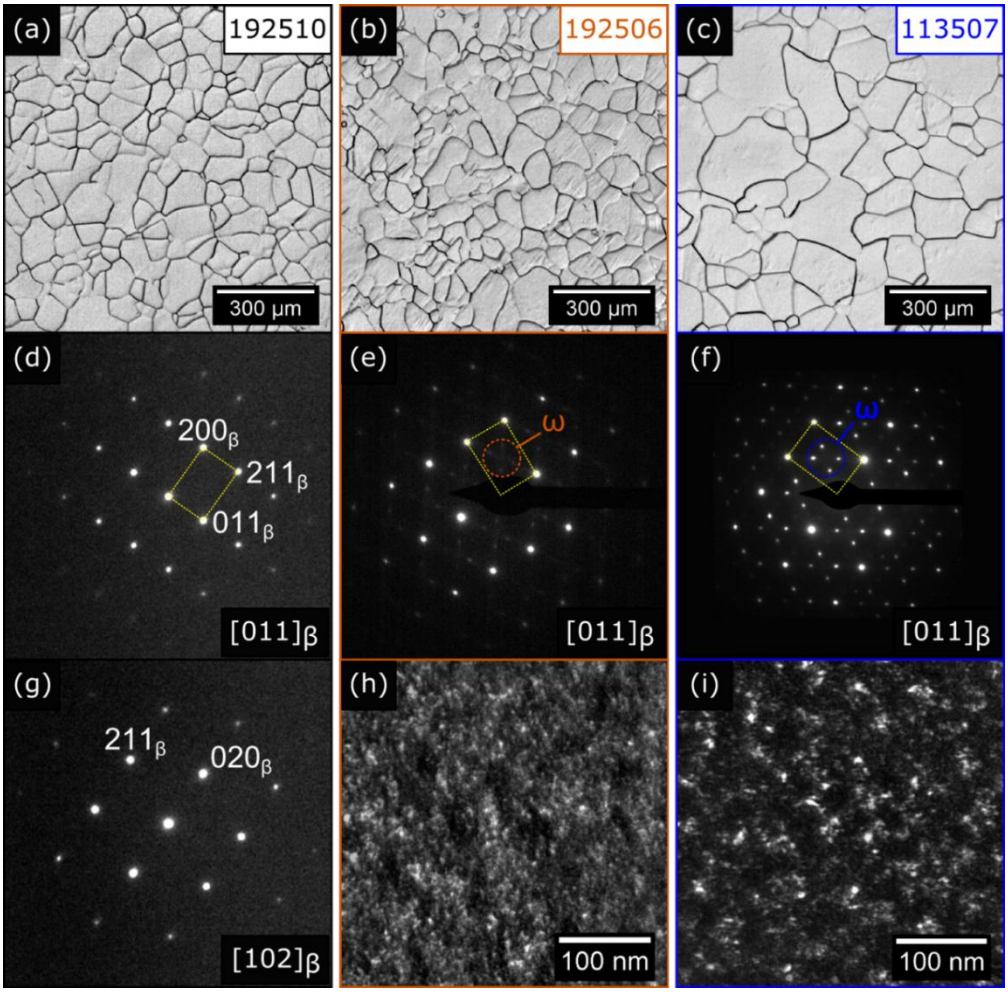

Figure 8.1 – Optical micrographs of the solution-treated and water-quenched (ST-WQ) quaternary alloys: (a) Ti-19Nb-2.5Fe-g. Zr, (b) Ti-19Nb-2.5Fe-6Sn and (c) Ti-11Nb-3.5Fe-7Zr. Selected-area diffraction patterns (SAD, d, e, f) and dark field images showing the athermal omega-phase (h, i) at the same condition. An additional SAD image is presented for Ti-19Nb-2.5Fe-10Zr (g) since it has a full beta-structure at this condition. Ti-19Nb-2.5Fe-6Sn and Ti-11Nb-3.5Fe-7Zr dark-field images are presented in (h) and (i), respectively.

The strain-hardening effect among Ti-Nb-Fe-Sn (TNFS) samples seems negligible. The ductility of Ti-19Nb-2.5Fe-6Sn is slightly superior to TNZT, with an average strain of 31%, while TNZT-O gets to approx. 20% before failure. According to the literature, at this condition, TNZT-O presents a great combination of yield strength and elastic modulus, 976MPa and 66GPa, respectively, thus resulting in an elastic admissible strain (EAS) of 1.48 [5]. Even though a relatively low EAS obtained for Ti-19Nb-2.5Fe-6Sn at this condition (1.09), the EAS obtained for Ti-19Nb-2.5Fe-10Zr (wt%), on the opposite, is close to that of TNZT-O - with 1027 MPa of yield strength and 69 GPa of elastic modulus, as can be seen in Table 8.1. According to Abdel-Hady et al., Zr has a high bond-order (Bo) comparatively to Ti - thus, alloying with Zr implies a reduction of the elastic modulus of β-Ti [58]. As for shape-memory alloys, some authors suggest the optimal Zr/Nb ratio of 0.3 [156]. While Ti-19Nb-2.5Fe-10Zr has a Zr/Nb ratio close to 0.5, it would be worth analyzing its shape-memory behavior at the WQ condition, given the mechanical behavior reported here (Table 8.2).

Table 8.1 – Electronic parameters, hardness and elastic modulus of the experimental alloys. Ternary Ti-11Nb-3.5Fe and Ti-19Nb-2.5Fe were included for comparison.

Alloy	Bo	Md (eV)	e/a	Mo [eq]	Hardness (HV1)	E (GPa)*
1135	2.804	2.399	4.19	11.83	382 ± 3	97 ± 1
113507	2.817	2.416	4.19	11.83	358 ± 3	88 ± 3
1925	2.820	2.409	4.20	11.57	334 ± 4	90 ± 3
192506	2.807	2.398	4.21	11.57	260 ± 9	78 ± 1
192510	2.840	2.437	4.21	11.57	267 ± 3	70 ± 1

*Obtained with the pulse-echo ultrasound technique

To this point, we concluded that the experimental alloys have similar properties to the TNZT system, and quaternary additions benefit the TNF alloys at the ST-WQ condition by increasing the mechanical strength while reducing the elastic modulus. As can be seen in the fracture surfaces presented in Figure 8.3, all ST-WQ samples showed a relatively ductile behavior, presenting a quasi-cleavage fracture mode [85,112,129]. The greater proportion of cleavage facets, which are associated with a brittle behavior, is observed in Ti-11Nb-3.5Fe-7Zr, probably due to the higher ω-ath volumetric fraction (Fig. 8.1) and its elevated Fe content.

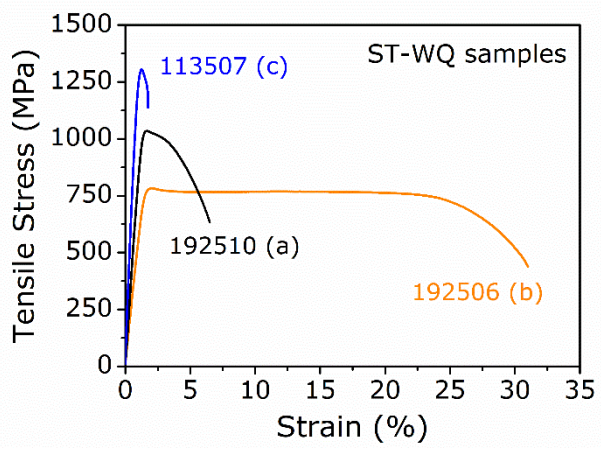

Figure 8.2 – Stress-strain curves for the experimental alloys at the ST-WQ condition. The plastic deformation does not cause work-hardening among Ti-19Nb-2.5Fe-6Sn (b) samples.

Table 8.2 – Compilation of the mechanical properties obtained through tensile tests

Alloy	Condition	Elastic modulus (GPa)	Yield Strength (MPa)	EAS* (%)	Elongation (%)
113507	**WQ**	90 ± 2	1011 ± 17	1.12	4 ± 1
	Aged	93 ± 2	1184 ± 33	1.27	1 ± 1
192506	**WQ**	71 ± 2	765 ± 10	1.08	31 ± 5
	Aged	98 ± 3	1261 ± 41	1.29	6 ± 1
192510	**WQ**	69 ± 1	1027 ± 33	1.49	8 ± 2
	Aged	97 ± 3	1132 ± 18	1.17	3 ± 1

*Elastic admissible strain

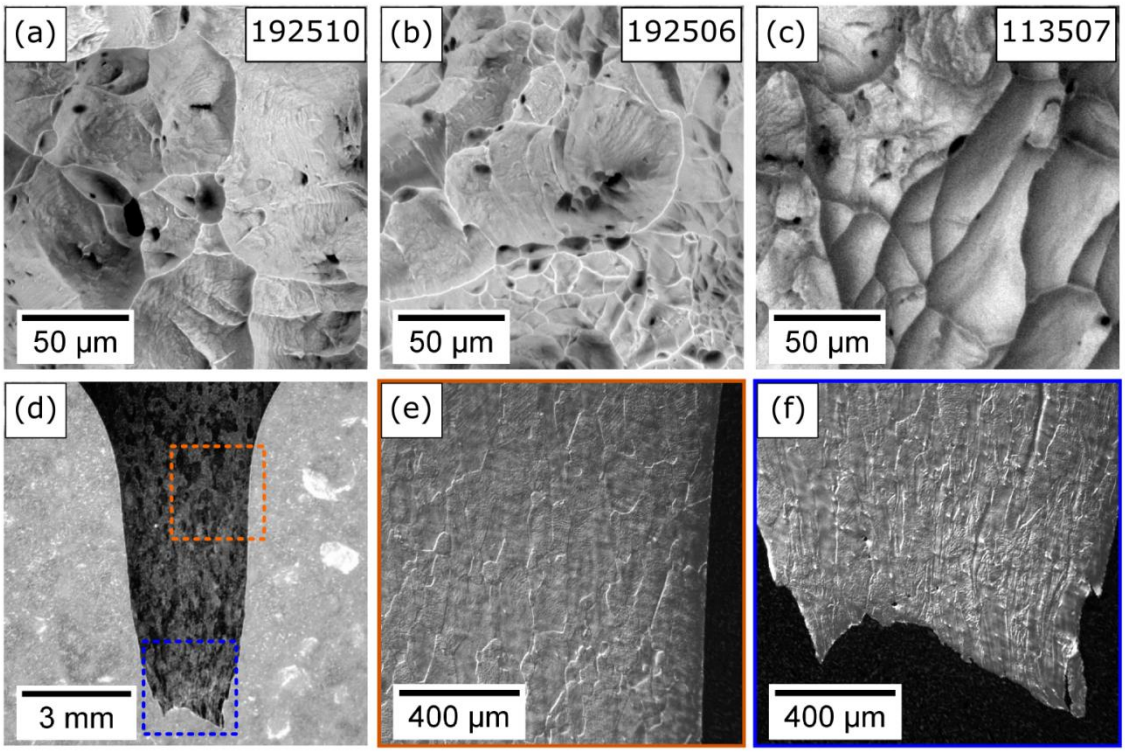

Figure 8.3 – Fractography of alloys (a) Ti-19Nb-2.5Fe-10Zr (b) Ti-19Nb-2.5Fe-6Sn and (c) Ti-11Nb-3.5Fe-7Zr alloy at the ST-WQ condition presenting a quasi-cleavage fracture mode. Transversal analysis of the Ti-19Nb-2.5Fe-6Sn showing the increase of twin boundaries near the failure (d-f).

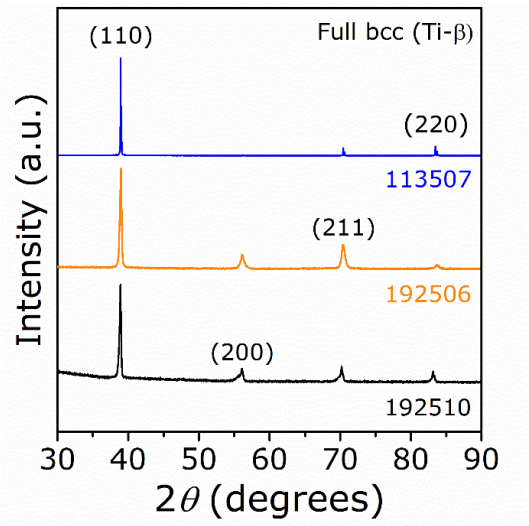

Figure 8.4 – X-ray diffraction of the fractured edges of the tensile test specimens (after testing) at the ST-WQ condition. Only the β-phase (bcc) was detected.

8.2.1 Isothermally-aged samples

Previous works have shown that Fe largely improves the mechanical strength of Ti-Nb-Fe alloys due to the reinforcement of the β-phase matrix via solid solution [69,109,111]. However, to achieve even higher strength, controlled precipitation of alpha (α) through aging heat treatments could be employed [157]. Since the size and distribution ofα-laths typically vary depending on the aging heat-treatments [8], trials with three different times (30 min, 3 h, and 12 h) were conducted, and we selected the microstructure with the finest and most disperse distribution of α-phase for each alloy to perform the tensile tests. That is - 12 h for the Ti-19Nb-2.5Fe based alloys and 30 min for the Ti- 11Nb-3.5Fe-7Zr alloy. The goal was to observe a net increase in the elastic admissible strain after the heat-treatment. Step-quench heat-treatments were selected instead of classical quench-and-aging treatments to avoid the formation of ω-phase at lower temperatures, e.g., while reheating the microstructure [94,158]. The aging temperature of 450 °C was selected based on our previous DSC experiments with Ti-19Nb- 2.5Fe ternary alloys (Chapter 3).

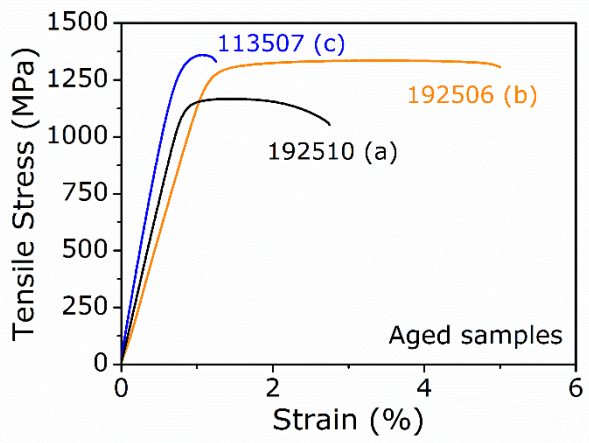

Figure 8.5 – Stress-strain curves for the heat-treated alloys, (a) Ti-19Nb-2.5Fe-10Zr, (b) Ti-19Nb-2.5Fe-6Sn and (c) Ti-11Nb-3.5Fe-7Zr (wt.%).

As shown in Figure 8.5, an increase in yield strength was observed after aging for all experimental alloys when compared to the ST condition. Ti-19Nb-2.5Fe-6Sn presented a remarkable increase in yield strength, from 765 MPa to 1261 MPa. Among Zr-based alloys, yield strength was increased by roughly 10%. In other ways, it is known that by strengthening the βmatrix through precipitation-hardening, the elastic modulus will inevitably be increased,

which is undesirable [3]. The elastic modulus of Ti-19Nb-2.5Fe-10Zr and Ti-19Nb-2.5Fe-6Sn were increased by approximately 30 GPa as part of the heat-treatment performed. These significant changes in mechanical behavior can be ascribed to microstructural alterations arising from aging, which will be discussed in more detail in the next paragraphs. To some extent, the increase in modulus is also associated with the increase in oxygen content to approx. 0.30 wt% during the hot swaging processing, which is a required step in the fabrication of the tensile test specimens. The composition of the experimental alloys including O and N contents are shown in Section 2. Regarding the fracture surfaces, we could identify fewer dimples, compared to the WQ samples, but the typical transgranular fracture mode is still predominant (Fig. 8.6).

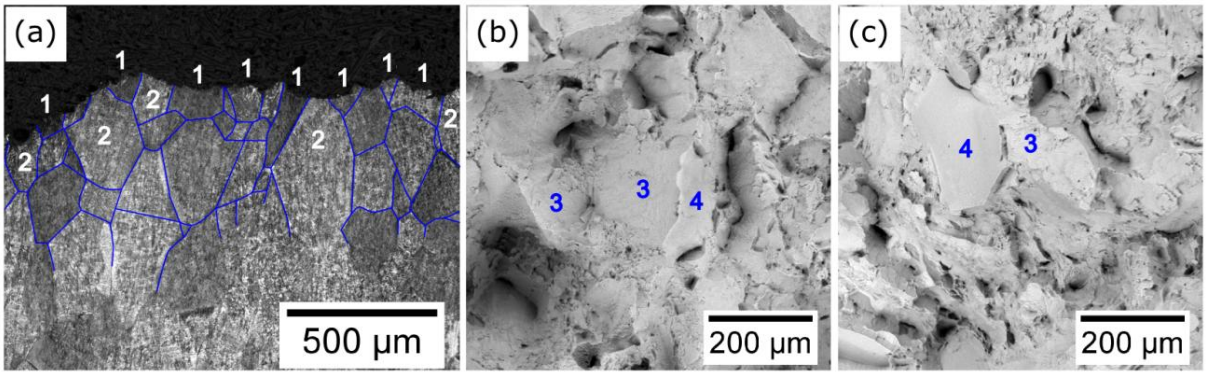

Figure 8.6 – Transversal (optical) and top-view fractography (a, b) of the Ti-19Nb-2.5Fe-6Sn and top-view (c) of the Ti-11Nb-3.5Fe-7Zr aged samples. Some features are indicated as (1) transgranular fracture, (2) intergranular fracture, (3) mixed fracture and (4) cleavage facets, respectively.

As seen in the scanning electron microscopy (SEM) images presented in Fig. 8.7, the aging heat-treatment was successful in obtaining fine and disperse α-laths to reinforce the β-matrix for the three experimental alloys. The laths are distributed, acting as an effective barrier to dislocations [8], and we did not observe a massive of α-phase at the grain boundaries, which could impair ductility [85]. With the assistance of ImageJ2 [159], we estimated the number of α-laths per area in each SEM image displayed in Fig. 8.7. For Ti-19Nb-2.5Fe-10Zr, there are approximately 7 laths/µm^2, while for Ti-19Nb-2.5Fe-6Sn and Ti-11Nb-3.5Fe-7Zr, there are 25 laths/µm^2, corresponding to Fig. 8.7c and d. The distributions of

Ti-19Nb-2.5Fe-6Sn and Ti-11Nb-3.5Fe-7Zr are similar, and both are finer than the Ti-19Nb-2.5Fe-10Zr counterpart. According to Zheng et al., they can be considered to be super-refined [43]. Finer α-phase distributions usually increase the mechanical strength of Ti-alloys [160]; thus, the high strength exhibited by aged Ti-19Nb-2.5Fe-6Sn is certainly related to the regular and restricted growth of α-laths in the selected aging condition. On the other hand, despite its α-phase density, the excess of Fe in Ti-11Nb-3.5Fe-7Zr β-matrix might have impaired the alloys ductility, comparing to the Ti-19Nb-2.5Fe based alloys [111].

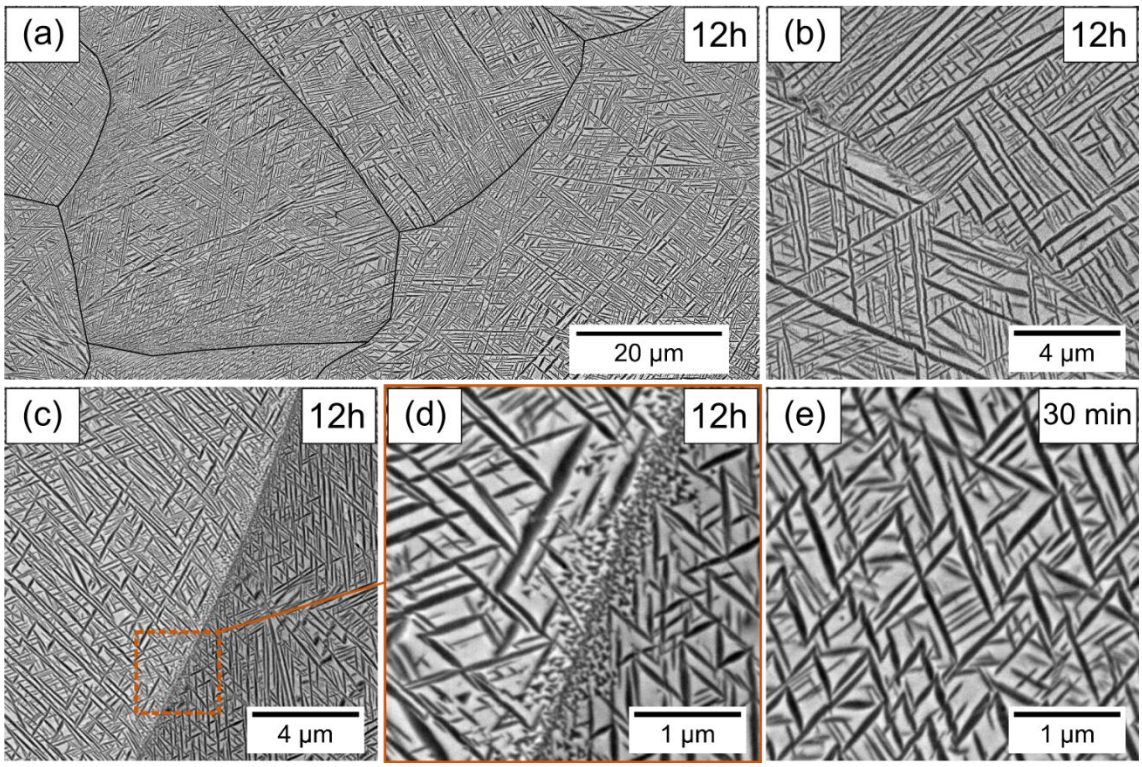

Figure 8.7 – SEM backscattered electrons (BSE) images of the experimental alloys after aging: (a) low-magnification of Ti-19Nb-2.5Fe-10Zr, grain boundaries were highlighted with coarse black lines; (b) Ti-19Nb-2.5Fe-10Zr, (c, d) Ti-19Nb-2.5Fe-6Sn and (e) Ti-11Nb-3.5Fe-7Zr alloy. The aging time is displayed at the right, upper corner.

As stated in Chapters 4-6, the rejection of β-stabilizing Nb and Fe from the α-phase was expected. Additionally, a negligible partitioning of Sn between β-matrix and α-phase laths was observed among Ti-19Nb-2.5Fe-6Sn samples, as shown in Fig. 8.8. Based on thermodynamic equilibrium assessments via ThermoCalc® (Table 8.3), a homogeneous

distribution of Sn between matrix and precipitates was not expected. Sn should be rejected from the β-phase to the α-laths. However, the opposite trend has been reported while subjecting Ti-Nb-Sn and Ti-Mo-Sn alloys to prolonged aging heat-treatments [19,161], with Sn being slightly rejected to the β-phase, instead. In this respect, it seems the Ti-Sn interactions are not well described via ThermoCalc®, and since the results are controversial, further assessments of the Ti-Fe-Sn system are needed to refine these calculations. The migration of Sn to the β-phase requires time, given Sn low diffusivity in both β and α-phases [162,163]. With that said, 12 h might be not enough time to reach the predicted equilibrium compositions, in this case.

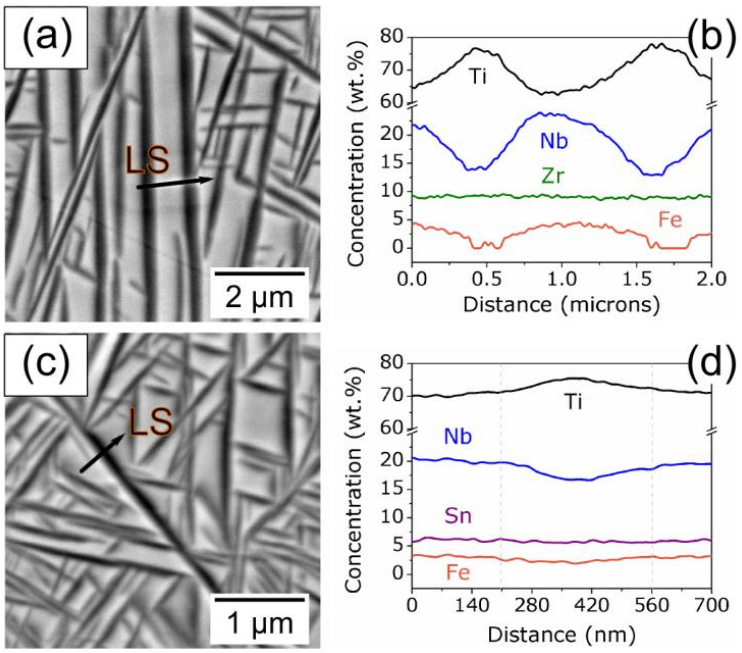

Figure 8.8 – Line scans performed via scanning electron microscopy (SEM), energy dispersive X-ray spectroscopy (EDS) of Ti-19Nb-2.5Fe-10Zr (a-b) and Ti-19Nb-2.5Fe-6Sn (c-d) aged at 450 °C for 12h. A marginal partition of both Zr (b) and Sn (d) is observed between matrix and precipitates.

Despite being considered a neutral alloying element, earlier authors suggested that aging Ti-Nb-Zr alloys could induce Zr to migrate to the β-phase matrix, working as a β stabilizer element [60]. However, a Zr partition could not be observed after aging Ti-19Nb-2.5Fe-10Zr for 12 h (Fig. 8.8b) and Ti-11Nb-3.5Fe-7Zr for 30 min (Fig. 8.8). ThermoCalc® predictions foresee that Zr should be equally distributed between matrix and precipitates in

Ti-19Nb-2.5Fe-10Zr (Table 8.3), which corroborates with our results. As for Ti-11Nb-3.5Fe-7Zr, Zr should be slightly concentrated at the β-phase. However, as we identified the coarsening of the α-precipitates occurring quickly in Ti-11Nb-3.5Fe-7Zr alloy, the heat-treatment time had to be limited to 30 min among these samples to avoid over-aging, and we believe the system did not have the time to achieve equilibrium compositions. In other ways, the assessment for the Ti-Nb-Fe-Zr system seems accurate.

By comparing Ti-19Nb-2.5Fe-10Zr with Ti-19Nb-2.5Fe-6Sn, we conclude that both Zr and Sn contribute to reducing the elastic modulus comparing to the Ti-Nb-Fe ternary system. The advantage of adding Zr is a stronger effect on reducing the elastic modulus in the ST-WQ condition, while Sn allows higher yield-strengths and more refined α-phase distributions, limiting α-phase coarsening during aging. Therefore, the co-addition of Zr and Sn seems a promising strategy in developing age-hardening gum-type alloys [20,21,164,165].

Table 8.3 – Equilibrium compositions at 450 °C predicted by ThermoCalc using the TCT1 thermodynamic database (2018).

Alloy (wt.%)	**Phases***	**Composition (wt.%)**			
		Ti	**Nb**	**Fe**	**Zr or Sn**
Ti-11Nb-3.5Fe-7Zr	β (bcc)	60.3	22.9	8.6	8.2
	α (hcp)	91.0	2.8	< 0.01	6.1
Ti-19Nb-2.5Fe-6Sn	β (bcc)	46.1	47.4	6.5	< 0.01
	α (hcp)	90.0	1.3	< 0.01	9.7
Ti-19Nb-2.5Fe-10Zr	β (bcc)	52.4	32.9	4.7	10.0
	α (hcp)	86.9	3.1	< 0.01	10.0

*Only disordered BCCs were included in the calculation.

8.2.2. Grain boundary segregations in TNFZ and TNFS systems

Once the importance of enthalpy of mixing in the TNF system has been exposed in Chapter 6, section 6.3, this paragraph will approach the TNFZ and TNFS quaternary systems in a similar way. The enthalpy of mixing of Fe-Zr is -35 J/mol, which is close to the reported values for Ti-Fe (-31 J/mol) and Nb-Fe (-22 J/mol). In this way, drastic changes in the segregation behavior are not expected after adding Zr to the ternary Ti-Nb-Fe system. By

doing this, Zr will only substitute an element with a similar enthalpy of mixing to the others. Analogously, little difference was observed in our experiments, even with high Fe contents. To exemplify, alloys Ti-11Nb-3.5Fe and Ti-11Nb-3.5Fe-7Zr present an almost identical microstructural evolution while subjected to annealing heat-treatments. On the opposite, the enthalpy of mixing of Fe-Sn is highly elevated, +92 J/mol. This number indicates that Sn will avoid to neighbor Fe at all (energetic) costs. However, the enthalpies of mixing of Nb-Fe and Nb-Sn are both negative, -22 e -25 J/mol, respectively, which indicates that both Fe and Sn must compete for the Nb neighborhood. In this manner, it seems that Sn restricts the co-segregation of Nb induced by Fe observed in the other alloy-systems, potentially altering the segregation mechanisms and the α-phase precipitation among Ti-Nb-Fe-Sn alloys. If we look at the α-phase formation at GBs in the Ti-19Nb-2.5Fe-6Sn, we will observe almost no precipitation at the GBs, what assures a high ductility after annealing to TNFS alloys [166]. That`s why Ti-19Nb-2.5Fe-6Sn responds better than any TNFZ alloy to aging heat-treatments.

8.2.3. Diffusion of the quaternary element

Now we will discuss the sluggish solute-diffusion observed among the TNFS aged samples, displayed in Fig. 8.8d. Previous studies showed that nearest-neighbor monovacancy jumps in the ⟨111⟩β direction are responsible for the diffusivity in bcc-structures over a large range of temperatures [93]. According to Neumann et al. (2001), Ti, Zr and Hf-based alloys are vulnerable to lattice instabilities in the ⟨111⟩β direction, which result in a drastic softening of ⟨111⟩ and ⟨110⟩ phonon-modes, that hence cause a decrease of the vacancy-migration energy and thus an enhanced diffusivity [162]. Based on our results, it could be inferred that Sn partially suppresses the lattice instabilities along the ⟨111⟩β direction. A consequence of that is the partial suppression of the (111)β collapse (to form ω-phase) observed in the WQ-condition (Figure 8.1d-i).

On the other hand, since Zr additions also suppressed the ω-phase, this cannot be the main factor influencing the Nb and Fe diffusion in the presence of a quaternary element. If that were the case, Ti-Nb-Fe-Zr (TNFZ) and TNFS would display an analogous behavior regarding diffusion – which is not the case (compare Figs. 8.8b, 8.8d and 8.9d). Therefore, the

barriers to Nb and Fe diffusions - which are particular to the Ti-Nb-Fe-Sn system - must be related to the presence of Sn atoms in the bcc-solid solution.

Sn has been known as a slow-diffuser in α and β Ti-alloys. Although some authors take account of Sn large metallic radius on its diffusivity, this should not play a decisive role regarding substitutional solutes that migrate via vacancies [162]. The diffusion coefficients of substitutional solutes linearly depend on correlation factors (CFs) - i.e. the correlation between two successive solute-vacancy exchanges. However, in binary alloys, the influence of CFs on Sn diffusion is negligible. As a result, the CFs on Sn impurity-diffusion in β-Ti has been often described by a pure mass-effect [167]. In respect to this point, we can only infer that the CFs in a multi-component system diverges from the binaries correlation factors available in the literature [168]. On top of that, CFs must depend on secondary interactions between Sn and the other alloying elements in this system: Nb and Fe.

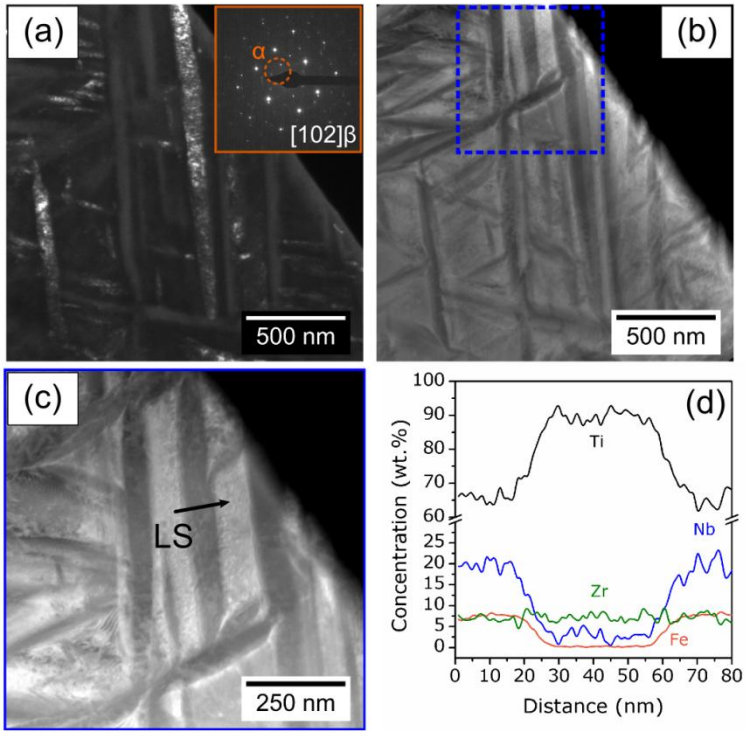

Figure 8.9 – TEM-images of Ti-11Nb-3.5Fe-7Zr aged at 450 °C for 30 min: (a) dark-field showing the alpha-precipitates through the [102]β zone axis, (b) HAADF image of the same region, (c) HAADF showing the region analyzed via EDS and finally (d) the compositional profile of the marked α-lath.

According to a recent study with the Ti-Nb-Sn system, small Sn additions create an energetically favorable configuration of Ti-Sn first- neighboring atoms, with a mixed Ti-Nb neighborhood [169]. We believe these Ti-Sn anti-bonding sites may influence the vacancy-migration energy and therefore the solute diffusion in our system. After all, further studies on the solute-vacancy binding energies and the chemical bonding characteristics of the Ti-Nb-Fe-Sn quaternary system are needed to reach a better understanding of the role of Sn on the mechanisms of diffusion.

8.3 Mechanical behavior of quaternary alloys rich in Nb

This section is dedicated to the quaternary alloys with higher Nb-content, i.e., Ti-23Nb-2.0Fe-10Zr, Ti-27Nb-1.5Fe-10Zr and Ti-31Nb-1.0Fe-10Zr. These alloys were designed with the hope that elevated Nb/Fe ratios (high Nb contents) could present a reduced elastic modulus in respect to the previous compositions, which had significant Fe amounts.

As a preliminary analysis, XRD data was obtained from the samples after solution-treatment followed by WQ (ST-WQ). One more time, WQ samples presented a full β-structure (Figure 8.10a). According to TEM analysis presented in Chapter 7, the addition of 10 wt.% of Zr to the ternary alloys Ti-19Nb-2.5Fe and Ti-27Nb-1.5Fe fully suppresses athermal ω-phase formation upon quenching. As Ti-23Nb-2.0Fe and Ti-31Nb-1.0Fe also have appreciable amounts of Nb, it could be inferred that ω-ath would also be suppressed upon the same addition. Figure 8.10b shows the diffractograms obtained from samples subjected to solution treatment followed by a step-quench to 450 ºC for 12h. Data points to a successful strategy in obtaining fine and dispersed α-precipitates through the β matrix without detectable ω-phase formation. The temperature of 450 ºC - which is above ω-*solvus* for both Ti-19Nb-2.5F-10Zr and Ti-27Nb-1.5Fe-10Zr - was chosen based on the previous discussion, especially concerning the DSC results presented in Chapter 4.

The microstructures of the WQ and aged samples are further detailed in Figure 8.11. As can be seen in the optical micrographs presented in Fig. 8.11a-c, WQ samples present only β grains, with a wide size distribution, due to the mechanical processing and quick recrystallization performed before the characterization. Although it appears Ti-23Nb-2.0Fe-10Zr has greater grains than the others, it is not possible to correlate grain size with the

composition, since the grain size depends on the region from which the image was taken. At the center of the plates/bars, the grains can be 5-10 times greater than on the edges. As for the aged samples (Fig. 8.11d-f), one can observe fine and dispersed α-phase, without much development of the precipitates at the grain boundaries, which is beneficial to ductility. As the images were recorded with the aid of a BSE detector, it can be inferred that Nb has been concentrated in the β-phase (brighter), as expected for such long heat-treatments.

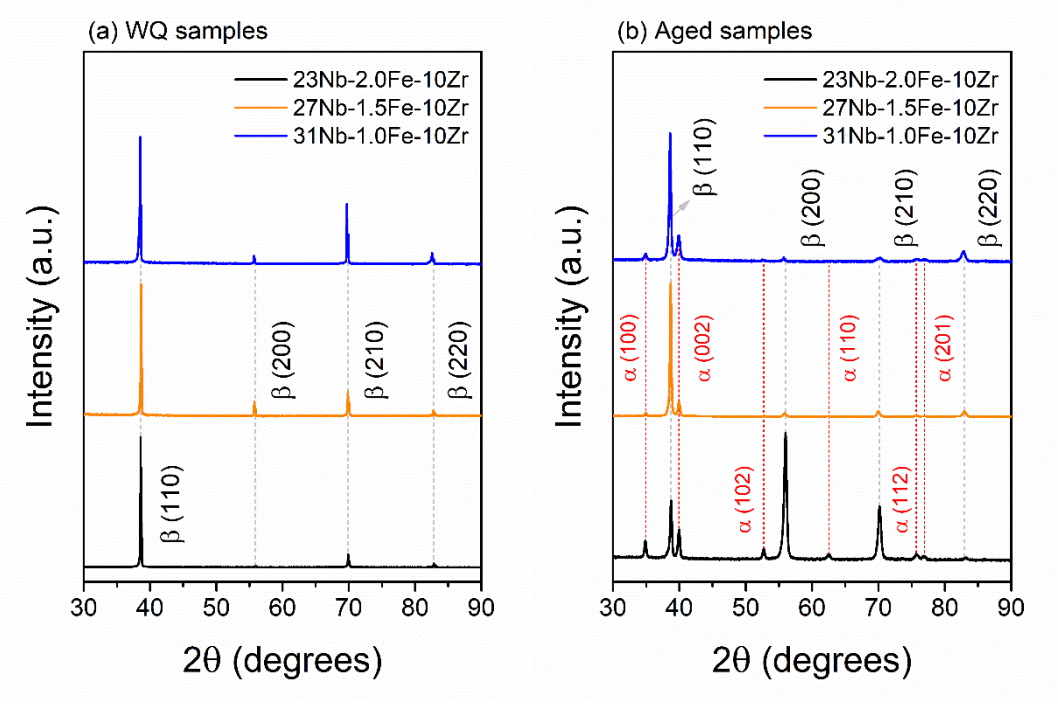

Figure 8.10 – XRD data on the (a) ST-WQ and (b) aged conditions.

Tensile tests presented at the WQ and aged conditions are presented in Figure 8.12a and 8.12b, respectively. As expected, the lower Nb/Fe ratio – i.e., a higher Fe content – in Ti-23Nb-2.0Fe-10Zr leads to overall higher yield strengths. On the other hand, elevated Nb contents lead to an improved ductility. Ti-31Nb-1.0Fe-10Zr reached an average elongation at failure of 15 ± 6 %, the higher strain among the three High-Nb experimental alloys, but still lower than Ti-19Nb-2.5Fe-6Sn. Concerning the heat-treated specimens, Ti-23Nb-2.0Fe-10Zr performed best in response to aging, with an average yield strength of 980 ± 62 MPa. A compilation of the mechanical properties obtained in this study is presented in Table 8.4. Despite the sound results reported in this section, neither of the high-Nb alloys performed as

good as the Ti-19Nb-2.5Fe-10Zr with respect to the mechanical properties. In other words, Ti-19Nb-2.5Fe-10Zr seems to present an optimal trade-off between mechanical strength and low elastic modulus, reaching a singular elastic admissible strain.

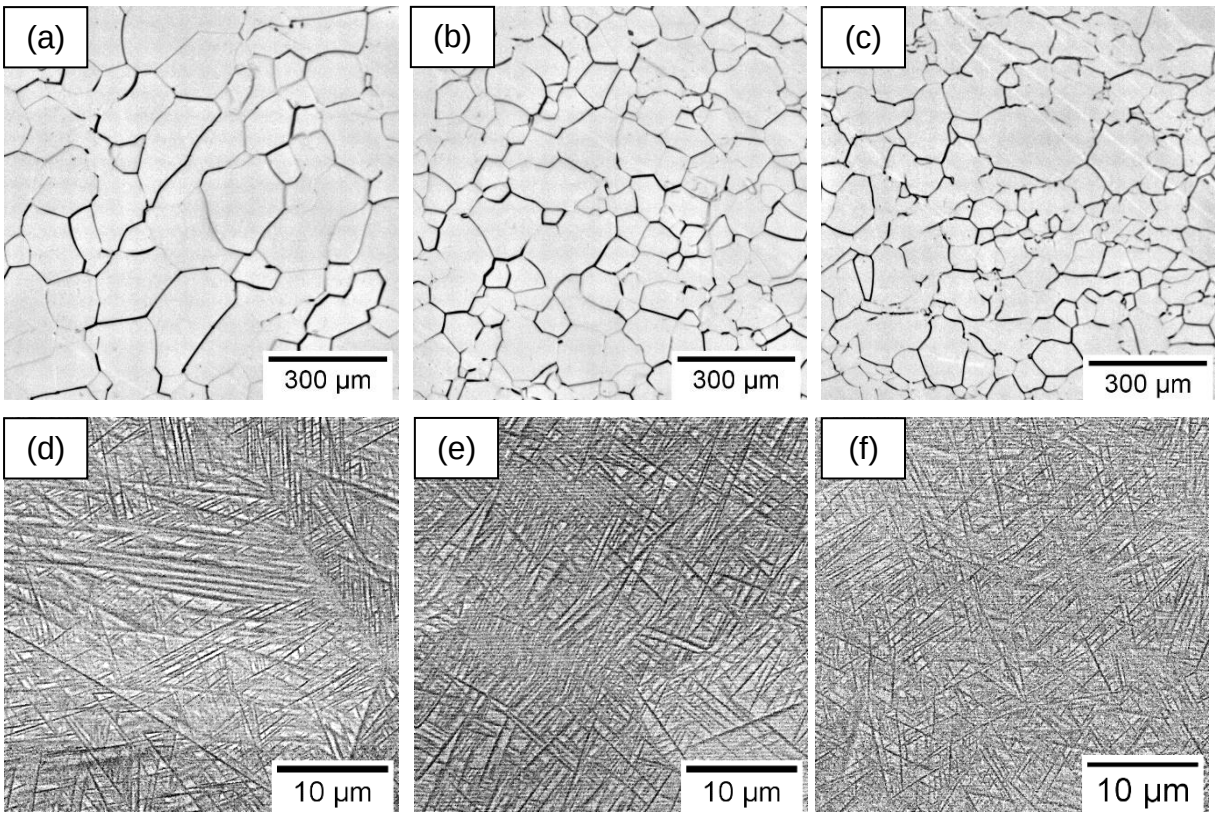

Figure 8.11 – Optical micrographs of the WQ-samples (a-c) and SEM of the aged samples (d-f). Images are related to Ti-23Nb-2.0Fe-10Zr, Ti-27Nb-1.5Fe-10Zr and Ti-31Nb-1.0Fe-10Zr from left to right, respectively.

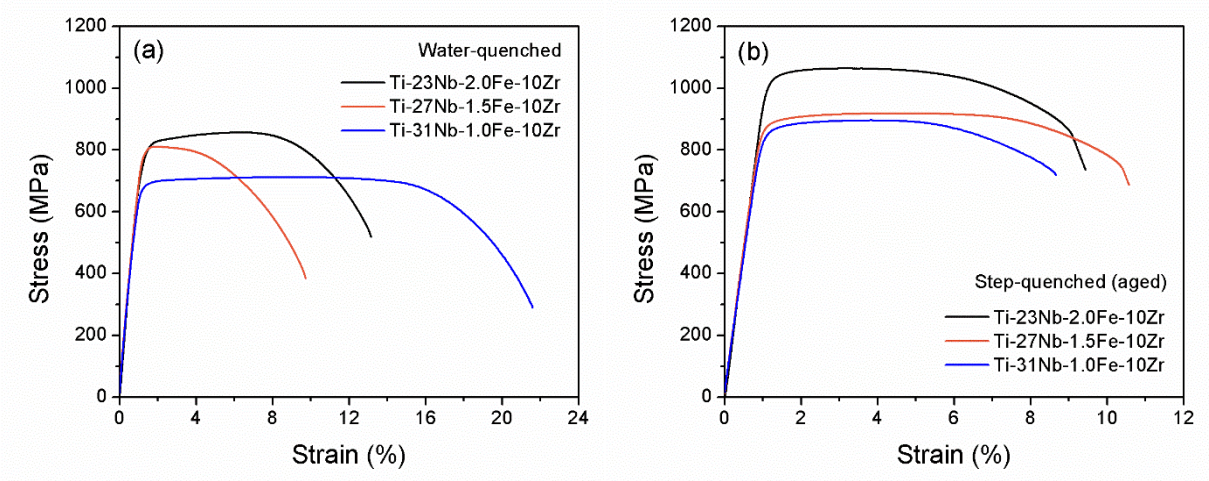

Figure 8.12 – Stress-strain curves for the experimental alloys at the ST-WQ condition (a) and at the aged condition (b).

Based on the fractured surfaces presented in Figure 8.13, a ductile mechanism of rupture is evident among the WQ-samples. The side-view images (Fig 8.13a-c) display a wide necking region for all specimens, with a well-known cup-and-cone shape [170]. Fractured surfaces are covered by dimples and a few opened-up pores (dark), which are an indication of a predominant ductile behavior. Dimpled rupture involves three stages: void nucleation, growth, and coalescence. According to Van Stone et al. (1978), in Ti-alloys, in the absence of a second-phase, void nucleation should occur on blocked slip-bands or deformation twins. Given Ti anisotropy, the voids propagate through twin boundaries or grain boundaries, taking advantage of the multiple deformation modes available on both sides of these boundaries [171], what is in accordance with our experimental observations and with the XRD data presented in the last section. Furthermore, a higher Nb content seems to be associated with fewer dimples, which are elongated and greater in size in Ti-31Nb-1.0Fe-10Zr specimens. A difference in the density and size of dimples based on composition was also reported in Lopes et al. (2016) while exploring the Ti-Nb-Fe system, corroborating with these observations.

As for the aged specimens., the side-view (Figure 8.14a-c) displays a mild necking and a few sharp ledges, which are more representative of both ductile and brittle (mixed) fracture modes. Accordingly, the fracture surfaces encompass a high density of small dimples, a few quasi-cleavage facets, and opened-up pores. Still, the micro-fracture surfaces are dominated by dimples, as can be seen in Figures 8.14g-i. That makes sense since the average

elongation at break for the aged specimens reaches 8%. As a frame of reference, heat-treated Ti-5553 also presents a quasi-cleavage, transgranular fracture mode under tensile, however, with a predominance of cleavage facets over dimples. In the case of Ti-5553, elongation at break is limited to 2%. In this context, it could be stated that the alloys explored in this Chapter still present a relatively high-ductility, even after aging.

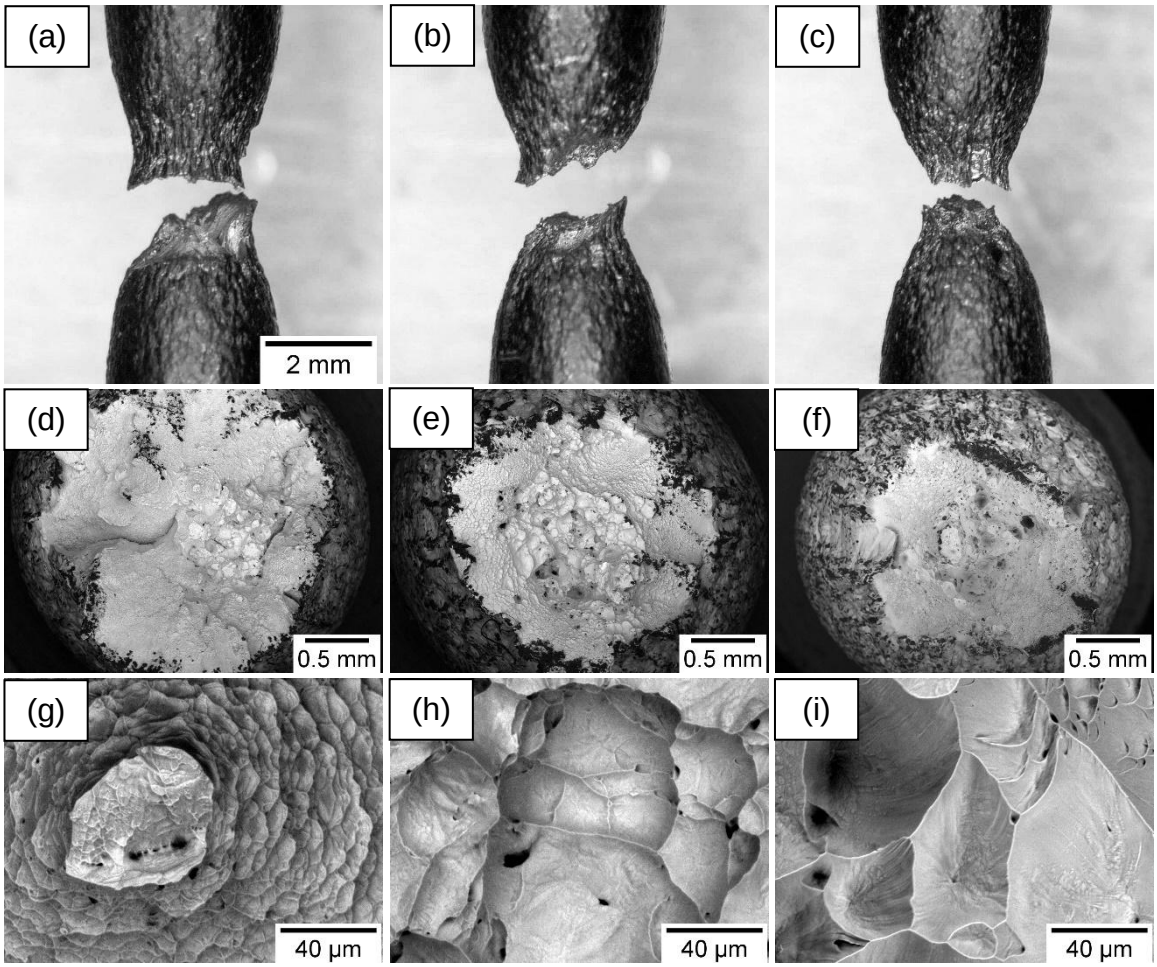

Figure 8.13 – Fractography of the samples subjected to ST-WQ. Side view of the specimens after testing (a-c), overview (d-f) and detailed (g-i) SEM images of the fractured surfaces. From left to right, respectively: Ti-23Nb-2.0Fe-10Zr, Ti-27Nb-1.5Fe-10Zr and Ti-31Nb-1.0Fe-10Zr.

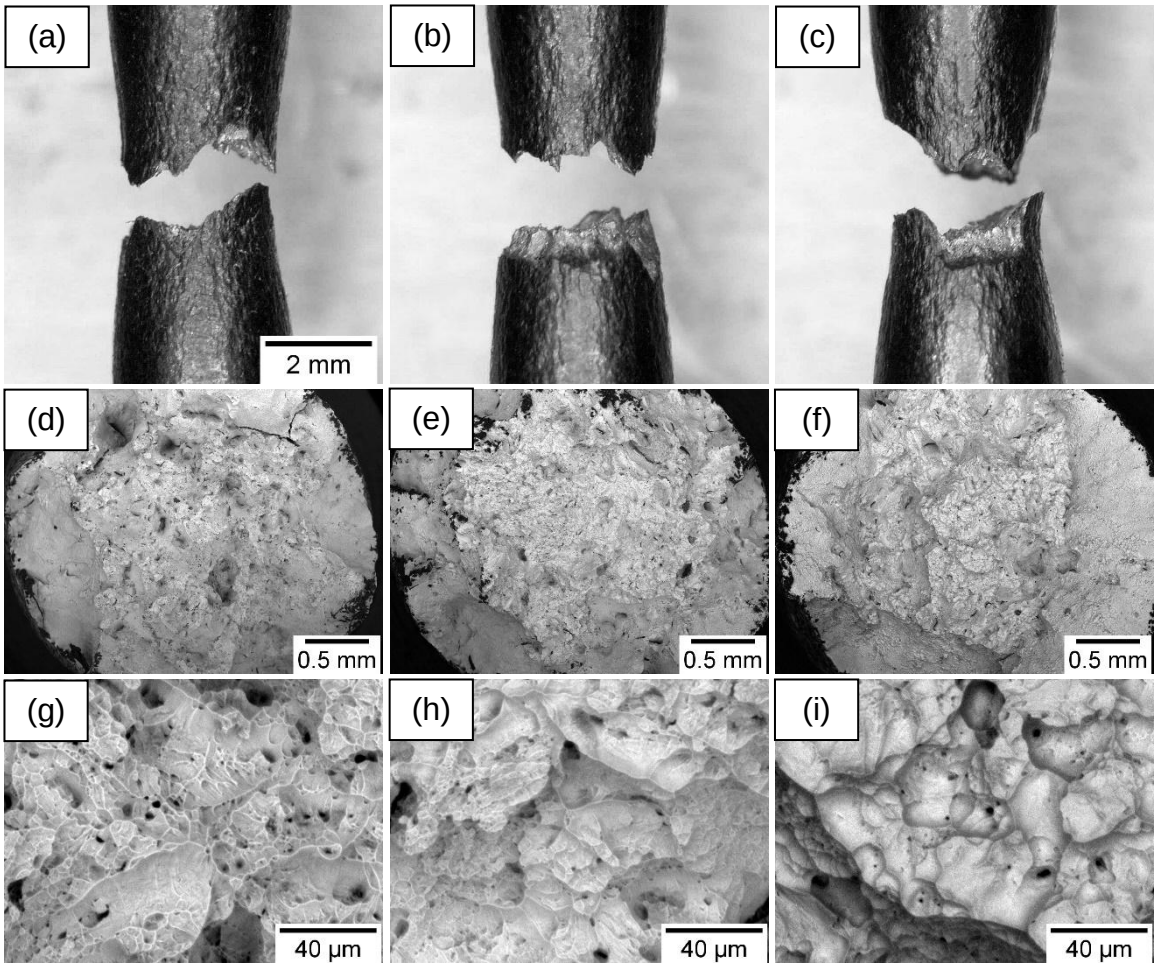

Figure 8.14 – Fractography of the samples subjected to aging. Side view of the specimens after testing (a-c), overview (d-f) and detailed (g-i) SEM images of the fractured surfaces. From left to right, respectively: Ti-23Nb-2.0Fe-10Zr, Ti-27Nb-1.5Fe-10Zr and Ti-31Nb-1.0Fe-10Zr.

Table 8.4 – Compilation of the mechanical properties of high-Nb alloys

Alloy	Condition	Yield (MPa)	E modulus (GPa)	E modulus (GPa)*	Elongation at break (%)
Ti-23Nb-2.0Fe-10Zr	**WQ**	782 ± 62	79 ± 1	72 ± 2	10 ± 1
	Aged	980 ± 62	104 ± 10	87 ± 2	8 ± 1
Ti-27Nb-1.5Fe-10Zr	**WQ**	735 ± 94	78 ± 3	77 ± 2	9 ± 1
	Aged	903 ± 33	101 ± 5	85 ± 3	8 ± 3
Ti-31Nb-1.0Fe-10Zr	**WQ**	672 ± 99	77 ± 2	75 ± 2	15 ± 6
	Aged	796 ± 94	89 ± 1	86 ± 4	10 ± 5

Two elastic modulus measurements, via tensile tests and the *pulse-echo technique

8.4 Compilation of the mechanical properties

Materials property charts (Ashby maps) are useful tools for selecting materials for structural parts. They represent, in a concise way, how two properties of interest correlate with each other. Also, by analyzing the position of a given material on the chart, one can promptly have a dimension on how the material will perform compared to other candidates concerning these properties [172].

With Fig. 8.15, we provide a detailed comparison of the alloys proposed in this thesis and 24 other compositions taken from the literature. Individual points in the graph are displayed as numbers, each one associated with an alloy listed in Table 8.6. Figure 8.15 was adapted from Dal Bó et al. (2018) [166]. In the version presented here, additional data from the ternary system and section 8.3 were added to the chart. As properties of interest for the map, we selected the elastic admissible strain, a well-developed performance index to structural biomaterials, and the alloy cost, which was estimated based on the cost-per-weight of the base metals traded on the London Metal Exchange (2016 first quarter), in United State Dollars (US$), and its relative proportion in each alloy. For a matter of reference, the cost-per-weight of the metals were compiled and are presented in Table 8.5.

Table 8.5 – Cost per kg of metals traded on the London Metal Exchange, in US$

Pure metal (99.9%)	Cost (US$/kg)
Ti	11.7
Ta	383.6
Nb	190.5
Zr	35
Mo	44.5
Fe	0.75
Cr	15.4
Sn	13.2

*Data extracted from [173] and www.lme.com.

Let`s finally take a bird's eye view of the problem (Figure 8.15). From left to right, upper on the chart, we can spot #13 (TNZT-O) and #10 (Ti-42Nb-O). As expected, TNZT and related alloys (overlaid in red) perform well in terms of elastic admissible strain; however, their cost is elevated due to the high percentage of Nb, Ta, and Zr in their composition - that is why they are displayed far left on the chart. Ternary alloys as the ones reported by Biesiekierski et al. (Ti-34Nb-25Zr) and Bahl et al. (Ti- 32Nb-2Sn), #7 and #8, respectively, have a relatively high elastic admissible strain, but their high-Nb content makes them a bit expensive (centered on the chart). The same happens for the high-Nb alloys presented in section 8.3, which are also centered on the chart (#37-42).

On the lower part of the chart, in blue, we expose the limitations of solute-lean ternary alloys such as (#1) Ti-6Al-4V, (#2) Ti-13Nb-13Zr and other alloys from the TNF system (#3–#5). All the same, ternary compositions from Chapter 4 (#25-30) are also displayed in this field. They barely achieve an elastic admissible strain of 1.0. As described in Chapter 4, among samples submitted to solution-treatment followed by water-quenching, the elastic modulus is always higher than 80 GPa due to the presence of ω ath phase [113,122,158]. Similarly, Ti-6Al-4V has a good yield strength, but its elastic modulus is higher than 100GPa, which is a huge penalty to its elastic admissible strain [3]. In conclusion, despite the low-cost associated with ternary alloys, they are deficient in terms of either yield strength or elastic modulus.

Through a combined analysis, the best candidates with a trade-off between elastic admissible strain and cost are displayed in the first quadrant of Fig. 8.15. They are: #24 (Ti-5Fe-3Nb-3Zr), #19 (Ti-12Mo-6Zr-2Fe) and numbers #32, #34 and #35. These numbers refer to Ti-11Nb-3.5Fe-7Zr at the aged condition, Ti-19Nb-2.5Fe-6Sn at the aged condition and Ti-19Nb-2.5Fe-10Zr at the ST-WQ condition, respectively (see Section 8.2). We must highlight the position of #35 (Ti-19Nb-2.5Fe-10Zr) which presented the remarkable elastic admissible strain of 1.49. Also upper on the chart, but with a slightly higher cost, are the remaining alloys from the TNZF system: #23 (Ti-32Nb-6Zr-1.5Fe, Nocivin et al. [174]), #20 and #21 (Ti-28Nb13Zr-0.5Fe, Cui et al. [72]). It may be emphasized that for the cost estimations we considered the price of commercially pure Nb (99.9%). Nevertheless, for the Ti-Nb-Fe-Zr system, the expense could be partially reduced by using Nb-Fe master alloys (66%Nb, 33%Fe) instead, since these alloys have both Nb and Fe in their composition. Master alloys are commodities of the steel industry, and their costs are far inferior to the vacuum-grade Nb

counterpart. As an exception in the first quadrant, Ti-12Mo-6Zr-2Fe alloy (ASTM F1813, [66]) shows that Ti-Mo based alloys can also perform well within the selected criteria. However, Ti-Nb based alloys are superior in respect of wear behavior. According to the literature, Nb allows a quick re-passivation at the surface level, preventing any premature failure due to combined corrosion-wear mechanisms [175].

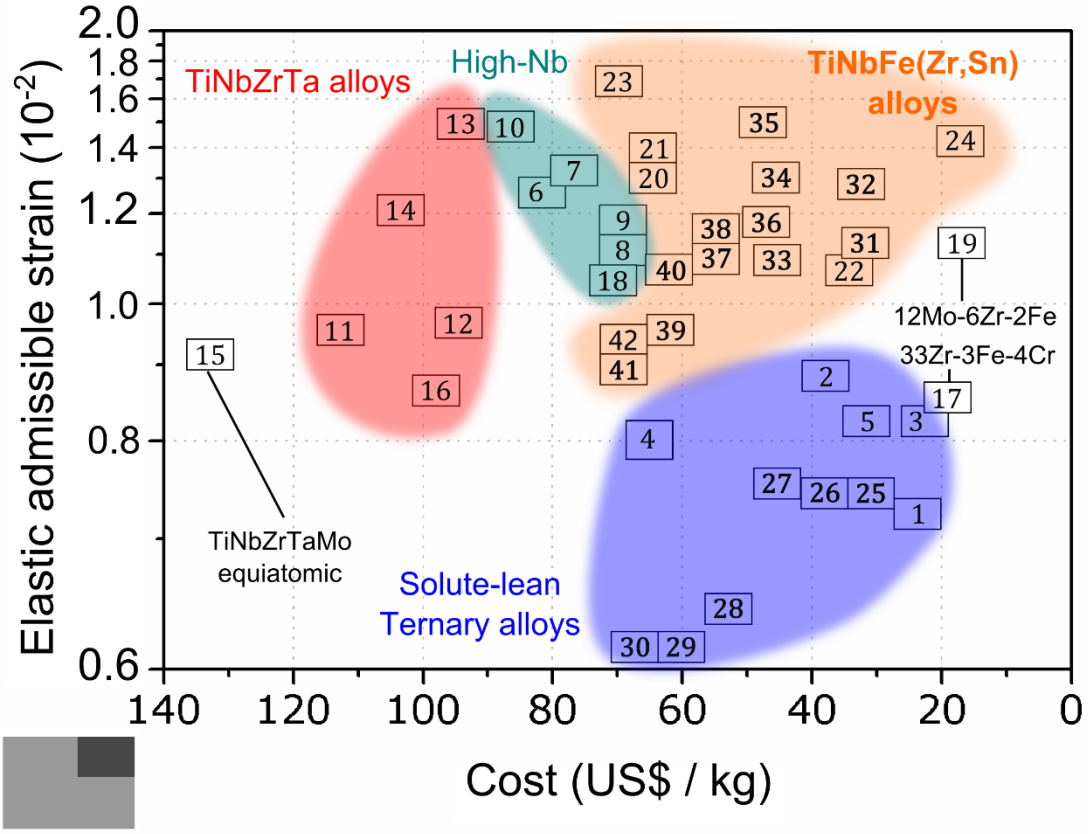

Figure 8.15 – Ashby map is displaying some biomedical alloys from the literature and most of the ones analyzed in this thesis. The 42 individual points displayed in the graph can be found, with the respective references, in Table 8.6.

It is worth reminding that in Fig. 8.15, alloys subjected to ST-WQ and too intricate heat-treatments are compared all at once; thus, their microstructure is varied. For more information on the thermal history of each alloy, please check the respective references. In general, with the precipitation of α-phase during aging-heat treatments, both yield strength and elastic modulus are increased [49,70], and a different EAS can be found for either condition.

Table 8.6 – Mechanical properties of 42 biomedical alloys - Raw data for Figure 8.15

Id. #	Alloy	Condition	Phases*	E (GPa)	YS (MPa)	EAS (%)	Cost (US$/kg)	Ref
1	Ti-6Al-4V	ST	β+α	110	795	0.72	25.5	[176]
2	Ti-13Nb-13Zr	500 ºC, 6h	β+α	82	725	0.88	38.0	[177]
3	Ti-6Al-7Nb	ST	β+α	110	900	0.82	23.7	[178]
4	Ti-30Nb-3Fe	ST - WQ	β+ω (ath)	81	650	0.80	65.0	[69]
5	Ti-12Nb-5Fe	ST	β+α"	90	740	0.82	32.0	[76]
6	Ti-38Nb0.46O	ST	Full β	62	780	1.26	79.6	[179]
7	Ti-34Nb-25Zr	ST-WQ	Full β	62	810	1.31	78.3	[149]
8	Ti-32Nb-2Sn	ST-WQ	Full β	60	665	1.11	69.0	[157]
9	Ti-32Nb-2Sn	500 ºC	β+α	82	960	1.17	69.0	[157]
10	Ti-42Nb	400 ºC, 48h	β+α+α"	67	983	1.47	86.8	[180]
11	Ti-29Nb-13Ta-4.6Zr	ST-WQ	Full β	63	600	0.95	113.0	[59]
12	Ti-35Nb-5Ta-7Zr	ST-WQ	Full β	55	530	0.96	94.5	[5]
13	TNTZ-0.4O	ST-WQ	Full β	66	976	1.48	94.5	[5]
14	Ti-30Nb-10Ta-5Zr	ST-AC	Full β	67	804	1.20	103.7	[175]
15	TiZrNbTaMo	ST	BCC1 + BCC2	153	1390	0.91	133.0	[181]
16	TNZT-2Fe-0.5Si	ST	β + Si-Xt.	83	710	0.86	98.0	[182]
17	Ti-33Zr-3Fe-4Cr	As cast	β + Laves C15	130	1111	0.85	19.2	[183]
18	Ti-32Nb-7Zr-3Sn	ST-WQ	Full β	54	562	1.04	70.6	[184]
19	Ti-12Mo-6Zr-2Fe	ST	Full β	80	897	1.12	16.8	[66]
20	Ti-28Nb-13Zr-0.5Fe	ST-WQ	β+α"	58	780	1.34	64.7	[72]
21	Ti-28Nb-13Zr-0.5Fe	450 ºC, 4h	β+ω (iso)	72	950	1.32	64.7	[72]
22	Ti-19Zr-10Nb-1Fe	ST	β+ω (ath)	59	624	1.06	33.9	[185]
23	Ti-32Nb-6Zr-1.5Fe	ST	Full β	62	1038	1.67	70.1	[174]
24	Ti-5Fe-3Nb-3Zr	ST	(Not described)	83	1169	1.41	17.2	[5]
25	Ti-11Nb-3.5Fe	ST-WQ	β+ω (ath)	97	715	0.74	31.0	This work
26	Ti-15Nb-3.0Fe	ST-WQ	β+ω (ath)	94	695	0.74	38.0	This work
27	Ti-19Nb-2.5Fe	ST-WQ	β+ω (ath)	90	672	0.75	45.0	This work
28	Ti-23Nb-2.0Fe	ST-WQ	β+ω (ath)	95	604	0.64	53.0	This work
29	Ti-27Nb-1.5Fe	ST-WQ	β+ω (ath)	94	496	0.53	60.0	This work
30	Ti-31Nb-1.0Fe	ST-WQ	β+ω (ath)	81	477	0.59	67.0	This work
31	Ti-11Nb-3.5Fe-7Zr	ST-WQ	β+ω (ath)	90	1011	1.12	32.6	This work
32	Ti-11Nb-3.5Fe-7Zr	450 ºC, 1/2h	β+α	93	1184	1.27	32.6	This work
33	Ti-19Nb-2.5Fe-6Sn	ST-WQ	β+ω (ath)	71	765	1.08	45.5	This work
34	Ti-19Nb-2.5Fe-6Sn	450 ºC, 12 h	β+α	98	1261	1.29	45.5	This work
35	Ti-19Nb-2.5Fe-10Zr	ST-WQ	Full β	69	1027	1.49	47.7	This work
36	Ti-19Nb-2.5Fe-10Zr	450 ºC, 12 h	β+α	97	1132	1.17	47.7	This work
37	Ti-23Nb-2.0Fe-10Zr	ST-WQ	Full β	72	782	1.09	54.9	This work
38	Ti-23Nb-2.0Fe-10Zr	450 ºC, 12 h	β+α	86	980	1.14	54.9	This work
39	Ti-27Nb-1.5Fe-10Zr	ST-WQ	Full β	77	735	0.95	62.1	This work
40	Ti-27Nb-1.5Fe-10Zr	450 ºC, 12 h	β+α	85	903	1.06	62.1	This work
41	Ti-31Nb-1.0Fe-10Zr	ST-WQ	Full β	75	672	0.89	69.3	This work
42	Ti-31Nb-1.0Fe-10Zr	450 ºC, 12 h	β+α	86	796	0.93	69.3	This work

***β = beta (bcc); α = alpha (hcp), ω = omega (hcp); α" = martensite (orthor.);**

9. CONCLUSIONS AND FUTURE WORKS

In this work, 16 compositions from the ternary (Ti-Nb-Fe) and quaternary (Ti-Nb-Fe-Zr) systems were explored. An additional composition from the Ti-Nb-Fe-Sn was also examined. Semiempirical electronic parameters (Bo, Md, e/a) alone could not predict the behavior of the novel compositions in respect to either their elastic modulus or their phase stability. Overall, the behavior of Fe-rich alloys diverges from the Nb-rich ones. Fe enables higher mechanical strength but unfortunately leads to relatively higher elastic modulus. A good compromise between strength and modulus is obtained for an Nb / Fe atomic ratio between two and eight ($2 < R < 8$).

On the other hand, despite being considered a strong β-stabilizer element, Fe tends to accelerate the formation of both ω and α phases, depending on the annealing temperature. During aging heat-treatments at 350 ºC, ω-phase particles achieved greater sizes in Fe-rich alloys, and presented an unusual semi-cuboidal morphology, given their misfit in respect to the β-matrix. It was not possible to directly observe activation of the pseudoespinodal mechanism in Ti-11Nb-3.5Fe (wt.%) at 450 ºC. According to the experimental results, this composition might be off from the optimal C_0 condition for pseudospinodal at this temperature. Based on the latest thermodynamic assessments, a direct continuation of this work would be checking if Ti-7Nb-3.5Fe (wt.%) could undergo pseudospinodal at 450º C, instead. That was the suggestion of Prof. Hamish Fraser at the end of my internship at The Ohio State University.

During step-quench heat-treatments at 450 ºC, the precipitation of α-phase seems to start independently at the GBs and inside the grains. However, GB α-phase develops faster and to greater sizes given the enormous solute diffusivity through GBs. This behavior highlights the importance of GB-mediated reactions in engineering materials. Atom-probe tomography of the GB regions from samples subjected to high-cooling rates is recommended to give insights into how the phase transformations happen at the GBs, with respect to composition.

For the intragranular α-particles, composition and size of the α-plates could be successfully modeled by a ledgewise kinetic model, with the growth taking place ledge-by-

ledge. In this case, it would be worth trying to match the experimental data with more refined approaches, such as the ones provided by the DICTRA module on ThermoCalc.

Zr and Sn proved to be valuable additions to ternary Ti-Nb-Fe alloys, helping to suppress ath-ω after solution treatment, and hindering the GB-α phase growth during aging heat-treatments. Overall, Zr and Sn additions always lead to a reduction in the elastic modulus, as expected.

Regarding the grain boundaries transformations, the enthalpy of mixing between solute elements can provide useful insights to predict which element will be segregated from/to GBs and therefore drive the nucleation of α-phase. Based on the parameter defined as elastic admissible strain (EAS), the best alloy designed through this study was Ti-19Nb-2.5Fe-10Zr at the ST-WQ condition. This composition presented a yield strength of 1027 ± 33 MPa with an elastic modulus of 69 ± 1 GPa, resulting in an EAS = 1.49, which is comparable to TNZT-0.4O.

Even after the extensive work presented in this thesis, several questions remain unanswered at present. The current challenge of Ti metallurgy lies on unveiling phase transformations that happen at a time scale of milliseconds. One answer to this limitation might be the use of in-situ MEMS sample holders coupled with aberration-corrected TEM, which will be able to record high-resolution events with a compatible time resolution. Another answer to the problem could be performing in-situ experiments using high-energy synchrotron X-rays, which can achieve similar spatial and temporal resolutions.

On account of the fact that this work was only a preliminary attempt to analyze these fast phase transformations events, it is hardly surprising that our results concerning pseudospinodal were not conclusive. Further studies employing atomistic techniques such as Monte Carlo (MC) and Molecular Dynamics (MD) are therefore suggested. With that, it will be possible to simulate events near the GBs, predict changes in the local lattice structure with the reaction time and thus design better experiments to be further explored with state-of-art characterization techniques.

In Brazil, the access to the new, 4^{th} generation synchrotron light source SIRIUS and it's respective high-energy XRD beamline HERA will present a great opportunity of developing edge research on the metallurgy of Ti alloys in the country.

10. REFERENCES

[1] Gabinete do Senador Humberto Costa, Relatório Final CPI das Próteses - CPIDPRO, Senado Fed. Bras. SF/16110.3 (2016).

[2] G. Federal, DATASUS, Informações de Saúde (TABNET), (2017). http://datasus.saude.gov.br.

[3] M. Long, H.J. Rack, Titanium alloys in total joint replacement--a materials science perspective., Biomaterials. 19 (1998) 1621–39. http://www.ncbi.nlm.nih.gov/pubmed/9839998.

[4] T. Saito, T. Furuta, J.-H. Hwang, S. Kuramoto, K. Nishino, N. Suzuki, R. Chen, A. Yamada, K. Ito, Y. Seno, T. Nonaka, H. Ikehata, N. Nagasako, C. Iwamoto, Y. Ikuhara, T. Sakuma, Multifunctional Alloys Obtained via a Dislocation-Free Plastic Deformation Mechanism., Science. 300 (2003) 464–7. doi:10.1126/science.1081957.

[5] M.A. Gepreel, M. Niinomi, Biocompatibility of Ti-alloys for long-term implantation, J. Mech. Behav. Biomed. Mater. 20 (2013) 407–415. doi:10.1016/j.jmbbm.2012.11.014.

[6] P.F. Santos, M. Niinomi, K. Cho, M. Nakai, H. Liu, N. Ohtsu, M. Hirano, M. Ikeda, T. Narushima, Microstructures, mechanical properties and cytotoxicity of low cost beta Ti-Mn alloys for biomedical applications, Acta Biomater. 26 (2015) 366–376. doi:10.1016/j.actbio.2015.08.015.

[7] J.C.W. C. Lütjering, Titanium, Springer-Verlag, Berlin, 2003.

[8] D. Banerjee, J.C. Williams, Perspectives on Titanium Science and Technology, Acta Mater. 61 (2013) 844–879. doi:10.1016/j.actamat.2012.10.043.

[9] M. Semlitsch, Titanium alloys for hip joint replacements, Clin. Mater. 2 (1987) 1–13. doi:10.1016/0267-6605(87)90015-1.

[10] ASTM International, ASTM F67-13(2017), Standard Specification for Unalloyed Titanium, for Surgical Implant Applications (UNS R50250, UNS R50400, UNS R50550, UNS R50700), West Conshohocken, PA. (2017). doi:10.1520/F0067-13R17.

[11] ASTM International, Standard Specification for Wrought Titanium-6Aluminum-4Vanadium ELI (Extra Low Interstitial) Alloy for Surgical Implant Applications (UNS R56401), West Conshohocken, PA. (2013). doi:10.1520/F0136-13.

[12] ASTM International, Standard Specification for Wrought Titanium-6Aluminum-7Niobium Alloy for Surgical Implant Applications (UNS R56700), (n.d.). doi:10.1520/F1295-16.

[13] C.J. Marvel, J.C. Sabol, T. Pasang, M. Watanabe, W.Z. Misiolek, Improving the Mechanical Properties of the Fusion Zone in Electron-Beam Welded Ti-5Al-5Mo-5V-3Cr Alloys, Metall. Mater. Trans. A. 48 (2017) 1921–1930. doi:10.1007/s11661-017-3968-2.

[14] T. Uesugi, S. Miyamae, K. Higashi, Enthalpies of Solution in Ti-X (X = Mo, Nb, V and W) Alloys from First-Principles Calculations, Mater. Trans. 54 (2013) 484–492. doi:10.2320/matertrans.MC201209.

[15] R. Kolli, A. Devaraj, A Review of Metastable Beta Titanium Alloys, Metals (Basel). 8 (2018) 506. doi:10.3390/met8070506.

[16] C.M. Lee, C.P. Ju, J.H. Chern Lin, Structure-property relationship of cast Ti-Nb alloys, J. Oral Rehabil. 29 (2002) 314–322. doi:10.1046/j.1365-2842.2002.00825.x.

[17] H.Y. Kim, Y. Ikehara, J.I. Kim, H. Hosoda, S. Miyazaki, Martensitic transformation, shape memory effect and superelasticity of Ti–Nb binary alloys, Acta Mater. 54 (2006) 2419–2429. doi:10.1016/j.actamat.2006.01.019.

[18] E. Aeby-Gautier, A. Settefrati, F. Bruneseaux, B. Appolaire, B. Denand, M. Dehmas, G. Geandier, P. Boulet, Isothermal α″ formation in β metastable titanium alloys, J. Alloys Compd. 577 (2013) S439–S443. doi:10.1016/j.jallcom.2012.02.046.

[19] C.A.F. Salvador, E.S.N. Lopes, C.A. Ospina, R. Caram, Orthorhombic martensite formation upon aging in a Ti-30Nb-4Sn alloy, Mater. Chem. Phys. 183 (2016) 238–246. doi:10.1016/j.matchemphys.2016.08.023.

[20] Y.L. Hao, S.J. Li, S.Y. Sun, R. Yang, Effect of Zr and Sn on Young's modulus and superelasticity of Ti–Nb-based alloys, Mater. Sci. Eng. A. 441 (2006) 112–118. doi:10.1016/j.msea.2006.09.051.

[21] Y.L. Hao, S.J. Li, S.Y. Sun, C.Y. Zheng, R. Yang, Elastic deformation behaviour of Ti–24Nb–4Zr–7.9Sn for biomedical applications, Acta Biomater. 3 (2007) 277–286. doi:10.1016/j.actbio.2006.11.002.

[22] E.G. Obbard, Y.L. Hao, T. Akahori, R.J. Talling, M. Niinomi, D. Dye, R. Yang, Mechanics of superelasticity in Ti – 30Nb –(8 – 10) Ta – 5Zr alloy, Acta Mater. 58 (2010) 3557–3567. doi:10.1016/j.actamat.2010.02.010.

[23] A. Biesiekierski, J. Wang, M.A.-H. Gepreel, C. Wen, M. Abdel-Hady Gepreel, C. Wen, A new look at biomedical Ti-based shape memory alloys., Acta Biomater. 8 (2012) 1661–9. doi:10.1016/j.actbio.2012.01.018.

[24] M. Bönisch, M. Calin, L. Giebeler, A. Helth, A. Gebert, W. Skrotzki, J. Eckert,

Composition-dependent magnitude of atomic shuffles in Ti–Nb martensites, J. Appl. Crystallogr. 47 (2014) 1374–1379. doi:10.1107/S1600576714012576.

[25] M. Bönisch, A. Panigrahi, M. Calin, T. Waitz, M. Zehetbauer, W. Skrotzki, J. Eckert, Thermal stability and latent heat of Nb–rich martensitic Ti-Nb alloys, J. Alloys Compd. 697 (2017) 300–309. doi:10.1016/j.jallcom.2016.12.108.

[26] D. De Fontaine, Mechanical instabilities in the bcc lattice and the beta to omega phase transformation, Acta Metall. 18 (1970) 275–279.

[27] J.C. Williams, D. Fontaine, N.E. Paton, The ω-phase as an example of an unusual shear transformation, Metall. Trans. 4 (1973) 2701–2708. doi:10.1007/BF02644570.

[28] T.W. Duerig, J.C. Williams, Overview: microstructure and properties of beta titanium alloys, Beta Titan. Alloy. 1980's, TMS. (1984) 19–67.

[29] G. Aurelio, a. Fernández Guillermet, G.J. Cuello, J. Campo, Metastable phases in the Ti-V system: Part I. Neutron diffraction study and assessment of structural properties, Metall. Mater. Trans. A. 33 (2002) 1307–1317. doi:10.1007/s11661-002-0057-x.

[30] Y. Zheng, T. Alam, R.E.A. Williams, S. Nag, R. Banerjee, H.L. Fraser, Structural and Compositional Characteristics of Isothermal Omega Phase in Beta Titanium Alloys, in: Proc. 13th World Conf. Titan., John Wiley & Sons, Inc., Hoboken, NJ, USA, 2016: pp. 559–562. doi:10.1002/9781119296126.ch90.

[31] J. Coakley, A. Radecka, D. Dye, P.A.J. Bagot, H.J. Stone, D.N. Seidman, D. Isheim, Isothermal omega formation and evolution in the Beta-Ti alloy Ti-5Al-5Mo-5V-3Cr, Philos. Mag. Lett. 96 (2016) 416–424. doi:10.1080/09500839.2016.1242877.

[32] D.L. Moffat, D.C. Larbalestier, The Competition between the Alpha and Omega Phases in Aged Ti-Nb Alloys, Metall. Trans. 19A (1988).

[33] B.S. Hickman, Omega phase precipitation in alloys of Ti with transition metals, Trans. Am. Inst. Mining, Metall. Pet. Eng. 245 (1969) 1329–1336.

[34] J. Šmilauerová, P. Harcuba, J. Pospíšil, Z. Matěj, V. Holý, Growth of ω inclusions in Ti alloys: An X-ray diffraction study, Acta Mater. 61 (2013) 6635–6645. doi:10.1016/j.actamat.2013.07.059.

[35] J. Nejezchlebová, M. Janovská, H. Seiner, P. Sedlák, M. Landa, J. Šmilauerová, J. Stráský, P. Harcuba, M. Janeček, The effect of athermal and isothermal ω phase particles on elasticity of β-Ti single crystals, Acta Mater. 110 (2016) 185–191. doi:10.1016/j.actamat.2016.03.033.

[36] D. Choudhuri, Y. Zheng, T. Alam, R. Shi, M. Hendrickson, S. Banerjee, Y. Wang, S.G.

Srinivasan, H. Fraser, R. Banerjee, Coupled experimental and computational investigation of omega phase evolution in a high misfit titanium-vanadium alloy, Acta Mater. 130 (2017) 215–228. doi:10.1016/j.actamat.2017.03.047.

[37] S. Azimzadeh, H.J. Rack, Phase Transformations in Ti-6.8Mo-4.5Fe-1.5Al, Metall. Mater. Trans. A. 29A (1998) 2455–2467.

[38] S. Nag, R. Banerjee, R. Srinivasan, J.Y. Hwang, M. Harper, H.L. Fraser, ω-Assisted nucleation and growth of α precipitates in the Ti–5Al–5Mo–5V–3Cr–0.5Fe β titanium alloy, Acta Mater. 57 (2009) 2136–2147. doi:10.1016/j.actamat.2009.01.007.

[39] E.S.N. Lopes, A. Cremasco, C.R.M. Afonso, R. Caram, Effects of double aging heat treatment on the microstructure, Vickers hardness and elastic modulus of Ti–Nb alloys, Mater. Charact. 62 (2011) 673–680. doi:10.1016/j.matchar.2011.04.015.

[40] S.-H. Kim, S.J. Kang, M. Park, C. Yang, H. Lee, H.N. Han, M. Kim, Vacancy-mediated ω-assisted α-phase formation mechanism in titanium–molybdenum alloy, Acta Mater. 83 (2015) 499–506. doi:10.1016/j.actamat.2014.10.022.

[41] T. Li, D. Kent, G. Sha, J.M. Cairney, M.S. Dargusch, The role of ω in the precipitation of α in near-β Ti alloys, Scr. Mater. 117 (2016) 92–95. doi:10.1016/j.scriptamat.2016.02.026.

[42] T.W. Xu, S.S. Zhang, F.S. Zhang, H.C. Kou, J.S. Li, Effect of ω-assisted precipitation on β→α transformation and tensile properties of Ti–15Mo–2.7Nb–3Al–0.2Si alloy, Mater. Sci. Eng. A. 654 (2016) 249–255. doi:10.1016/j.msea.2015.12.052.

[43] Y. Zheng, R.E.A. Williams, D. Wang, R. Shi, S. Nag, P. Kami, J.M. Sosa, R. Banerjee, Y. Wang, H.L. Fraser, Role of ω phase in the formation of extremely refined intragranular α precipitates in metastable β-titanium alloys, Acta Mater. 103 (2016) 850–858. doi:10.1016/j.actamat.2015.11.020.

[44] F. Sun, J.Y. Zhang, P. Vermaut, D. Choudhuri, T. Alam, S.A. Mantri, P. Svec, T. Gloriant, P.J. Jacques, R. Banerjee, F. Prima, Strengthening strategy for a ductile metastable β -titanium alloy using low-temperature aging, Mater. Res. Lett. 0 (2017) 1–7. doi:10.1080/21663831.2017.1350211.

[45] M.P. Banerjee S, Phase transformations, examples from titanium and zirconium alloys, 1st ed., Oxford: Elsevier, 2007.

[46] Y. Zheng, D. Banerjee, H.L. Fraser, A nano-scale instability in the β phase of dilute Ti–Mo alloys, Scr. Mater. 116 (2016) 131–134. doi:10.1016/j.scriptamat.2016.01.044.

[47] Q. Liang, Y. Zheng, D. Wang, Y. Hao, R. Yang, Y. Wang, H.L. Fraser, Nano-scale

structural non-uniformities in gum like Ti-24Nb-4Zr-8Sn metastable β-Ti alloy, Scr. Mater. 158 (2019) 95–99. doi:10.1016/j.scriptamat.2018.08.043.

[48] Y. Zheng, R.E.A. Williams, H.L. Fraser, Characterization of a previously unidentified ordered orthorhombic metastable phase in Ti-5Al-5Mo-5V-3Cr, Scr. Mater. 113 (2016) 202–205. doi:10.1016/j.scriptamat.2015.10.037.

[49] C.R.M. Afonso, P.L. Ferrandini, A.J. Ramirez, R. Caram, High resolution transmission electron microscopy study of the hardening mechanism through phase separation in a beta-Ti-35Nb-7Zr-5Ta alloy for implant applications., Acta Biomater. 6 (2010) 1625–9. doi:10.1016/j.actbio.2009.11.010.

[50] A.K. Ackerman, V.A. Vorontsov, I. Bantounas, Y. Zheng, T. McAuliffe, W.A. Clark, H.L. Fraser, D. Rugg, D. Dye, Interface characteristics in an {\alpha}+{\beta} titanium alloy, (2018). http://arxiv.org/abs/1805.09882.

[51] Y. Zheng, R.E.A. Williams, G.B. Viswanathan, W.A.T. Clark, H.L. Fraser, Determination of the structure of α-β interfaces in metastable β-Ti alloys, Acta Mater. 150 (2018) 25–39. doi:10.1016/j.actamat.2018.03.003.

[52] T.W. Duerig, J. Albrecht, D. Richter, P. Fischer, Formation and reversion of stress induced martensite in Ti-10V-2Fe-3Al, Acta Metall. 30 (1982) 2161–2172. doi:10.1016/0001-6160(82)90137-7.

[53] A.K. Ackerman, A.J. Knowles, H.M. Gardner, A.A.N. Nemeth, I. Bantounas, A. Radecka, M.P. Moody, P.A.J. Bagot, R.C. Reed, D. Rugg, D. Dye, The Kinetics of Primary Alpha Plate Growth in Titanium Alloys, (2018). http://arxiv.org/abs/1805.09885.

[54] D.A. R. Todd, Gum Metal and Related Alloys, in: Encycl. Mater. Sci. Technol., Elsevier Ltd, 2006: pp. 1–4.

[55] T. Saito, T. Furuta, J. et al. Hwang, Multifunctional Alloys Obtained via a Dislocation-Free Plastic Deformation Mechanism, Science. 300 (2003) 464–7. doi:10.1126/science.1081957.

[56] H.L. Wang, S.A.A. Shah, Y.L. Hao, F. Prima, T. Li, J.M. Cairney, Y.D. Wang, Y. Wang, E.G. Obbard, S.J. Li, R. Yang, Stabilizing the body centered cubic crystal in titanium alloys by a nano-scale concentration modulation, J. Alloys Compd. 700 (2017) 155–158. doi:10.1016/j.jallcom.2016.12.406.

[57] K.K. M. Morinaga, M. Kato, T. Kamimura, M. Fukumoto, I. Harada, Theoretical design of β-type titanium alloys, in: TMS, Warrendale, PA, 1992: pp. 276–283.

[58] M. Abdel-Hady, K. Hinoshita, M. Morinaga, General approach to phase stability and elastic properties of β-type Ti-alloys using electronic parameters, Scr. Mater. 55 (2006) 477–480. doi:10.1016/j.scriptamat.2006.04.022.

[59] M. Niinomi, M. Nakai, J. Hieda, Development of new metallic alloys for biomedical applications, Acta Biomater. 8 (2012) 3888–3903. doi:10.1016/j.actbio.2012.06.037.

[60] M. Abdel-Hady, H. Fuwa, K. Hinoshita, H. Kimura, Y. Shinzato, M. Morinaga, Phase stability change with Zr content in β-type Ti–Nb alloys, Scr. Mater. 57 (2007) 1000–1003. doi:10.1016/j.scriptamat.2007.08.003.

[61] D. Kuroda, M. Niinomi, M. Morinaga, Y. Kato, T. Yashiro, Design and mechanical properties of new beta type titanium alloys for implant materials, Mater. Sci. Eng. A. A243 (1998) 244–249. doi:10.1016/S0921-5093(97)00808-3.

[62] A. Devaraj, V. V. Joshi, A. Srivastava, S. Manandhar, V. Moxson, V.A. Duz, C. Lavender, A low-cost hierarchical nanostructured beta-titanium alloy with high strength, Nat. Commun. 7 (2016) 11176. doi:10.1038/ncomms11176.

[63] G.W. Franti, J.C. Williams, H.I. Aaronson, A survey of eutectoid decomposition in ten Ti-X systems, Metall. Trans. A. 9 (1978) 1641–1649. doi:10.1007/BF02661947.

[64] H.J. Lee, H.I. Aaronson, Eutectoid decomposition mechanisms in hypoeutectoid Ti-X alloys, J. Mater. Sci. 23 (1988) 150–160. doi:10.1007/BF01174047.

[65] S. Nag, R. Banerjee, H.L. Fraser, Microstructural evolution and strengthening mechanisms in Ti-Nb-Zr-Ta, Ti-Mo-Zr-Fe and Ti-15Mo biocompatible alloys, Mater. Sci. Eng. C. 25 (2005) 357–362. doi:10.1016/j.msec.2004.12.013.

[66] ASTM International, Standard Specification for Wrought Titanium-12Molybdenum-6Zirconium-2Iron Alloy for Surgical Implant (UNS R58120), (2013) 12–16. doi:10.1520/F1813-13.2.

[67] C.M. Lee, W.F. Ho, C.P. Ju, J.H. Chern Lin, Structure and properties of Titanium-25 Niobium-x iron alloys., J. Mater. Sci. Mater. Med. 13 (2002) 695–700. http://www.ncbi.nlm.nih.gov/pubmed/15348579.

[68] H.-C. Hsu, S.-K. Hsu, S.-C. Wu, C.-J. Lee, W.-F. Ho, Structure and mechanical properties of as-cast Ti–5Nb–xFe alloys, Mater. Charact. 61 (2010) 851–858. doi:10.1016/j.matchar.2010.05.003.

[69] É.S.N. Lopes, C.A.F. Salvador, D.R. Andrade, A. Cremasco, K.N. Campo, R. Caram, Microstructure, Mechanical Properties, and Electrochemical Behavior of Ti-Nb-Fe Alloys Applied as Biomaterials, Metall. Mater. Trans. A. 47 (2016) 3213–3226.

doi:10.1007/s11661-016-3411-0.

[70] C.P. Wang, J.P. Zheng, Y. Yu, H.F. Hu, X.J. Liu, Experimental investigation and thermodynamic calculation of the phase equilibria in the Fe–Nb–Ti ternary system, Mater. Chem. Phys. 130 (2011) 806–814. doi:10.1016/j.matchemphys.2011.07.071.

[71] V. Raghavan, Fe-Nb-Ti (Iron-Niobium-Titanium), J. Phase Equilibria Diffus. 33 (2012) 404–406. doi:10.1007/s11669-012-0103-3.

[72] W.F. Cui, A.H. Guo, Microstructures and properties of biomedical TiNbZrFe β-titanium alloy under aging conditions, Mater. Sci. Eng. A. 527 (2009) 258–262. doi:10.1016/j.msea.2009.08.057.

[73] P.G. Esteban, E.M. Ruiz-Navas, E. Gordo, Influence of Fe content and particle size the on the processing and mechanical properties of low-cost Ti–xFe alloys, Mater. Sci. Eng. A. 527 (2010) 5664–5669. doi:10.1016/j.msea.2010.05.026.

[74] D. Kent, S. Pas, S. Zhu, G. Wang, M.S. Dargusch, Thermal analysis of precipitation reactions in a Ti–25Nb–3Mo–3Zr–2Sn alloy, Appl. Phys. A. 107 (2012) 835–841. doi:10.1007/s00339-012-6778-9.

[75] D.F. Williams, On the mechanisms of biocompatibility, Biomaterials. 29 (2008) 2941–2953. doi:10.1016/j.biomaterials.2008.04.023.

[76] A. Biesiekierski, J. Lin, Y. Li, D. Ping, Y. Yamabe-Mitarai, C. Wen, Investigations into Ti-(Nb,Ta)-Fe alloys for biomedical applications, Acta Biomater. 32 (2016) 336–347. doi:10.1016/j.actbio.2015.12.010.

[77] S. Ozan, J. Lin, Y. Li, C. Wen, New Ti-Ta-Zr-Nb alloys with ultrahigh strength for potential orthopedic implant applications, J. Mech. Behav. Biomed. Mater. 75 (2017) 119–127. doi:10.1016/j.jmbbm.2017.07.011.

[78] J.W. Cahn, THE KINETICS OF GRAIN BOUNDARY NUCLEATED REACTIONS, Acta Metall. 4 (1956) 449–459.

[79] M. Guttmann, The Role of Residuals and Alloying Elements in Temper Embrittlement, Philos. Trans. R. Soc. A Math. Phys. Eng. Sci. 295 (1980) 169–196. doi:10.1098/rsta.1980.0099.

[80] E.T. Stephenson, The Effect of Tin on the Toughness of Some Common Steels, Metall. Trans. A. 11A (1980).

[81] M. Šob, V. Paidar, P. Lejc, Progress in Materials Science Interfacial segregation and grain boundary embrittlement : An overview and critical assessment of experimental data and calculated results, 87 (2017) 83–139. doi:10.1016/j.pmatsci.2016.11.001.

[82] H. Zhao, F. De Geuser, A. Kwiatkowski da Silva, A. Szczepaniak, B. Gault, D. Ponge, D. Raabe, Segregation assisted grain boundary precipitation in a model Al-Zn-Mg-Cu alloy, Acta Mater. 156 (2018) 318–329. doi:10.1016/j.actamat.2018.07.003.

[83] Y. Zhu, K. Sun, G.S. Frankel, Intermetallic Phases in Aluminum Alloys and Their Roles in Localized Corrosion, J. Electrochem. Soc. 165 (2018) C807–C820. doi:10.1149/2.0931811jes.

[84] O.N. Senkov, J.K. Jensen, A.L. Pilchak, D.B. Miracle, H.L. Fraser, Compositional variation effects on the microstructure and properties of a refractory high-entropy superalloy AlMo 0.5 NbTa 0.5 TiZr, Mater. Des. 139 (2018) 498–511. doi:10.1016/j.matdes.2017.11.033.

[85] L.C. Campanelli, P.S.C.P. da Silva, C. Bolfarini, High cycle fatigue and fracture behavior of Ti-5Al-5Mo-5V-3Cr alloy with BASCA and double aging treatments, Mater. Sci. Eng. A. 658 (2016) 203–209. doi:10.1016/j.msea.2016.02.004.

[86] M. Niinomi, Fatigue performance and cyto-toxicity of low rigidity titanium alloy, Ti–29Nb–13Ta–4.6Zr, Biomaterials. 24 (2003) 2673–2683. doi:10.1016/S0142-9612(03)00069-3.

[87] C. Lin, G. Yin, Y. Zhao, P. Ge, Z. Liu, Analysis of the effect of alloy elements on martensitic transformation in titanium alloy with the use of valence electron structure parameters, Mater. Chem. Phys. 125 (2011) 411–417. doi:10.1016/j.matchemphys.2010.10.039.

[88] W. Xing, A.R. Kalidindi, D. Amram, C.A. Schuh, Solute interaction effects on grain boundary segregation in ternary alloys, Acta Mater. 161 (2018) 285–294. doi:10.1016/j.actamat.2018.09.005.

[89] M.C. Troparevsky, J.R. Morris, M. Daene, Y. Wang, A.R. Lupini, G.M. Stocks, Beyond Atomic Sizes and Hume-Rothery Rules: Understanding and Predicting High-Entropy Alloys, JOM. 67 (2015) 2350–2363. doi:10.1007/s11837-015-1594-2.

[90] Y. Mishin, C. Herzig, J. Bernardini, W. Gust, Grain boundary diffusion: fundamentals to recent developments, Int. Mater. Rev. 42 (1997) 155–178. doi:10.1179/imr.1997.42.4.155.

[91] P. Heitjans, J. Kärger, Diffusion in Condensed Matter, Springer-Verlag, Berlin/Heidelberg, 2005. doi:10.1007/3-540-30970-5.

[92] C. Corvalán, A. Lucía, M. Iribarren, C. Servant, A. Costa e Silva, Study and simulations of quick diffusion in Zr-based alloys, J. Nucl. Mater. 466 (2015) 80–84.

doi:10.1016/j.jnucmat.2015.07.024.

[93] C. Herzig, U. Köhler, S. V Divinski, Tracer diffusion and mechanism of non-Arrhenius diffusion behavior of Zr and Nb in body-centered cubic Zr – Nb alloys Tracer diffusion and mechanism of non-Arrhenius diffusion behavior of Zr and Nb in body-centered cubic Zr – Nb alloys, J. Appl. Phys. 85 (1999) 8119–8130. doi:10.1063/1.370650.

[94] C.A.F. Salvador, V.C. Opini, E.S.N. Lopes, R. Caram, Microstructure evolution of Ti–30Nb–(4Sn) alloys during classical and step-quench aging heat treatments, Mater. Sci. Technol. 33 (2017) 400–407. doi:10.1080/02670836.2016.1216030.

[95] Standard Practice for Measuring Ultrasonic Velocity in Materials, Annu. B. ASTM Stand. (2011). doi:10.1520/E0494-10.

[96] M. DeGraef, Introduction to Conventional Transmission Electron Microscopy, Cambridge University Press, 2003.

[97] C.B. Williams, D. B.; Carter, Transmission electron microscopy - A textbook for materials science, 2nd ed., Springer, 2009.

[98] H.L. Fraser, D.W. McComb, R.E.A. Williams, Transmission Electron Microscopy for Physical Metallurgists, in: Phys. Metall., 5th ed., Elsevier, 2014: pp. 1143–1226. doi:10.1016/B978-0-444-53770-6.00012-5.

[99] J. Jensen, Characterization of a high strength refractory high entropy alloy, AlMo0.5NbTa0.5TiZr, The Ohio State University, 2017.

[100] D.E. Newbury, N.W.M. Ritchie, Performing elemental microanalysis with high accuracy and high precision by scanning electron microscopy/silicon drift detector energy-dispersive X-ray spectrometry (SEM/SDD-EDS), J. Mater. Sci. 50 (2015) 493–518. doi:10.1007/s10853-014-8685-2.

[101] A. Devaraj, S. Nag, R. Srinivasan, R.E.A. Williams, S. Banerjee, R. Banerjee, H.L. Fraser, Experimental evidence of concurrent compositional and structural instabilities leading to ω precipitation in titanium–molybdenum alloys, Acta Mater. 60 (2012) 596–609. doi:10.1016/j.actamat.2011.10.008.

[102] C.A.F. Salvador, V.C. Opini, M.G. Mello, R. Caram, Effects of double-aging heat-treatments on the microstructure and mechanical behavior of an Nb-modified Ti-5553 alloy, Mater. Sci. Eng. A. 743 (2018) 716–725. doi:10.1016/j.msea.2018.11.086.

[103] A. George, V. Sharma, R. Divakar, M. Sabeena, E. Mohandas, Transmission electron microscopy studies and modeling of 3D reciprocal space of ω forming alloy, Micron. 102 (2017) 73–87. doi:10.1016/j.micron.2017.08.004.

[104] P.A. Stadelmann, EMS - a software package for electron diffraction analysis and HREM image simulation in materials science, Ultramicroscopy. 21 (1987) 131–145. doi:10.1016/0304-3991(87)90080-5.

[105] X. Wu, J. del Prado, Q. Li, A. Huang, D. Hu, M.H. Loretto, Analytical electron microscopy of C-free and C-containing Ti–15–3, Acta Mater. 54 (2006) 5433–5448. doi:10.1016/j.actamat.2006.07.002.

[106] J. Yu, J. Liu, J. Zhang, J. Wu, TEM investigation of FIB induced damages in preparation of metal material TEM specimens by FIB, Mater. Lett. 60 (2006) 206–209. doi:10.1016/j.matlet.2005.08.018.

[107] A. Genç, D. Huber, D. Basile, H. l Fraser, P. Fischione, Sample Preparation for Aberration Corrected Microscopy, Microsc. Microanal. 14 (2008) 998–999. doi:10.1017/S1431927608083669.

[108] E. Yücelen, I. Lazić, E.G.T. Bosch, Phase contrast scanning transmission electron microscopy imaging of light and heavy atoms at the limit of contrast and resolution, Sci. Rep. 8 (2018) 2676. doi:10.1038/s41598-018-20377-2.

[109] J.M. Chaves, O. Florêncio, P.S. Silva, P.W.B. Marques, C.R.M. Afonso, Influence of phase transformations on dynamical elastic modulus and anelasticity of beta Ti–Nb–Fe alloys for biomedical applications, J. Mech. Behav. Biomed. Mater. 46 (2015) 184–196. doi:10.1016/j.jmbbm.2015.02.030.

[110] A. V Dobromyslov, V.A. Elkin, Martensitic transformation and metastable beta-phase in binary titanium alloys with d-metals of 4 - 6 periods, Scr. Mater. 44 (2001) 905–910.

[111] S. Ehtemam-Haghighi, Y. Liu, G. Cao, L.-C. Zhang, Phase transition, microstructural evolution and mechanical properties of Ti-Nb-Fe alloys induced by Fe addition, Mater. Des. 97 (2016) 279–286. doi:10.1016/j.matdes.2016.02.094.

[112] F.H. da Costa, C.A.F. Salvador, M.G. de Mello, R. Caram, Alpha phase precipitation in Ti-30Nb-1Fe alloys – phase transformations in continuous heating and aging heat treatments, Mater. Sci. Eng. A. 677 (2016) 222–229. doi:10.1016/j.msea.2016.09.023.

[113] F.H. da Costa, C.A.F. Salvador, M.G. de Mello, R. Caram, Alpha phase precipitation in Ti-30Nb-1Fe alloys – phase transformations in continuous heating and aging heat treatments, Mater. Sci. Eng. A. 677 (2016). doi:10.1016/j.msea.2016.09.023.

[114] S. Ehtemam-Haghighi, Y. Liu, G. Cao, L.-C. Zhang, Influence of Nb on the $\beta \rightarrow \alpha''$ martensitic phase transformation and properties of the newly designed Ti–Fe–Nb alloys, Mater. Sci. Eng. C. 60 (2016) 503–510. doi:10.1016/j.msec.2015.11.072.

[115] I. Weiss, S. L. Semiatin, Thermomechanical processing of alpha titanium alloys—an overview, Mater. Sci. Eng. A. 263 (1999) 243–256.

[116] Y. Sohn, Diffusion in metals, in: Smithells Met. Ref. B., Elsevier, 2004: pp. 13-1-13–120. doi:10.1016/B978-075067509-3/50016-6.

[117] P. Barriobero-Vila, G. Requena, S. Schwarz, F. Warchomicka, T. Buslaps, Influence of phase transformation kinetics on the formation of α in a β-quenched Ti–5Al–5Mo–5V–3Cr–1Zr alloy, Acta Mater. 95 (2015) 90–101. doi:10.1016/j.actamat.2015.05.008.

[118] P. Barriobero-Vila, G. Requena, F. Warchomicka, A. Stark, N. Schell, T. Buslaps, Phase transformation kinetics during continuous heating of a β-quenched Ti–10V–2Fe–3Al alloy, J. Mater. Sci. 50 (2015) 1412–1426. doi:10.1007/s10853-014-8701-6.

[119] M.J. Williams, J.C. Blackburn, Influence of misfit on morphology and stability of omega phase in titanium-transition metal alloys, Trans. Met. Soc. AIME 245 (1969) 2352–2355.

[120] H.P. Ng, a. Devaraj, S. Nag, C.J. Bettles, M. Gibson, H.L. Fraser, B.C. Muddle, R. Banerjee, Phase separation and formation of omega phase in the beta matrix of a Ti–V–Cu alloy, Acta Mater. 59 (2011) 2981–2991. doi:10.1016/j.actamat.2011.01.038.

[121] B. Tang, Y.-W. Cui, H. Chang, H. Kou, J. Li, L. Zhou, A phase-field approach to athermal β→ω transformation, Comput. Mater. Sci. 53 (2012) 187–193. doi:10.1016/j.commatsci.2011.09.011.

[122] C.A.F. Salvador, M.R. Dal Bó, F.H. Costa, M.O. Taipina, E.S.N. Lopes, R. Caram, Solute lean Ti-Nb-Fe alloys: An exploratory study, J. Mech. Behav. Biomed. Mater. 65 (2017) 761–769. doi:10.1016/j.jmbbm.2016.09.024.

[123] S.E. Haghighi, H.B. Lu, G.Y. Jian, G.H. Cao, D. Habibi, L.C. Zhang, Effect of α″ martensite on the microstructure and mechanical properties of beta-type Ti–Fe–Ta alloys, Mater. Des. 76 (2015) 47–54. doi:10.1016/j.matdes.2015.03.028.

[124] M.C. Troparevsky, J.R. Morris, P.R.C. Kent, A.R. Lupini, G.M. Stocks, Criteria for predicting the formation of single-phase high-entropy alloys, Phys. Rev. X. 5 (2015) 1–6. doi:10.1103/PhysRevX.5.011041.

[125] X.H. Min, S. Emura, N. Sekido, T. Nishimura, K. Tsuchiya, K. Tsuzaki, Effects of Fe addition on tensile deformation mode and crevice corrosion resistance in Ti–15Mo alloy, Mater. Sci. Eng. A. 527 (2010) 2693–2701. doi:10.1016/j.msea.2009.12.050.

[126] L.-F. Huang, B. Grabowski, J. Zhang, M.-J. Lai, C.C. Tasan, S. Sandlöbes, D. Raabe, J. Neugebauer, From electronic structure to phase diagrams: A bottom-up approach to

understand the stability of titanium–transition metal alloys, Acta Mater. 113 (2016) 311–319. doi:10.1016/j.actamat.2016.04.059.

[127] T. Li, M. Ahmed, G. Sha, R. Shi, G. Casillas, H.-W. Yen, Y. Wang, E. V. Pereloma, J.M. Cairney, The influence of partitioning on the growth of intragranular α in near-β Ti alloys, J. Alloys Compd. 643 (2015) 212–222. doi:10.1016/j.jallcom.2015.04.143.

[128] T. Li, D. Kent, G. Sha, L.T. Stephenson, A. V Ceguerra, S.P. Ringer, M.S. Dargusch, J.M. Cairney, New insights into the phase transformations to isothermal ω and ω-assisted α in near β-Ti alloys, Acta Mater. 106 (2016) 353–366. doi:10.1016/j.actamat.2015.12.046.

[129] V.C. Opini, C.A.F. Salvador, K.N.. Campo, E.S.N. Lopes, R.R. Chaves, R. Caram, α phase precipitation and mechanical properties of Nb-modified Ti-5553 alloy, Mater. Sci. Eng. A. 670 (2016) 112–121. doi:10.1016/j.msea.2016.06.001.

[130] R. Dong, J. Li, J. Fan, H. Kou, B. Tang, Precipitation of α phase and its morphological evolution during continuous heating in a near β titanium alloy Ti-7333, Mater. Charact. 132 (2017) 199–204. doi:10.1016/j.matchar.2017.07.032.

[131] D. Li, W. Wan, L. Zhu, Y. Jiang, S. Shao, G. Yang, H. Liu, D. Yi, S. Cao, Q. Hu, Experimental and DFT characterization of interphase boundaries in titanium and the implications for ω-assisted α phase precipitation, Acta Mater. 151 (2018) 406–415. doi:10.1016/j.actamat.2018.03.056.

[132] T. Li, D. Kent, G. Sha, M.S. Dargusch, J.M. Cairney, The mechanism of ω-assisted α phase formation in near β-Ti alloys, Scr. Mater. 104 (2015) 75–78. doi:10.1016/j.scriptamat.2015.04.007.

[133] Y. Zheng, D. Choudhuri, T. Alam, R.E.A. Williams, R. Banerjee, H.L. Fraser, The role of cuboidal ω precipitates on α precipitation in a Ti-20V alloy, Scr. Mater. 123 (2016) 81–85. doi:10.1016/j.scriptamat.2016.06.004.

[134] S. Nag, Y. Zheng, R.E. a. Williams, A. Devaraj, A. Boyne, Y. Wang, P.C. Collins, G.B. Viswanathan, J.S. Tiley, B.C. Muddle, R. Banerjee, H.L. Fraser, Non-classical homogeneous precipitation mediated by compositional fluctuations in titanium alloys, Acta Mater. 60 (2012) 6247–6256. doi:10.1016/j.actamat.2012.07.033.

[135] L. Landau, E. Lifshitz, Statistical physics – Part 1, 3rd ed., Butterworth-Heinemann, London, 1980.

[136] B.B. Kozeschnik E, MatCalc—a simulation tool for multicomponent thermodynamics, diffusion and phase transformation kinetics, Math. Model. Weld Phenom. 5. Book 738

(2001) 349–361.

[137] A. Boyne, D. Wang, R.P. Shi, Y. Zheng, A. Behera, S. Nag, J.S. Tiley, H.L. Fraser, R. Banerjee, Y. Wang, Pseudospinodal mechanism for fine α/β microstructures in β-Ti alloys, Acta Mater. 64 (2014) 188–197. doi:10.1016/j.actamat.2013.10.026.

[138] Y. Zheng, R.E.A. Williams, J.M. Sosa, T. Alam, Y. Wang, R. Banerjee, H.L. Fraser, The indirect influence of the ω phase on the degree of refinement of distributions of the α phase in metastable β-Titanium alloys, Acta Mater. 103 (2016) 165–173. doi:10.1016/j.actamat.2015.09.053.

[139] I.B. Timokhina, K.D. Liss, D. Raabe, K. Rakha, H. Beladi, X.Y. Xiong, P.D. Hodgson, Growth of bainitic ferrite and carbon partitioning during the early stages of bainite transformation in a 2 mass% silicon steel studied by in situ neutron diffraction, TEM and APT, J. Appl. Crystallogr. 49 (2016) 399–414. doi:10.1107/S1600576716000418.

[140] C.A.F. Salvador, E.S.N. Lopes, J. Bettini, R. Caram, Formation of alpha phase via pseudospinodal decomposition in Ti-Nb-Fe based alloys, Mater. Lett. 189 (2017) 201–205. doi:10.1016/j.matlet.2016.11.097.

[141] S.M.C. van Bohemen, J. Sietsma, S. van der Zwaag, Experimental observations elucidating the mechanisms of structural beta Ti alloys, Phys. Rev. B. 74 (2006) 134114. doi:10.1103/PhysRevB.74.134114.

[142] S.M.C. van Bohemen, J. Sietsma, S. van der Zwaag, Experimental observations elucidating the mechanisms of structural bcc-hcp transformations in <math display="inline"> <mrow> <mi>β</mi> <mtext>−</mtext> <mi mathvariant="normal">Ti</mi> </mrow> </math> alloys, Phys. Rev. B. 74 (2006) 134114. doi:10.1103/PhysRevB.74.134114.

[143] H.A. Murdoch, C.A. Schuh, Estimation of grain boundary segregation enthalpy and its role in stable nanocrystalline alloy design, J. Mater. Res. 28 (2013) 2154–2163. doi:10.1557/jmr.2013.211.

[144] J.W. Cahn, TRANSITIONS AND PHASE EQUILIBRIA AMONG GRAIN BOUNDARY STRUCTURES, J. Phys. Colloq. 43 (1982) 199–213. doi:https://doi.org/10.1051/jphyscol:1982619.

[145] N.J. Peter, T. Frolov, M.J. Duarte, R. Hadian, C. Ophus, C. Kirchlechner, C.H. Liebscher, G. Dehm, Segregation-Induced Nanofaceting Transition at an Asymmetric Tilt Grain Boundary in Copper Segregation-Induced Nanofaceting Transition at an Asymmetric Tilt Grain Boundary in Copper, Phys. Rev. Lett. 121 (2018) 255502.

doi:10.1103/PhysRevLett.121.255502.

[146] M. Enomoto, M. Fujita, Analysis of the composition of α plates isothermally formed in titanium binary alloys, Metall. Trans. A. 21 (1990) 1547–1556. doi:10.1007/BF02672569.

[147] H.I. Aaronson, W.T. Reynolds, G.J. Shiflet, G. Spanos, Bainite viewed three different ways, Metall. Trans. A. 21 (1990) 1343–1380. doi:10.1007/BF02672557.

[148] A. Borgenstam, A. Engstro, L. Ho Lund, J.A. Ren, Basic and Applied Research: Section I DICTRA, a Tool for Simulation of Diffusional Transformations in Alloys, J. Phase Equilibria. 21 (2000) 269–280. doi:10.1361/105497100770340057.

[149] S. Ozan, J. Lin, Y. Li, R. Ipek, C. Wen, Development of Ti–Nb–Zr alloys with high elastic admissible strain for temporary orthopedic devices, Acta Biomater. 20 (2015) 176–187. doi:10.1016/j.actbio.2015.03.023.

[150] X.H. Min, S. Emura, L. Zhang, K. Tsuzaki, Effect of Fe and Zr additions on ω phase formation in β-type Ti–Mo alloys, Mater. Sci. Eng. A. 497 (2008) 74–78. doi:10.1016/j.msea.2008.06.018.

[151] M. Geetha, A.K. Singh, A.K. Gogia, R. Asokamani, Effect of thermomechanical processing on evolution of various phases in Ti–Nb–Zr alloys, J. Alloys Compd. 384 (2004) 131–144. doi:10.1016/j.jallcom.2004.04.113.

[152] A. Kilmametov, Y. Ivanisenko, B. Straumal, A.A. Mazilkin, A.S. Gornakova, M.J. Kriegel, O.B. Fabrichnaya, D. Rafaja, H. Hahn, Transformations of α' martensite in Ti–Fe alloys under high pressure torsion, Scr. Mater. 136 (2017) 46–49. doi:10.1016/j.scriptamat.2017.04.010.

[153] F. Sun, Y.L. Hao, S. Nowak, T. Gloriant, P. Laheurte, F. Prima, A thermo-mechanical treatment to improve the superelastic performances of biomedical Ti-26Nb and Ti-20Nb-6Zr (at.%) alloys., J. Mech. Behav. Biomed. Mater. 4 (2011) 1864–72. doi:10.1016/j.jmbbm.2011.06.003.

[154] R.P. Kolli, W.J. Joost, S. Ankem, Phase Stability and Stress-Induced Transformations in Beta Titanium Alloys, JOM. 67 (2015) 1273–1280. doi:10.1007/s11837-015-1411-y.

[155] T. Grosdidier, Y. Combres, E. Gautier, M.J. Philippe, Effect of microstructure variations on the formation of deformation-induced martensite and associated tensile properties in a β metastable Ti alloy, Metall. Mater. Trans. A Phys. Metall. Mater. Sci. 31 (2000) 1095–1106. doi:10.1007/s11661-000-0105-3.

[156] F. Sun, S. Nowak, T. Gloriant, P. Laheurte, a. Eberhardt, F. Prima, Influence of a short

thermal treatment on the superelastic properties of a titanium-based alloy, Scr. Mater. 63 (2010) 1053–1056. doi:10.1016/j.scriptamat.2010.07.042.

[157] S. Bahl, A.S. Krishnamurthy, S. Suwas, K. Chatterjee, Controlled nanoscale precipitation to enhance the mechanical and biological performances of a metastable β Ti-Nb-Sn alloy for orthopedic applications, Mater. Des. 126 (2017) 226–237. doi:10.1016/j.matdes.2017.04.014.

[158] S. Kobayashi, R. Ohshima, K. Nakai, T. Sakamoto, Effect of Quenching and Reheating on Isothermal Phase Transformation in Ti-15Nb-10Zr Alloy, Mater. Sci. Forum. 638–642 (2010) 582–587. doi:10.4028/www.scientific.net/MSF.638-642.582.

[159] C.T. Rueden, J. Schindelin, M.C. Hiner, B.E. DeZonia, A.E. Walter, E.T. Arena, K.W. Eliceiri, ImageJ2: ImageJ for the next generation of scientific image data, BMC Bioinformatics. 18 (2017) 529. doi:10.1186/s12859-017-1934-z.

[160] M.-Y. Seok, Y. Zhao, J.-A. Lee, R.M. Mohamed, L.M. Al-Harbi, M.S. Al-Ghamdi, G. Singh, U. Ramamurty, J. Jang, On the contributions of different micromechanisms for enhancement in the strength of TI–6Al–4V alloy upon B addition: A nanomechanical analysis, Mater. Sci. Eng. A. 649 (2016) 123–127. doi:10.1016/j.msea.2015.09.103.

[161] M.G. de Mello, C.A.F. Salvador, A. Cremasco, R. Caram, The effect of Sn addition on phase stability and phase evolution during aging heat treatment in Ti–Mo alloys employed as biomaterials, Mater. Charact. 110 (2015) 5–13. doi:10.1016/j.matchar.2015.10.005.

[162] G. Neumann, V. To, C. Tuijn, On the impurity diffusion in beta-Ti, Phys. B. 296 (2001) 334–341.

[163] R.A. Perez, H. Nakajima, F. Dyment, Diffusion in alpha-Ti and Zr, Mater. Trans. 44 (2003) 2–13.

[164] B. Jiang, Q. Wang, D. Wen, F. Xu, G. Chen, C. Dong, L. Sun, P.K. Liaw, Effects of Nb and Zr on structural stabilities of Ti-Mo-Sn-based alloys with low modulus, Mater. Sci. Eng. A. 687 (2017) 1–7. doi:10.1016/j.msea.2017.01.047.

[165] M.F. Ijaz, H.Y. Kim, H. Hosoda, S. Miyazaki, Superelastic properties of biomedical (Ti-Zr)-Mo-Sn alloys, Mater. Sci. Eng. C. 48 (2015) 11–20. doi:10.1016/j.msec.2014.11.010.

[166] M.R. Dal Bó, C.A.F. Salvador, M.G. Mello, D.D. Lima, G.A. Faria, A.J. Ramirez, R. Caram, The effect of Zr and Sn additions on the microstructure of Ti-Nb-Fe gum metals with high elastic admissible strain, Mater. Des. 160 (2018) 1186–1195.

doi:10.1016/j.matdes.2018.10.040.

[167] X.J. Liu, Z.K. Liu, A first-principles study of the diffusion coefficients of alloying elements in dilute alpha-Ti alloys, PCCP. 18 (2016) 16870–16881. doi:10.1039/C6CP01899H.

[168] J.L. Wang, L.B. Liu, B.Y. Tuo, W.M. Bai, X. Wang, X. Li, X.P. Hu, Computational Study of Mobilities and Diffusion in Ti-Sn Alloy, 36 (2015) 248–253. doi:10.1007/s11669-015-0377-3.

[169] J.J. Gutiérrez-moreno, Y. Guo, K. Georgarakis, A.R. Yavari, G.A. Evangelakis, C.E. Lekka, The role of Sn doping in the β-type Ti – 25 at % Nb alloys : Experiment and ab initio calculations The role of Sn doping in the b -type Ti – 25 at % Nb alloys : Experiment and ab initio calculations, J. Alloys Compd. 615 (2018) S676–S679. doi:10.1016/j.jallcom.2014.05.024.

[170] S. Gorsse, C. Hutchinson, M. Gouné, R. Banerjee, Additive manufacturing of metals: a brief review of the characteristic microstructures and properties of steels, Ti-6Al-4V and high-entropy alloys, Sci. Technol. Adv. Mater. 18 (2017) 584–610. doi:10.1080/14686996.2017.1361305.

[171] R.H. Van Stone, J.R. Low, J.L. Shannon, Investigation of the fracture mechanism of Ti-5AI-2.5 Sn at cryogenic temperatures, Metall. Trans. A. 9 (1978) 539–552.

[172] M.F. Ashby, Materials Selection in Mechanical Design, 5th editio, Butterworth-Heinemann, 2016.

[173] Y. Abd-elrhman, M.A.-H. Gepreel, A. Abdel-Moniem, S. Kobayashi, Compatibility assessment of new V-free low-cost Ti–4.7Mo–4.5Fe alloy for some biomedical applications, Mater. Des. 97 (2016) 445–453. doi:10.1016/j.matdes.2016.02.110.

[174] A. Nocivin, I. Cinca, D. Raducanu, V.D. Cojocaru, I.A. Popovici, Mechanical properties of a Gum-type Ti–Nb–Zr–Fe–O alloy, Int. J. Miner. Metall. Mater. 24 (2017) 909–917. doi:10.1007/s12613-017-1477-3.

[175] M. Geetha, A.K. Singh, R. Asokamani, A.K. Gogia, Ti based biomaterials, the ultimate choice for orthopaedic implants – A review, Prog. Mater. Sci. 54 (2009) 397–425. doi:10.1016/j.pmatsci.2008.06.004.

[176] F. Spectrometry, F. Technique, R. Metals, T. Alloys, A. Bar, Standard Specification for Wrought Titanium-6Aluminum-4Vanadium ELI (Extra Low Interstitial) Alloy for Surgical Implant Applications (UNS, (2013) 6–10. doi:10.1520/F0136-12A.2.

[177] F. Technique, R. Metals, T. Alloys, Standard Specification for Wrought Titanium-

13Niobium-13Zirconium Alloy for Surgical Implant Applications (UNS R58130) 1, 08 (2013) 5–9. doi:10.1520/F1713-08R13.2.

[178] ASTM F562, Standard Specification for Wrought 35Cobalt-35Nickel-20Chromium-10Molybdenum Alloy for Surgical Implant Applications, ASTM Int. (2013) 1–5. doi:10.1520/F0562-13.2.

[179] Q. Li, D. Ma, J. Li, M. Niinomi, M. Nakai, Y. Koizumi, D. Wei, T. Kakeshita, T. Nakano, A. Chiba, K. Zhou, D. Pan, Low Young's Modulus Ti–Nb–O with High Strength and Good Plasticity, Mater. Trans. 59 (2018) 858–860. doi:10.2320/matertrans.M2018021.

[180] T. Figueiredo Azevedo, T. Nunes Lima, J. Garcia de Blas, L. Carlos Pereira, S. Griza, The mechanical behavior of TiNbSn alloys according to alloying contents, cold rolling and aging, J. Mech. Behav. Biomed. Mater. 75 (2017) 33–40. doi:10.1016/j.jmbbm.2017.07.002.

[181] S.P. Wang, J. Xu, TiZrNbTaMo high-entropy alloy designed for orthopedic implants: As-cast microstructure and mechanical properties, Mater. Sci. Eng. C. 73 (2017) 80–89. doi:10.1016/j.msec.2016.12.057.

[182] I. Kopova, J. Stráský, P. Harcuba, M. Landa, M. Janeček, L. Bačákova, Newly developed Ti–Nb–Zr–Ta–Si–Fe biomedical beta titanium alloys with increased strength and enhanced biocompatibility, Mater. Sci. Eng. C. 60 (2016) 230–238. doi:10.1016/j.msec.2015.11.043.

[183] C.D. Rabadia, Y.J. Liu, L. Wang, H. Sun, L.C. Zhang, Laves phase precipitation in Ti-Zr-Fe-Cr alloys with high strength and large plasticity, Mater. Des. 154 (2018) 228–238. doi:10.1016/j.matdes.2018.05.035.

[184] C. Lan, Y. Wu, L. Guo, H. Chen, F. Chen, Microstructure, texture evolution and mechanical properties of cold rolled Ti-32.5Nb-6.8Zr-2.7Sn biomedical beta titanium alloy, J. Mater. Sci. Technol. 34 (2018) 788–792. doi:10.1016/j.jmst.2017.04.017.

[185] C. Xiong, P. Xue, B. Sun, Y. Li, Effect of annealing temperature on the microstructure and superelasticity of Ti-19Zr-10Nb-1Fe alloy, Mater. Sci. Eng. A. 688 (2017) 464–469. doi:10.1016/J.MSEA.2017.02.031.